

**QUASI-STEADY AND TRANSIENT STUDY OF
FLOW-BOILING PHENOMENA IN A MICROCHANNEL**

MRINAL JAGIRDAR

(B.Tech., SVNIT, India)

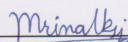
**A THESIS SUBMITTED
FOR THE DEGREE OF DOCTOR OF PHILOSOPHY
DEPARTMENT OF MECHANICAL ENGINEERING
NATIONAL UNIVERSITY OF SINGAPORE**

2015

DECLARATION

I hereby declare that this thesis is my original work and it has been written by me in its entirety. I have duly acknowledged all the sources of information which have been used in the thesis.

This thesis has also not been submitted for any degree in any university previously.

A handwritten signature in blue ink, reading "Mrinal Jagirdar", is written over a horizontal line.

Mrinal Jagirdar
11 November 2015

Acknowledgements

I would like to express gratitude towards my adviser Assoc. Prof. Lee Poh Seng for his trust in me. He was always available for discussions and guidance and ensured that I had the necessary resources for research. I shall always look up to his open-mindedness, helpfulness, positive attitude and high standards of research. I also thank Dr. Karthik B. and Dr. Sivanand S. who were always available for discussions which gave me new ideas that fructified into this thesis. I would also like to express my thanks to Dr. Raghvendra Gupta, formerly at IHPC (A-STAR) for helping me for my oral qualification exam. I also acknowledge support from Dr. Tamanna Alam, Dr. Hassanali Ghaedamini, Dr. Fan Yan, Mr. Matthew Law Lee Liong, Dr. Sunil Dash, Dr. Pawan Kumar Singh, Ms. Mou Nasi, Mr. Ye Yonghuang, Dr. Bernard Saw, Mr. Chirag Shah, Mr. Yeo Linkang, Dr. Jin Liwen, Mr. Xin Xian and Mr. Bugra Kanargi.

I thank the Lab technologist at TPL-2, Ms. Roslina Bte Abdullah. She was always very efficient with paper work. Mr. Abdul Jalil helped me with the design of the PCB and I thank him for that.

Last but not the least, I would like to thank my parents, my brother and grand-father who have always supported me in pursuing my dreams.

Contents

| | |
|---|-------------|
| Summary | v |
| List of Tables | viii |
| List of Figures | ix |
| Nomenclature | xiv |
| 1 Introduction | 1 |
| 1.1 Background | 1 |
| 1.2 Objectives | 4 |
| 1.3 Scope of the Present Work | 5 |
| 1.4 Thesis Structure | 6 |
| 2 Literature Review | 7 |
| 2.1 Flow Boiling Regimes | 7 |
| 2.2 Transition from Unconfined Flow to Confined Flow | 9 |
| 2.3 Fundamentals of Flow Boiling in Microchannels | 11 |
| 2.4 Prediction/Detection of Flow-regimes in Microchannels | 24 |
| 3 Experimental Setup and Procedure | 27 |
| 3.1 Experimental Setup | 27 |
| 3.1.1 Test-section | 27 |
| 3.1.2 Flow Loop | 30 |
| 3.2 Calibration of Temperature Sensors | 32 |
| 3.3 Characterization of Heat Loss | 33 |
| 3.4 Experiment Procedure | 35 |
| 4 Methodologies for Data Reduction | 36 |
| 4.1 Steady State Heat Transfer | 36 |
| 4.2 Transient Heat Transfer | 38 |
| 4.2.1 Literature Review | 39 |
| 4.2.2 Scope | 40 |
| 4.2.3 Test-case | 42 |
| 4.2.4 Mathematical Description | 43 |
| 4.2.5 Test-case Results and Discussion | 50 |

Contents

| | | |
|----------|---|------------|
| 4.2.6 | Validation of IHCP Solution Method for Experiment Based Superimposed Sinusoidal Test-cases | 60 |
| 4.2.7 | Summary | 65 |
| 4.3 | Fast Fourier Transform (FFT) of the Wetted Surface Temperature | 66 |
| 4.4 | Uncertainties | 67 |
| 5 | Results and Discussion | 68 |
| 5.1 | Pressure Drop Characteristics | 70 |
| 5.2 | Heat Transfer Characteristics | 74 |
| 5.2.1 | Boiling Curves | 74 |
| 5.2.2 | Time-averaged Heat Transfer Coefficient Characteristics | 77 |
| 5.2.3 | Transient Heat Transfer Characteristics | 81 |
| 5.3 | Detection of Flow Regimes | 110 |
| 6 | Conclusions and Recommendations for Future Work | 122 |
| 6.1 | Conclusions | 123 |
| 6.2 | Recommendations for Future Work | 127 |
| | Bibliography | 130 |
| | Appendix A: Uncertainty Analysis | 151 |
| | List of Publications | 153 |
| | Attachment | 155 |

Summary

Advances in microelectronics and military hardware have led to a continual increase in heat flux removal requirements. Hence, methods for removal of high heat fluxes have attracted enormous attention in recent years. Flow boiling in microchannels has been identified as a promising method because of advantages like high heat transfer coefficient, low mass flow rate requirement, compact designs, good hot spot mitigation capability and good temperature uniformity across the length.

Flow boiling is a highly transient phenomena which leads to significant temporal changes in heat transfer. Hence, transient nature of flow-regime and heat transfer need to be considered. However, most experimental investigations have only studied time-averaged heat transfer variables. Consequently, there is still a dearth of fundamental understanding of boiling mechanisms and predictive models.

The present work studies both, time-averaged as well as local, transient heat transfer along with flow visualizations during flow boiling of de-ionized water in a single microchannel. Micro-channel heights studied were 0.14, 0.28 and 0.42 *mm*, the tested mass fluxes ranged from 200 – 1000 *kg/m²s* while the tested heat fluxes were up to 105 *W/cm²*.

For transient studies, local temperature data and visual data from the high speed camera were captured synchronously using a TTL signal, at a frequency of 10 *kHz* and 5 *kHz* respectively. A solution methodology for Inverse Heat

Conduction Problem (IHCP) was used to calculate the transient wetted surface heat flux, temperature and heat transfer coefficient which were then correlated with the visual data. Depending on the flow boiling phenomena, there were significant variations in heat transfer with time. During the passage of vapour slugs, transient heat transfer coefficient values peaked and the peak values were much greater than the average values. Thus, thin film evaporation was found to be primarily responsible for enhanced heat transfer. Peak values during thin film evaporation were dependent on how close was the slug incipience from sensor location and whether the flow just downstream of the slug was stagnated. Small secondary peaks in heat transfer coefficient were also observed during the passage of 3-phase contact line. If the liquid slugs were short and fast moving, heat transfer coefficient was relatively higher compared to long, slow moving liquid slugs.

Based on transient temperature data, a methodology has been developed for detection of flow regimes in a microchannel as an alternative to flow visualization. The Fourier Transform of the temperature-time data were corrected for damping due to the solid substrate to get a true amplitude-frequency domain of temperature on the wetted surface. Depending on the prevalent flow regime, there were notable differences in the amplitudes in frequency domain of temperature-time data. This technique is potentially useful for experiments involving multiple inter-layer microchannels within a 3D IC package since high-speed camera cannot be used. This technique may also be used for design of a

Summary

feed-back loop to control the flow-rate which in turn controls the prevalent flow-regime to maximize heat transfer.

List of Tables

| | | |
|-----|---|----|
| 4.1 | MAE(%) in heat transfer coefficient at data-logging frequency of 10 kHz | 59 |
| 4.2 | MAE(%) in heat transfer coefficient at data-logging frequency of 1 kHz | 59 |
| 4.3 | Constituent sine-waves' frequency and amplitude for test-case 1 | 62 |
| 4.4 | Constituent sine-waves' frequency and amplitude for test case 2 | 64 |
| 5.1 | Microchannel dimensions and experimental test conditions | 69 |

List of Figures

| | | |
|-----|---|----|
| 2.1 | Flow boiling regimes : (a) Bubbly flow (b) Slug flow (c) Churn flow (d) Wispy annular flow (e) Annular flow | 8 |
| 2.2 | Schematic showing similarities between heat transfer mechanisms during pool boiling and slug flow during microchannel flow boiling | 19 |
| 3.1 | Exploded view of the assembled test-section | 28 |
| 3.2 | Sectional view along Z-mid-plane (plane of symmetry) | 29 |
| 3.3 | (a) Assembled test-section (b) Silicon test chip (wetted surface) on the PCB (c) 1 x 10 array of thermal test dies behind the silicon surface | 30 |
| 3.4 | Schematic of the flow loop | 31 |
| 3.5 | Calibration curves for diodes on the thermal test-chip | 33 |
| 3.6 | Heat loss vs. average substrate temperature | 34 |
| 4.1 | Schematic of solid domain | 42 |
| 4.2 | Testing of solution algorithm for IHCP | 43 |
| 4.3 | Direct Numerical (Stolz) method vs. Function Specification Method (Constant heat flux functional form) for $A_1 = 1\text{ }^\circ\text{C}$ and $f = 30\text{ Hz}$ (a) Top surface temperature vs. time (b) Heat transfer coefficient vs. time | 50 |
| 4.4 | Induced temperature signal, signal measured by an ideal sensor, signal measured by a real sensor and the estimated signal using IHCP solution method for $A_1 = 1\text{ }^\circ\text{C}$ and $f = 100\text{ Hz}$ | 52 |
| 4.5 | Amplitude ratio vs. frequency | 53 |
| 4.6 | Comparison of IHCP solution methods | 53 |
| 4.7 | IHCP solution method applied to filtered and unfiltered data | 54 |
| 4.8 | Comparison of data-logging frequency (a) $f = 30\text{ Hz}, \sigma = 0.1\text{ }^\circ\text{C}$ (b) $f = 100\text{ Hz}, \sigma = 0.1\text{ }^\circ\text{C}$ | 55 |
| 4.9 | MAE(%) in Heat transfer coefficient vs. r' for $\sigma = 0.1\text{ }^\circ\text{C}, F = 10\text{ kHz}$ (a) $f = 5\text{ Hz}$ (b) $f = 30\text{ Hz}$ (c) $f = 50\text{ Hz}$ (d) $f = 100\text{ Hz}$ | 56 |

| | | |
|------|---|----|
| 4.10 | Heat transfer coefficient vs. time for $F = 10 \text{ kHz}$ (a) $f = 5 \text{ Hz}$, $A_1 = 0.1 \text{ }^\circ\text{C}$ (b) $f = 5 \text{ Hz}$, $A_1 = 2 \text{ }^\circ\text{C}$ (c) $f = 30 \text{ Hz}$, $A_1 = 0.1 \text{ }^\circ\text{C}$ (d) $f = 30 \text{ Hz}$, $A_1 = 2 \text{ }^\circ\text{C}$ (e) $f = 50 \text{ Hz}$, $A_1 = 0.1 \text{ }^\circ\text{C}$ (f) $f = 50 \text{ Hz}$, $A_1 = 2 \text{ }^\circ\text{C}$ (g) $f = 100 \text{ Hz}$, $A_1 = 0.1 \text{ }^\circ\text{C}$ (h) $f = 100 \text{ Hz}$, $A_1 = 2 \text{ }^\circ\text{C}$ | 58 |
| 4.11 | Heat transfer coefficient vs. time for $F = 10 \text{ kHz}$ (a) $f = 300 \text{ Hz}$, $A_1 = 0.2 \text{ }^\circ\text{C}$ (b) $f = 300 \text{ Hz}$, $A_1 = 1 \text{ }^\circ\text{C}$ | 58 |
| 4.12 | FFT for $G = 200 \text{ kg}/(\text{m}^2\text{s})$, $q_b = 17.2\text{W}/\text{cm}^2$ | 62 |
| 4.13 | Assessment of IHCP solution method with superimposed sine waves as the test-case for $H = 0.42 \text{ mm}$ $G = 200 \text{ kg}/(\text{m}^2\text{s})$, $q_b = 17.2\text{W}/\text{cm}^2$ | 63 |
| 4.14 | FFT for $G = 400 \text{ kg}/(\text{m}^2\text{s})$, $q_b = 32 \text{ W}/\text{cm}^2$ | 63 |
| 4.15 | Assessment of the IHCP solution methodology with superimposed sine waves as the test-case for $H = 0.42 \text{ mm}$, $G = 400 \text{ kg}/(\text{m}^2\text{s})$, $q_b = 32 \text{ W}/\text{cm}^2$ | 64 |
| 5.1 | Flow regimes observed during experiments were (a) Single phase flow (b) Bubbly flow (c) Slug flow (d) Churn flow (e) Wispy Annular flow | 70 |
| 5.2 | Effect of microchannel height on pressure drop verses heat flux curves for various mass fluxes | 71 |
| 5.3 | Effect of mass flux on pressure drop verses heat flux curves for various microchannel heights | 73 |
| 5.4 | Effect of microchannel height on the boiling curves for various mass fluxes | 76 |
| 5.5 | Effect of mass flux on the boiling curves for various microchannel heights | 78 |
| 5.6 | Effect of microchannel height on heat transfer coefficient as a function of heat flux for various mass fluxes | 79 |
| 5.7 | Effect of mass flux on heat transfer coefficient as a function of heat flux for various microchannel height | 80 |
| 5.8 | Heat transfer coefficient as a function of heat flux for two separate trials for two cases | 81 |
| 5.9 | Variation of heat transfer coefficient, wall (wetted surface) heat flux and wall (wetted surface) temperature with time for $H = 0.42 \text{ mm}$, $G = 200 \text{ kg}/(\text{m}^2\text{s})$ for (a) $q_b = 17.2 \text{ W}/\text{cm}^2$ (b) $q_b = 25.2 \text{ W}/\text{cm}^2$ | 86 |

| | | |
|------|--|-----|
| 5.10 | Bubbly flow at times when heat transfer coefficient is low in Figure 5.9 at heat fluxes (a) $q_b = 17.2 \text{ W/cm}^2$ (b) $q_b = 25.2 \text{ W/cm}^2$ | 86 |
| 5.11 | Variation of heat transfer coefficient, wall (wetted surface) heat flux and wall (wetted surface) temperature with time for $H = 0.42 \text{ mm}$, $G = 400 \text{ kg/(m}^2\text{s)}$ for (a) $q_b = 24.6 \text{ W/cm}^2$ (b) $q_b = 32 \text{ W/cm}^2$ | 87 |
| 5.12 | Time frames corresponding to Figure 5.11 for (a1) $q_b = 24.6 \text{ W/cm}^2$, nucleation site is close to sensor location (a2) $q_b = 24.6 \text{ W/cm}^2$, long liquid slug (b1) $q_b = 32 \text{ W/cm}^2$, nucleation site is further upstream outside the field of view of the camera (b2) $q_b = 32 \text{ W/cm}^2$, short liquid slug | 87 |
| 5.13 | Variation of heat transfer coefficient with time for $H = 0.42 \text{ mm}$, $G = 200 \text{ kg/(m}^2\text{s)}$, $q_b = 17.2 \text{ W/cm}^2$ from 0.42-0.476 seconds | 88 |
| 5.14 | Video frames corresponding to Figure 5.13 | 88 |
| 5.15 | Schematic of slug flow | 89 |
| 5.16 | Variation of heat transfer coefficient with time for $H = 0.42 \text{ mm}$, $G = 200 \text{ kg/(m}^2\text{s)}$, $q_b = 17.2 \text{ W/cm}^2$ from 0.476-0.56 seconds | 91 |
| 5.17 | Video frames corresponding to Figure 5.16 | 91 |
| 5.18 | Variation of heat transfer coefficient with time for $H = 0.42 \text{ mm}$, $G = 200 \text{ kg/(m}^2\text{s)}$, $q_b = 17.2 \text{ W/cm}^2$ from 0.62-0.78 seconds | 94 |
| 5.19 | Video frames corresponding to Figure 5.18 | 94 |
| 5.20 | Variation of heat transfer coefficient with time for $H = 0.42 \text{ mm}$, $G = 400 \text{ kg/(m}^2\text{s)}$, $q_b = 32 \text{ W/cm}^2$ | 95 |
| 5.21 | Video frames corresponding to Figure 5.20 | 96 |
| 5.22 | Streamlines within a liquid slug trapped between vapour slugs, in a reference frame moving with the bubble | 98 |
| 5.23 | Variation of heat transfer coefficient with time for $G = 400 \text{ kg/(m}^2\text{s)}$, $q_b = 32.5 \text{ W/cm}^2 (\pm 1.5\%)$ for microchannel heights of (a) 0.28 mm (b) 0.42 mm . Video frames (a1) Nucleation site is close to sensor location for condition (a) (a2) Liquid slug is long for condition (a) (b1) Nucleation site is upstream outside the field of view of the camera for condition (b) (b2) Liquid slug length is short for condition (b) | 101 |

| | | |
|------|---|-----|
| 5.24 | Variation of heat transfer coefficient with time for $G = 600$ $kg/(m^2s)$, $q_b = 29.3 W/cm^2(\pm 3.6\%)$ for microchannel heights (a) 0.14 mm (b) 0.28 mm (c) 0.42 mm. Video frames (a1) Short liquid slug for condition (a) (b1) Nucleation site is near to the sensor for condition (b) (b2) Bubbles observed during passage of long liquid slug for condition (b) | 103 |
| 5.25 | Variation of heat transfer coefficient with time for $G = 1000$ $kg/(m^2s)$, $q_b = 42.4 W/cm^2(\pm 2.4\%)$ for various microchannel heights (a) 0.14 mm (b) 0.28 mm (c) 0.42 mm. Video frame (c) Very rarely observed short vapour slug for condition (c) | 105 |
| 5.26 | Variation of heat transfer coefficient with time for $H = 0.14$ mm, $q_b = 28.1 W/cm^2(\pm 3.2\%)$ for mass fluxes (a) 600 $kg/(m^2s)$ (b) 1000 $kg/(m^2s)$ | 106 |
| 5.27 | Variation of heat transfer coefficient with time for $H = 0.28$ mm, $q_b = 30.8 W/cm^2(\pm 3\%)$ for mass fluxes (a) 400 $kg/(m^2s)$ (b) 600 $kg/(m^2s)$ (c) 1000 $kg/(m^2s)$ | 107 |
| 5.28 | Variation of heat transfer coefficient with time for $H = 0.42$ mm, $q_b = 21.1 W/cm^2(\pm 2.8\%)$ for mass fluxes (a) 200 $kg/(m^2s)$ (b) 400 $kg/(m^2s)$ (c) 600 $kg/(m^2s)$ | 108 |
| 5.29 | Variation of heat transfer coefficient with time for $H = 0.42$ mm, $q_b = 59.4 W/cm^2(\pm 2.3\%)$ for mass fluxes (a) 600 $kg/(m^2s)$ (b) 1000 $kg/(m^2s)$ | 109 |
| 5.30 | Typical temperature (measured by sensor) verses time curve for different flow regimes (a) Single phase flow for $H = 0.14$ mm, $G = 1000$ $kg/(m^2s)$ (b) Bubbly flow for $H = 0.42$ mm, $G = 1000$ $kg/(m^2s)$ (c) Slug flow for $H = 0.14$ mm, $G = 1000$ $kg/(m^2s)$ (d) Churn/Wispy-annular flow for $H = 0.14$ mm, $G = 600$ $kg/(m^2s)$ | 111 |
| 5.31 | Comparison of frequency domain obtained directly using transient wall (wetted surface) temperature and corrected frequency domain of temperature sensor data for (a) Single phase flow (b) Bubbly flow (c) Slug flow (d) Slug/Churn flow (e) Churn/Wispy Annular flow | 114 |
| 5.32 | Corrected frequency domain of temperature (measured by sensor) verses time data for $H = 0.14$ mm, $G = 600$ $kg/(m^2s)$ for various heat fluxes | 115 |
| 5.33 | Corrected frequency domain of temperature (measured by sensor) verses time data for $H = 0.14$ mm, $G = 1000$ $kg/(m^2s)$ for various heat fluxes | 115 |

| | | |
|------|--|-----|
| 5.34 | Corrected frequency domain of temperature (measured by sensor) verses time data for $H = 0.28 \text{ mm}$, $G = 400 \text{ kg}/(\text{m}^2\text{s})$ for various heat fluxes | 116 |
| 5.35 | Corrected frequency domain of temperature (measured by sensor) verses time data for $H = 0.28 \text{ mm}$, $G = 600 \text{ kg}/(\text{m}^2\text{s})$ for various heat fluxes | 116 |
| 5.36 | Corrected frequency domain of temperature (measured by sensor) verses time data for $H = 0.28 \text{ mm}$, $G = 1000 \text{ kg}/(\text{m}^2\text{s})$ for various heat fluxes | 117 |
| 5.37 | Corrected frequency domain of temperature (measured by sensor) verses time data for $H = 0.42 \text{ mm}$, $G = 200 \text{ kg}/(\text{m}^2\text{s})$ for various heat fluxes | 117 |
| 5.38 | Corrected frequency domain of temperature (measured by sensor) verses time data for $H = 0.42 \text{ mm}$, $G = 400 \text{ kg}/(\text{m}^2\text{s})$ for various heat fluxes | 118 |
| 5.39 | Corrected frequency domain of temperature (measured by sensor) verses time data for $H = 0.42 \text{ mm}$, $G = 600 \text{ kg}/(\text{m}^2\text{s})$ for various heat fluxes | 118 |
| 5.40 | Corrected frequency domain of temperature (measured by sensor) verses time data for $H = 0.42 \text{ mm}$, $G = 1000 \text{ kg}/(\text{m}^2\text{s})$ for various heat fluxes | 119 |
| 5.41 | Regime detection chart | 120 |

Nomenclature

Roman Symbols

| | |
|------------|---|
| A | amplitude in frequency domain ($^{\circ}C$) |
| A_1 | amplitude of induced temperature signal ($^{\circ}C$) |
| A_s | amplitude of temperature signal at sensor location as measured by an ideal sensor ($^{\circ}C$) |
| A_{ws} | wetted surface area (m^2) |
| c | specific heat of solid ($J/(kgK)$) |
| C_p | specific heat of coolant ($J/(kgK)$) |
| Ca | Capillary number ($= \mu_l U_b / \sigma$) |
| Co | Confinement number |
| D_H | Hydraulic diameter (m) |
| D_{tran} | transition diameter (m) |
| F | data logging frequency (Hz) |
| f | frequency (Hz) |
| f^* | non-dimensional frequency |
| G | mass flux ($kg/(m^2s)$) |

Nomenclature

| | |
|-------------|---|
| g | gravitational acceleration (m/s^2) |
| H | microchannel height (m) |
| h | heat transfer coefficient ($W/(m^2K)$) |
| I | current (A) |
| k | thermal conductivity ($W/(mK)$) |
| L | thickness (m) |
| l | length of the microchannel (m) |
| m | mass flux of coolant ($kg/(m^2s)$) |
| q | heat flux (W/m^2) |
| q_b | base heat flux (W/m^2) |
| q_n | wetted surface heat flux at time step n (W/m^2) |
| q_w | wetted surface heat flux (W/m^2) |
| q_{fluid} | heat flux absorbed by the fluid (W/m^2) |
| Q_t | heat loss (W) |
| r | number of future time-steps |
| r_{opt} | number of future time-steps for minimum MAE(%) in heat transfer coefficient |

Nomenclature

| | |
|--------------|--|
| Ra | average roughness i.e. area between the roughness profile and its center line divided by the evaluation length (μm) |
| Rt | vertical distance from the deepest valley to the highest peak (μm) |
| S | minimization function |
| T | temperature ($^{\circ}C$) |
| t | time (s) |
| T_0 | initial temperature ($^{\circ}C$) |
| T_i | temperature at time step i ($^{\circ}C$) |
| t_s | silicon substrate thickness (m) |
| T_w | wetted surface temperature ($^{\circ}C$) |
| T_{α} | bulk mean temperature of fluid ($^{\circ}C$) |
| T_{ideal} | temperature (noiseless) measured by ideal sensor ($^{\circ}C$) |
| T_{in} | inlet temperature of the coolant ($^{\circ}C$) |
| T_{out} | outlet temperature of the coolant ($^{\circ}C$) |
| T_{sensor} | temperature measured by the sensor ($^{\circ}C$) |
| T_{signal} | induced signal ($^{\circ}C$) |
| U_b | bubble velocity (m/s) |
| V | voltage (V) |

Nomenclature

- w microchannel width (m)
- x spatial co-ordinate along depth (m)
- $Y(t)$ temperature measured by sensor ($^{\circ}C$)
- Y_i measured temperature at time step i ($^{\circ}C$)
- z co-ordinate along flow (m)

Greek Symbols

- α thermal diffusivity of substrate (m^2/s)
- α_1 first order regularization parameter
- ΔT temperature difference ($^{\circ}C$)
- δ liquid thin film thickness (m)
- μ dynamic viscosity ($Pa.s$)
- ω Gaussian variable ($-2.576 < \omega < 2.576$ corresponds to the 99% confidence interval)
- ϕ_i sensitivity coefficient at time step i at the sensor location ($^{\circ}Cm^2W^{-1}$)
- ρ density (kg/m^3)
- σ standard deviation in the noise of the measured temperature ($^{\circ}C$)
- σ_{st} surface tension (N/m)

Subscripts

Nomenclature

l liquid

s silicon

tran transition

v vapour

Abbreviations

CHF Critical Heat Flux

HTC heat transfer coefficient $W/(m^2K)$

IHCP Inverse Heat Conduction Problem

MAE Mean Absolute Error

ONB Onset of Nucleate Boiling

Chapter 1

Introduction

1.1 Background

The continuing increase in integration density of transistors onto microprocessor chips is also leading to increase in power generation and heat dissipation from microprocessors [1]. Already, the current challenge is to remove heat fluxes greater than 100 W/cm^2 while maintaining device temperature below $70 \text{ }^\circ\text{C}$ due to reliability concerns of the chips [2]. Moreover, for military applications like lasers and radars, the challenge is to remove heat fluxes exceeding $10,000 \text{ W/cm}^2$ [3].

It is important to consider reliability, size, noise and power consumption of the cooling solution technology to ensure successful practical application [4]. Apart from the conventional air cooling technology, other cooling technologies worth mentioning are single phase microchannel cooling, 2-phase microchannel cooling, spray cooling, thermo-syphons, heat pipes, refrigeration systems, electro-wetting cooling, immersion cooling, cryogenic cooling, thermoelectric coolers, etc [5]. Among these, microchannel cooling has been considered to

be one of the most promising technologies ever since Tuckerman and Pease proposed this idea in 1981 [1]. Microchannel cooling technology may involve either single phase flow or two phase flow with or without phase change. Since pioneering work on flow boiling in narrow channels by Lazarek and Black [6], flow boiling in microchannels has been a topic of much interest among researchers. This is due to the fact that very high heat transfer coefficient can be achieved and very high heat fluxes can be dissipated. In fact, Mudawar and Bowers [7] could successfully dissipate heat flux of 10 kW/cm^2 using this technology. Moreover, the large latent heat of vaporization of the evaporating fluid improves temperature uniformity by maintaining the working fluid at the saturation temperature at comparatively much smaller flow rates than its single-phase counterparts, thus leading to a smaller pressure drop and a small pumping power requirement, leading to smaller pumps and more compact designs [4]. Flow boiling can also handle localized hot spots effectively as shown by Alam and Lee [8] as well as by Ritchey et al.[9]. Research in this field is hence well warranted.

Research work in the field of microchannel flow boiling is quite diverse. Many researchers carry out parametric studies for detailed understanding of the effect of channel dimensions, wall heat fluxes, mass fluxes etc. on heat transfer, pressure drop, flow instabilities etc [10–13]. Large data-sets have also lead to a number of developed correlations and semi-analytical models for prediction of heat transfer coefficient, pressure drop and Critical Heat Flux [14–16]. Some researchers have also developed flow-regime maps [16–18] and criteria for determination of transition from macro-channel to micro-channel flow boiling

[19, 20]. There is significant literature on active/passive techniques for enhancement of flow boiling heat transfer and Critical Heat Flux as well as for reduction of instabilities and pressure drop. Some achieve this by surface enhancement [1, 21–28], others by the use of novel fins [4, 29–32] and yet others by some active means [33]. With the advent of high performance computing, numerical simulations have also gained significant attention in the field [34–39].

In spite of a plethora of research and although advantages of this cooling technology are aplenty, major challenges limit its commercial application. A fundamental understanding of boiling mechanisms is still missing [10]. Additionally, flow boiling being a highly transient phenomena the heat transfer coefficient is time-dependent since it varies with various stages in bubble growth, as well as with cyclical passage of liquid slug, an evaporating elongated bubble and vapor slug as discussed by Thome et al.[15]. Hence, there is a need to consider the transient nature of flow and consequently the heat transfer as well. Although there is a plethora of research on flow boiling in mini/micro-channels, the focus on experimental studies has largely been on the variation of quasi-steady state heat transfer coefficient with wall heat flux, wall superheat, vapor quality (the ratio of mass flow rate of the vapour phase to the total mass flow rate of the coolant), mass flux, coolants, mini/microchannel sizes etc rather than study of the transient nature of heat transfer. Quite likely due to the severe dearth of transient studies, the existing heat transfer models (based on time averaged heat transfer data) still lack general applicability. There is also a dearth of predictive/diagnostic methods for prediction/detection of flow-regimes during flow

boiling in mini/microchannels. Before micro-channel flow boiling can become a commercial technology, these issues need to be resolved.

1.2 Objectives

1. To study the effect of wall heat flux, mass flux and channel height on time-averaged pressure drop and heat transfer during micro-channel flow boiling.
2. To test, optimize and apply a solution methodology for Inverse Heat Conduction Problem (IHCP) for calculation of transient wall temperature, heat flux and heat transfer coefficient.
3. To correlate video-frames at specific time-intervals with transient temperature, heat flux and heat transfer coefficient (calculated using IHCP solution methodology) and thus analyze and understand the heat transfer mechanisms during flow-boiling in a micro-channel, especially the relative importance of heat transfer during the passage of vapour slug, liquid slug and 3-phase contact line and the effect of hydrodynamics on various heat transfer mechanisms.
4. To develop a diagnostic technique for flow-regime detection during micro-channel flow boiling, based on transient temperature data.

To meet these objectives, experiments on flow boiling have been conducted on a single micro-channel. Time averaged and transient temperature as well as pressure data were captured along with flow visualizations.

1.3 Scope of the Present Work

In this work, apart from collection of time-averaged data, synchronous temperature data logging and flow visualizations are carried out. This is followed by application of solution methodology of IHCP which computes the transient heat transfer coefficient, wall heat flux and temperature which are correlated to video-frames at specific instances. This gives a very unique perspective into heat transfer mechanisms prevalent during different flow boiling phenomena. It thus serves to improve the fundamental understanding of transient heat transfer evolution during flow boiling. The methodology and results also serve to contribute to the development and validation of semi-analytical heat transfer models as well as for validation of numerical simulations. The insights gained from this kind of study can also be utilized to develop novel techniques for enhancement of flow boiling heat transfer.

Based on corrected Fast Fourier Transform of the temperature-time data, a novel technique that can potentially detect flow regimes, has also been developed. Such a technique can be especially of use for experiments involving multiple layers of microchannels in a 3D IC package since flow-visualization with a high-speed camera would not be possible for internal stacks. The technique may also be of utility for design of a feed-back flow loop that may have variable flow-rate to control the prevalent flow-regime to maximize heat transfer and prevent CHF (Critical Heat Flux).

1.4 Thesis Structure

A literature review on mini/micro-channel flow boiling has been presented in Chapter 2. Chapter 3 describes the experimental setup, the test section as well as the procedure for conducting microchannel flow-boiling experiments. Since some of the data-reduction procedures are quite unique and elaborate, Chapter 4 has been fully devoted to it. It has a dedicated literature review as well. In Chapter 5, experimental results are shown and detailed discussions are provided for time-averaged as well as transient variables based on video-frames and existing theories in literature. The effect of wall heat flux, mass flux as well as channel height is discussed. It is also shown how transient temperature signals can be used for detection of flow-regimes. Chapter 6 concludes the thesis and gives recommendations for future work. Appendix A shows the procedure for uncertainty analysis.

Chapter 2

Literature Review

This chapter begins with a general introduction to regimes during flow-boiling. This is followed by a review on quantitative criteria for differentiation between unconfined and confined flows. Next, the effects of various parameters and regimes on flow boiling heat transfer and pressure drop, as available in the literature, are discussed. Based on time-averaged as well as transient studies carried out by a number of researchers, explanation of various heat transfer mechanisms thought to be responsible for heat transfer during flow-boiling in micro-domains is presented. A general review of correlations and semi-empirical models for heat transfer is also given. This is followed by a discussion on prediction/detection methods for flow-regimes. Research gaps are identified, based on which research work presented in this thesis is carried out.

2.1 Flow Boiling Regimes

Flow Boiling in channels is an inherently complex phenomena due to the presence of 2-phases that have changing mass/void fractions. Consequently, various flow-regimes are possible as shown schematically in Figure 2.1. It is

important to understand the prevalent flow regime during experiments since heat transfer and pressure drop characteristics change with the prevalent flow-regime.

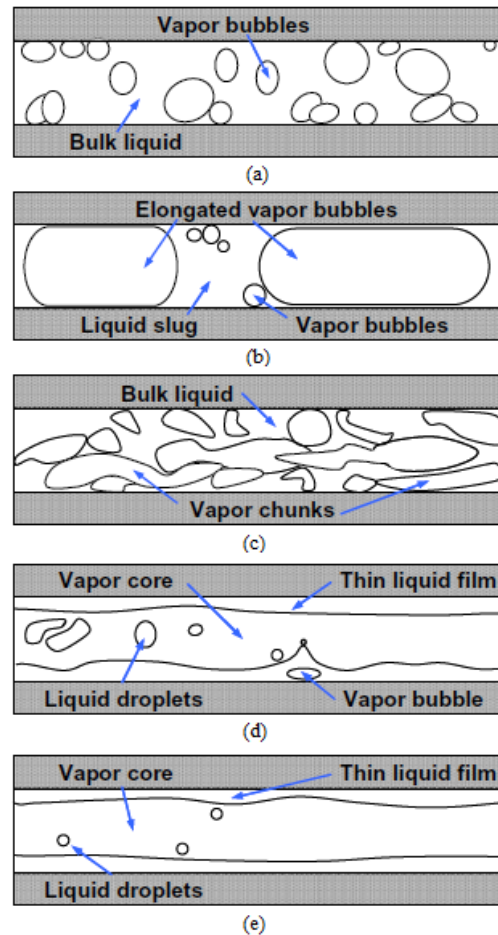


FIGURE 2.1: Flow boiling regimes : (a) Bubbly flow (b) Slug flow (c) Churn flow (d) Wispy annular flow (e) Annular flow [11]

Major flow-regimes typically encountered during flow-boiling are

- (a) Bubbly flow: It is characterized by the presence of round bubbles smaller than the cross section of the channels. The bubbles nucleate and grow at the walls and later detach.

- (b) Slug flow: When bubbles occupy the entire cross-section of the channels and are forced to grow along the flow length, such a flow is called slug flow. Sometimes, small bubbles may exist in the liquid slugs that are between the elongated vapour bubbles/slugs. During passage of vapour slugs, there is a thin film of liquid trapped between the vapour phase and the heated wall.
- (c) Churn flow: The churn flow regime is characterized by oddly shaped chunks of flowing vapour bubbles. There may still be nucleation of large bubbles at a high rate or nucleation may be completely suppressed.
- (d) Wispy annular flow: There exists a thick film of unstable liquid adhering to the wall and an annulus is formed consisting of vapor core. There may be irregularly-shaped droplets entrained in the annular region and some small vapor bubbles may nucleate in the liquid layer.
- (e) Annular flow: The liquid layer is thinner compared to wispy annular flow. The interface may become wavy. Nucleation is typically suppressed [11].

2.2 Transition from Unconfined Flow to Confined Flow

The macro-scale models cannot be applied for predicting flow boiling heat transfer coefficients in microchannels since they are based on the nucleate boiling and convective boiling mechanisms [15]. Also, with decrease in dimensions of the channels, since the surface area to volume ratio becomes much larger, surface forces become more dominant than the body forces. This is contrary to

macro-scale flows and it may completely change the flow physics. For instance, unlike for macro-channels, a nucleate bubble would be confined by the small cross section of the microchannel before departure and there is no stratification observed at micro-scales. Hence micro-scale flow boiling requires exclusive studies rather than extrapolations from research on macro-scale flow boiling.

Several researchers have suggested using various criteria that differentiate confined micro-scale flows from unconfined flows. Mehendale and Jacobi [40] suggested that channels with diameters ranging from 1 – 100 μm must be classified as micro-channels while Kandlikar [41] opined that channel sizes in the range of 10 – 200 μm must be considered as micro-channels.

Some researchers have also incorporated fluid properties into the transition criteria to better predict the pre-dominance of vapour bubble confinement. Kew and Cornwell [19] suggested that if the hydraulic diameters of channels were such that Confinement number given by equation (2.1) was greater than 0.5, then it should be considered as a micro-channel. While Ong and Thome [42] observed confinement effects becoming predominant at a threshold value of ≈ 1 .

$$Co = \frac{[\sigma_{st}/(g(\rho_l - \rho_v))]^{0.5}}{D_H} \quad (2.1)$$

Lee and Mudawar [43] argued that for flow-boiling, it is not just the surface tension and the buoyancy force that are important but drag force on the bubble too is important since it determines the bubble size during departure and thus

influences confinement. Diameter indicating a transition from macrochannel flow to micro-scale flows was derived and is expressed by equation (2.2).

$$D_{tran} = \frac{160 (\sigma \rho_l - 3\mu_l G)}{9 G^2} \quad (2.2)$$

2.3 Fundamentals of Flow Boiling in Microchannels

In 1982, Lazarek and Black [6] conducted a study on flow boiling in 0.31 cm diameter tube with R113 as the coolant. The inlet condition was sub-cooled liquid. They noted that for saturated boiling, heat transfer coefficient was independent of vapour quality. This, according to them implied that nucleate boiling was the heat transfer mechanism. While for negative qualities, HTC (Heat Transfer Coefficient) increased monotonically with quality.

Wambsganss et al. [44] conducted flow boiling heat transfer studies in a tube with a diameter of 2.92 mm with R113 as the refrigerant. The tested heat fluxes and mass fluxes ranged from 8.8 – 90.75 kW/m² and 50 – 300 kg/(m²s) respectively resulting in vapour quality up to 0.9. Their results indicated that HTC is a strong function of heat flux but a weak function of mass flux and mass quality. A flow pattern map was used to determine that the slug flow pattern was dominant and the heat transfer mechanism was concluded to be nucleate boiling.

Yu et al. [45] conducted studies on a small horizontal tube of 2.98 mm diameter using water as the coolant. The mass fluxes ranged from 50 – 200

$kg/(m^2s)$. They observed that heat transfer was heat-flux dependent and independent of mass-flux. Their trend was consistent with boiling in small channels but significantly different from larger-channel boiling wherein mass flux can dominate. Hence they concluded that nucleation mechanism was dominant over the convective mechanism even for high qualities.

Agostini et al. [46, 47] conducted a study on a silicon heat sink composed of 67 microchannels, 223 μm wide, 680 μm high and 20 mm long using refrigerants R236fa and R245fa. For R236fa, heat flux and mass flux range tested were 3.6 – 221 W/cm^2 and 281 – 1501 $kg/(m^2s)$ respectively. The exit vapour quality ranged from 2 – 75 %. They noted that at low heat flux, vapour quality and mass velocity, HTC increased with vapour quality and was independent of heat flux and mass velocity. While, for medium heat fluxes, HTC was nearly independent of the vapour quality, increased with heat flux and was weakly dependent on the mass flux. But, for very high heat fluxes, the HTC increased weakly with mass flux and decreased with increasing heat flux. Heat transfer was thus predominantly dependent on heat flux. For R245fa, their test conditions covered heat fluxes and mass fluxes from 3.6 – 190 W/cm^2 and 281 – 1501 $kg/(m^2s)$. Exit vapour qualities ranged up to 78 %. Again, it was found that at low heat flux, HTC increased with vapour quality and was independent of heat flux and mass velocity. At medium heat flux, HTC increased with heat flux, increased slightly with mass flux and was not dependent on vapour quality. At high heat flux, HTC decreased with increasing heat flux and vapour quality and increased with mass velocity. For R245fa, the influence of mass velocity on HTC was

more than that for R236fa. However, at low heat flux, the heat transfer coefficient shows essentially no dependence on mass velocity for both fluids.

Chen and Garimella [48] conducted flow boiling experiments on a heat sink consisting of 60 parallel microchannels, each of which was $100\ \mu\text{m}$ wide and $389\ \mu\text{m}$ deep. Flow rates tested were in the range of $20 - 80\ \text{ml}/\text{min}$ and the inlet sub-cooling was fixed at $26\ \text{K}$. The working fluid used was FC-77. With increase in heat flux, successive flow patterns observed were bubbly flow, slug flow, elongated bubble flow or annular flow, alternating wispy-annular/churn flow, and wall dryout. Hence, HTC varied substantially with heat flux. Their results also suggest an increase in HTC with flow-rate. Pressure drop was found to increase linearly with heat flux. They highlighted one of their major findings to be that HTC was enhanced in the upstream and downstream region of the microchannels due to changes in flow patterns during instabilities.

Harirchian and Garimella [49] pointed out that when flow is unconfined, heat transfer and boiling curves are independent of the channel size as well as the flow rate. Pressure drop and pumping power have only minor sensitivity to channel size and flow rate. During confined flow, HTC increases as the micro-channel cross sectional area decreases. After the onset of nucleate boiling, the HTC is independent of mass flux and increases with heat flux. But at higher heat fluxes, since contribution from convective heat transfer begins to dominate that of nucleate boiling, the heat transfer coefficient becomes a function of mass flux and increases with increasing mass flux. Thin liquid film evaporation that

is responsible for larger values of HTC as compared to unconfined flow where nucleate boiling is dominant.

Qu and Mudawar [50] conducted flow boiling experiments on a heat sink with 21 parallel microchannels with a width of 231 μm and height of 713 μm using de-ionized water as the coolant. Mass flux tested ranged from 135 to 402 $kg/(m^2s)$. Two, highly sub-cooled inlets, 30 $^{\circ}C$ and 60 $^{\circ}C$ were tested. Abrupt transition to annular flow regime was observed near the point of zero thermodynamic equilibrium quality. They concluded the dominant heat transfer mechanism to be forced convective boiling rather than nucleate boiling. HTC decreased with vapour quality. This was attributed to appreciable droplet entrainment at the onset of annular flow regime development, and the increase in mass flow rate of the annular film by droplet deposition downstream. HTC was a strong function of mass velocity, and only a weak function of heat flux. Another publication ([51]) by the same authors with same microchannel geometry and flow conditions revealed a steep rise in HTC with thermodynamic equilibrium vapour quality (and heat flux) for negative vapour quality (sub-cooled region). However, for saturated boiling region, HTC decreased with vapour quality.

Lee and Mudawar [43], conducted a study on four microchannel heat sinks using HFE7100 as the working fluid. The inlet condition was significantly sub-cooled. Three different inlet temperatures 44, 64 and 74 $^{\circ}C$ lower than saturation temperature were tested. They found that high sub-cooling greatly reduced bubble departure diameter as well as the void fraction, and it prevented flow pattern transitions beyond the bubbly regime.

Balasubramanian et al. [13] conducted a study on multi-microchannel heat sink. Each of the channels was $300 \mu m$ wide and $1200 \mu m$ deep. HTC varied with flow-boiling regime and the corresponding heat transfer mechanism. HTC increases with heat flux and exit vapour quality in the nucleate boiling regime, reaches a peak and then dips down after transitioning to intermittent flow regime where it was found to be remaining almost constant. After transitioning to annular flow regime, HTC increases again, reaches a peak due to thin film evaporation and then drops as dry-out progresses. Thus, HTC had a 'M' shaped variation with heat flux and exit vapour quality. However, in the sub-cooled region of the graph, the HTC increased monotonically with heat flux and consequently with exit vapour quality. Mass flux had a pronounced effect on HTC too beyond the nucleate boiling regime.

Researchers have also been interested in low-aspect ratio microchannels and micro-gaps. Lee and lee [52] conducted experiments for micro-gap size ranging from $0.4 - 2 mm$ using R113 as the test fluid. The tested mass fluxes and heat fluxes respectively ranged from $50 - 200 kg/m^2$ and $0 - 15 kW/m^2$. The vapour quality ranged from $0.15 - 0.75$ and the flow pattern observed was annular. The heat transfer coefficient increased with mass flux and local quality while the effect of heat flux was not significant.

Kandlikar and Balasubramanian [53] studied flow boiling characteristics of water in a set of six parallel mini-channels, each of which was $1054 \mu m$ wide and $197 \mu m$ deep. They used a high-speed camera to capture two-phase flow structure and liquid-vapor interactions. The observed flow patterns were

bubbly flow, thin film nucleation, plug flow, annular flow and churn flow. Even during annular flow or slug flow, bubbles were found to nucleate on the wall. Hence, they concluded the dominance of nucleate boiling which was further substantiated by the observed decreasing trend of HTC with quality.

Bar-Cohen and Rahim [54] performed a detailed analysis of microchannel and micro-gap heat transfer data gathered from the open literature. They first sorted the data by the use of Taitel and Dukler flow regime map and thus identified data for different flow regimes namely bubbly flow, intermittent and annular flow along with stratified flow for small channels. They observed that for channels with diameter less than 0.1 mm, annular flow was the most dominant regime. A characteristic M-shaped HTC variation with quality was found to be prevalent. Transition of flow regimes occurred at the inflection points of this curve. The first maxima indicated a transition from bubble to intermittent flow, then during the intermittent regime there was a decrease in HTC. This was followed by a sharp increase when there was transition to the annular flow. The second maxima was at moderate qualities within annular flow regime just before local dry-out started.

Utaka et al.[55] investigated micro-layer thickness under a confined vapour bubble and heat transfer characteristics for narrow gaps of 0.5, 0.3 and 0.15 mm. They showed that heat transfer was enhanced due to the micro-layer evaporation. They also clarified the effect of various factors on the initial micro-layer thickness. The initial micro-layer thickness decreased as the micro-gap size decreased. Up to a certain threshold velocity of 2 m/s, with increase in velocity,

the film thickness increased, while beyond this velocity, it was nearly constant. Moreover, the initial micro-layer thickness also increased with heat flux since high heat flux caused the bubble forefront velocity to increase. They also observed a dependence of initial micro-layer thickness on the distance from the bubble incipient site.

Kim et al. [56] experimentally investigated the applicability of a micro-gap with FC-72 as a coolant for cooling of high power LED devices. Micro-gap heights ranged from 110 – 500 μm while the mass flux range tested was 55 – 1270 $kg/(m^2s)$. Using the Taitel-Dukler analytical flow regime map, they concluded intermittent and annular flow regimes to be mainly responsible for the two-phase heat transfer. They concluded that it is possible to dissipate up to 600 kW/m^2 from an LED array for a wall superheat of 60 K .

Alam et al. [12] conducted a study on micro-gaps with heights 190, 285 and 381 μm using de-ionized water as the coolant. Mass fluxes tested were 420, 690 and 970 $kg/(m^2s)$ and heat fluxes tested were up to 110 W/cm^2 . At inlet to the microchannels, the temperature was maintained constant at 86 $^{\circ}C$ throughout. Confined slug and annular flow boiling were the dominant flow regimes. HTC increased significantly with heat flux during confined boiling due to thin film evaporation. Boiling curves showed sensitivity to mass flux as well. Smaller micro-gap height yielded better HTC because of greater confinement effects. Also HTC was greater for smaller mass flux. It was also observed that micro-gap maintained a good wall temperature uniformity and smaller temporal fluctuations for small gaps. For larger gap sizes, pressure drop remains almost

constant with heat flux, while for smaller gap sizes, pressure drop increases with heat flux. Pressure drop increased with mass flux for all micro-gap heights.

Based on large-sets of data, a number of different empirical correlations have been developed by researchers. However, they lack general applicability and are mostly good only with parent data-sets. Thome and Consolini [57] reviewed a number of empirical correlations and remarked that none of them were able to predict the diverse trends in the heat transfer coefficients. Similarly, after comparison of a number of empirical correlations against a large database available from various research groups, it was concluded by Bertsch et al. [58] that none of the correlations developed for flow boiling offered an improved prediction over those for pool boiling (boiling occurring on a heated surface that is submerged in a liquid pool that is not agitated) and conventional sized channels. The best predictions, they stated, had a mean absolute error (MAE) of 40% relative to the large experimental database, and predicted less than half of the measured data to within a deviation of $\pm 30\%$.

Harirchian and Garimella [16] pointed out that for nucleate boiling regime, Coopers pool boiling correlation predicted their heat transfer experimental results, for nucleate boiling regime very well. Moreover, they noted that none of the empirical correlations developed specifically for flow boiling in microchannels were found to predict experimental heat transfer for other flow regimes. The experimental results for even the pressure drop were compared with empirical correlations existing in the literature and they yielded very large errors. Thus,

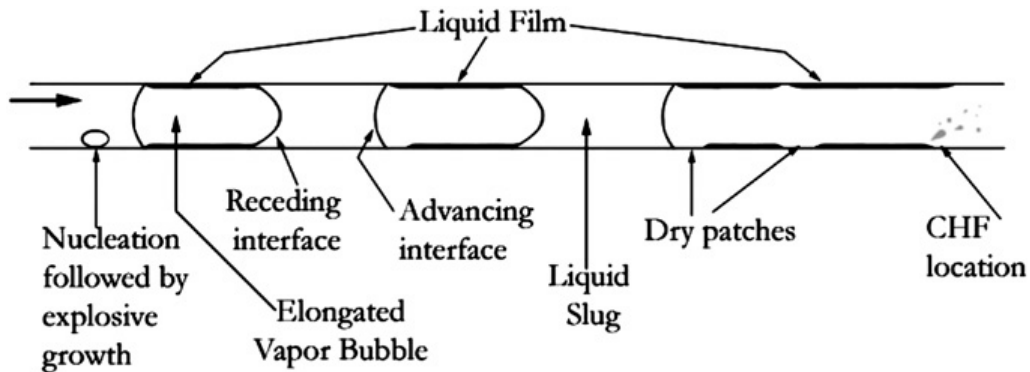


FIGURE 2.2: Schematic showing similarities between heat transfer mechanisms during pool boiling and slug flow during microchannel flow boiling [60]

they concluded that there was a need for development of physics based models for flow boiling heat transfer as well as pressure drop in microchannels.

For development of a physics based model, the mechanism of heat transfer must be known. Some parallels may be drawn between flow boiling in microchannels with pool boiling heat transfer mechanisms. Kim [59] reviewed the heat transfer mechanisms during pool boiling. Based on reviewed experimental and numerical work on pool boiling, the main heat transfer mechanisms identified were transient conduction, micro-layer heat transfer and contact line heat transfer. They clarified, that these mechanisms contribute to various extents depending on various experimental conditions. However, it was concluded that it is mostly the transient conduction and micro-convection that contribute the most to heat transfer augmentation.

Kandlikar [60] noted similarities between the heat transfer mechanisms of pool and flow boiling, not just for nucleation of the bubble, but also for the slug flow. For pool boiling, when the nucleating bubble grows, heat is transferred by

evaporation from the micro-layer beneath the bubble. The micro-layer contribution can be divided between the conduction from the heater and evaporation from the initial superheat of the liquid film. Its contribution reduces significantly as the micro-layer evaporates completely, leaving dry patches at some locations resulting in a very low heat transfer over the patches. As the bubble begins to depart, the liquid interface then advances and covers the surface. This results in a significantly higher heat transfer rate due to transient heat conduction to the liquid which is at a much lower temperature. The cycle begins again with the nucleation of the next bubble. The superheated liquid layer also releases its energy by evaporation at the receding liquid-vapour interface during the growth period of the bubble. The dominant mode of heat transfer for pool boiling, according to him, is transient conduction since it raises the liquid superheat, which is released at the evaporating interface through micro-convection.

Similarly, in the case of flow boiling (see figure 2.2), a nucleating vapour bubble grows by evaporation at the bulk liquid-vapour interface. This provides a relaxation mechanism for liquid superheat in the surrounding liquid. Evaporation from the interface leads to elongation of the bubble in microchannel flow boiling, and the heater surface surrounding the vapour is covered with a micro-layer (or a thin film), similar to the micro-layer under a bubble in pool boiling. The receding and advancing menisci at the front and back of the elongated bubble (as shown in Figure 2.2) are similar to the interfaces during growth and departure phases of a nucleating bubble in pool boiling respectively. The transient conduction mechanism in pool boiling during the departure mode is replaced by

the transient heat conduction to the liquid slug trapped between the two elongated vapour bubbles. Transient conduction is followed by micro-convection in the liquid slug. Micro-convection induces circulation within the liquid slug and evaporation happens at the receding interface upstream. At the advancing interface in the slug, liquid comes in contact with the wall, which may be partially dry or may be covered with a thin liquid film. The liquid behind the interface begins to be heated due to transient conduction, and sweeps over the receding interface resulting in significant evaporation. Thus transient conduction followed by release of energy through evaporation at the interface is identified as the heat transfer mechanism in this configuration. In case of complete dry-out of the film, there may be an additional component due to enhanced heat transfer at the triple contact line, but this contribution, he expected to be quite small.

Contrastingly, Thome et al. [15] have suggested the thin film evaporation to be significant during elongated bubble (slug flow) regime. The varying opinions about the dominant mechanisms and their relative contributions make the development of physics based model, a challenging task even if it is only for a specific flow regime. Hence there are very few such models in the literature.

One such model is that of Jacobi and Thome [61], which was developed for prediction of the HTC in slug flow. Thome et al. [15] further refined the model. They argued that for the slug flow in microchannels, it is the thin film evaporation mechanism which is of paramount significance. According to the model, the local HTC, during the passage of liquid slug is much smaller compared to that during passage of vapour slug surrounded by a thin liquid film.

They considered a transient HTC which varied with the thickness of the thin liquid film around the vapour slug. The challenges that Thome et al [15] pointed out were that the model ideally requires knowledge about the critical nucleation radius to calculate the required superheat for initiation of boiling as well as the bubble frequency, the initial film thickness and the minimum film thickness. For comparison with a wide database, they chose the optimum values for the stated parameters and were able to predict 67% of the database to within 30% [62].

Pointing to significant deviations of HTC correlations developed for macro-channels in predicting the trend in HTC, Qu and Mudawar [14] developed a semi-analytical annular flow model. Features unique to two-phase micro-channel flow, such as laminar liquid and vapour flow, smooth interface, as well as strong droplet entrainment and deposition effects were incorporated into the model. Forced convection followed by evaporation of the thin film of liquid into the vapour core was considered as the heat transfer mechanism. Their model correctly captured the overall trend of decreasing and then increasing heat transfer coefficient with increasing vapour quality. Their model yielded a MAE of 13.3% for their experimental data.

Recently, Harirchian and Garimella [16] developed models similar to those of Thome et al. [15] as well as Qu and Mudawar [14]. However, they had to completely change the empirical constants used by the previous authors to achieve a reasonable fit with their experimental data. In fact, the decreasing and then increasing trend in the heat transfer coefficient observed by Qu and Mudawar [14] was not observed. They only observed an increasing trend. They

argued that they did not observe any entrapped liquid droplets in the vapour core during the annular flow and hence the droplet deposition mechanism was not considered.

In summary, the often diverging trends of especially the HTC, the multiplicity of mechanisms thought to be responsible for heat transfer and the reasonable predictions given by semi-empirical correlations and the semi-analytical models to usually only the parent data-sets rather than being generally applicable points to the fact that flow boiling in microchannels is very complex. The number of factors influencing the trends of HTC, flow regimes and heat transfer mechanisms may be more than that which are considered while developing correlations and semi-analytical models. Moreover, the highly transient nature of flow-boiling even for a given set of experimental parameters and flow regime makes it even more challenging to draw any concrete conclusions, especially on the basis of data that is time-averaged. Hence, the necessity to conduct transient heat transfer measurements synchronously with flow visualizations is felt herein. In recent years, some researchers [63–65] have worked towards fulfilling the need for such transient studies.

Freystein et al. [63] conducted synchronous study on a mini-channel and they obtained the temperature field with an Infra-red (IR) camera. They studied transient wetted surface heat flux with passage of slug during flow-boiling of FC-72. Rao et al.[64] conducted high frequency (10 kHz) temperature measurements synchronously with high speed flow visualization during sub-cooled

nucleate flow boiling in microchannels. They found that the local surface temperature fluctuations closely followed the events in the flow field. They could determine the relative importance of micro-layer evaporation, liquid phase cooling (forced convection), dry-out and re-wetting. Transient heat transfer coefficient was also computed, for which they used a finite element computational model by matching experimental temperature histories and boundary conditions. Bigham et al. [65] conducted a synchronized study and discussed the similarities and differences between flow boiling and pool boiling heat transfer mechanisms. There was a spike in heat flux and heat transfer coefficient during micro-layer/inter-line evaporation.

It can thus be seen that studies on transient heat transfer during micro-channel flow boiling are extremely limited. Many more detailed studies looking into the effect of various parameters such as the micro-channel/micro-gap dimensions, heat flux, mass flux, quality, coolant etc. are required to understand the effect of various parameters on heat transfer so that progress can be made towards a detailed understanding of heat transfer mechanisms and development of generally applicable models.

2.4 Prediction/Detection of Flow-regimes in Microchannels

Some researchers have attempted to develop regime-prediction techniques or techniques to diagnose flow regimes. Revellin and Thome [66] developed a flow pattern map for circular microchannels that had the mass velocity and the vapor quality as co-ordinates. Transition curves were determined using

Reynolds number, Weber number, Boiling number, fluid properties and microchannel dimensions. Regimes identified were isolated bubble regime, coalescing bubble regime, the annular zone and the post dry-out zone. Martin-Callizo et al. [18] noted that larger inlet sub-cooling shifted all transition lines (except for slug-annular/churn to annular flow) to earlier vapor qualities. Moreover, an increase in the saturation temperature shifted all transition boundaries toward higher vapor qualities. A comprehensive flow regime map was proposed by Harirchian and Garimella [16] based on their experiments on microchannels of several dimensions. Fluid properties, channel diameter, heat flux, mass flux as well as the heated length of the microchannels were considered and four regions namely slug, confined annular, bubbly, and alternating churn/annular/wispy-annular flow were plotted. It may hence be argued that there are a number of variables affecting flow-regimes and it indeed seems to be a very difficult task to develop a regime prediction method that is generally applicable.

Further, any modification to the wetted surface characteristics and/or the geometry of microchannel can add to the difficulty in development of a generic prediction method for regime detection. It was shown by Alam et al. [21] that transition from single phase to bubbly flow can be altered by changing the surface roughness. Even artificial nucleation sites (ANS) as shown by some researchers [1, 22, 23, 26] can alter the flow-regime and heat transfer mechanism. Yang et al.[28] showed that by having superhydrophilic silicon nanowires on the inner-walls of the microchannel, heat transfer can be very drastically enhanced by manipulation of prevalent flow regime. Some researchers

have also developed novel microchannel designs that can change heat transfer performance by changing prevalent regimes under certain experimental conditions [4, 29, 30].

Thus, development of a diagnostic tool for flow-regime detection seems to be a simpler alternative to the apparently very challenging problem of developing a generally applicable regime prediction method. Although, a diagnostic technique cannot fully replace flow-regime prediction techniques, it can still be of utility for certain applications. Smart feed-back loops that control flow-rate to control the prevalent flow-regime for optimal heat transfer performance and minimum pressure drop can potentially use detection techniques. Another application includes upcoming technology such as 3D IC packages. In fact, in recent times, researchers have shown interest in moving towards assessment of cooling solutions for modular thermal management of 3D-ICs consisting of multiple inter-layer microchannels. Kim et al. [67] and Koo et al. [68] carried out numerical and theoretical investigations respectively, to explore 3D IC cooling. Since a high speed camera cannot be used for regime detection in internal microchannels, a diagnostic technique can be useful.

Only Revellin et al.[69] developed a diagnostic tool based on a novel optical technique that could characterize flow pattern transition of two-phase flows. Their technique could determine bubble frequency, percentage of surviving small bubbles, lengths of bubbles and flow pattern transitions. However, it requires optical access for implementation. It is hence desirable to look into alternative techniques such as transient variations in temperature.

Chapter 3

Experimental Setup and Procedure

This chapter begins with a description of the test section and flow loop. Details regarding the calibration of temperature sensing diodes as well as the heat loss test are given. The procedure adopted for conducting the experiments is then explained.

3.1 Experimental Setup

3.1.1 Test-section

An exploded view and sectional view of the test-section are shown in Figures 3.1 and 3.2 respectively; while a photograph of the assembled micro-channel test section is as shown in Figure 3.3(a). The silicon test-chip (from Delphi Electronics) is flip-chip packaged onto the PCB (Printed Circuit Board) shown in Figure 3.3(b). The Pyrex glass (shown in Figure 3.1) insert is bonded to the Polycarbonate top-cover cavity and it provides good optical transparency required for flow-visualizations. A gap is formed between the surface of the silicon shown in Figure 3.3(b) and the pyrex glass insert. This gap acts as a finless low aspect ratio micro-channel.

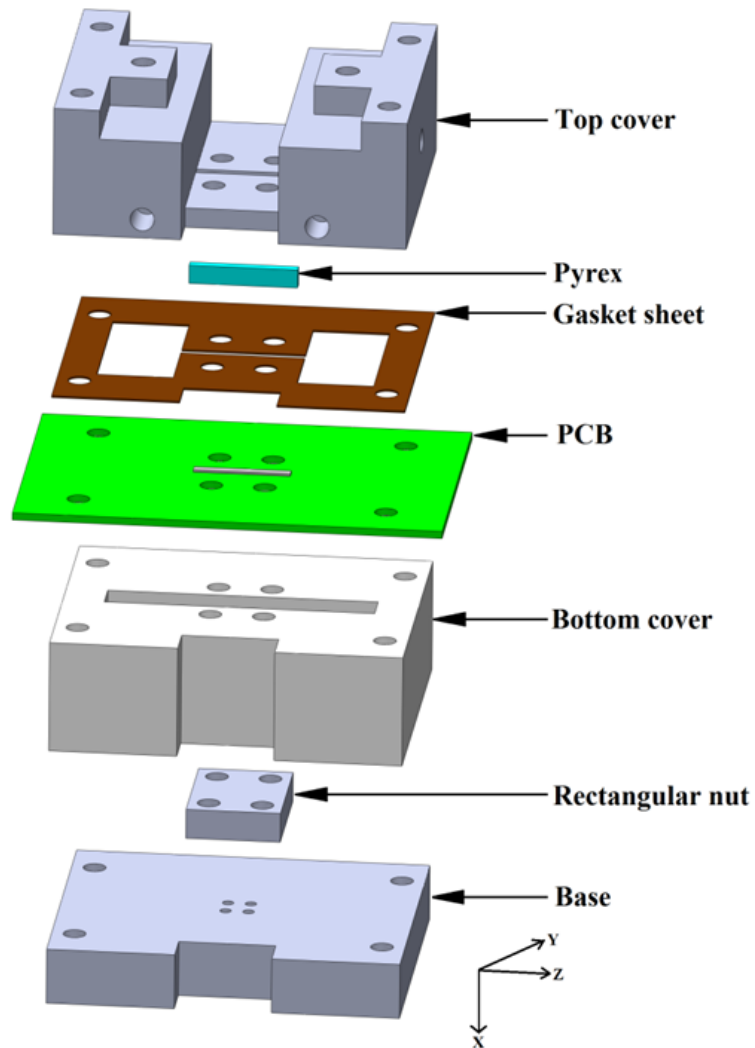


FIGURE 3.1: Exploded view of the assembled test-section

Gasket sheet between the Polycarbonate top-cover and the PCB acts as a sealant. The inlet and outlet plenums in the polycarbonate top cover, as seen in Figure 3.3(a), have fittings above them so that by slightly loosening them, the bubbles can be bled out. Two ports (see Figure 3.3(a)) are provided through which RTD (Resistance Temperature Detector) probes can be fitted to measure the fluid temperature at the inlet and outlet plenums. Similarly there are also two ports coming out of the other end of the plenums connected to the Pressure

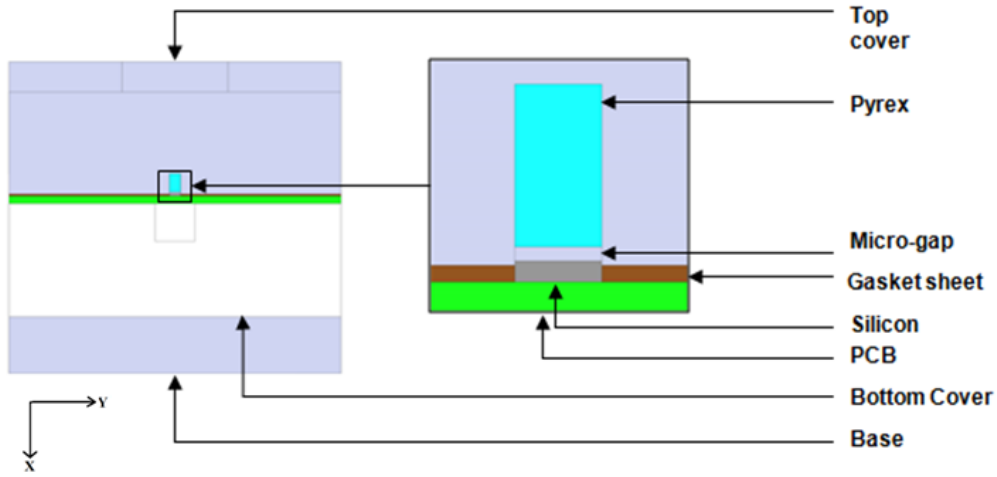


FIGURE 3.2: Sectional view along Z-mid-plane (plane of symmetry)

transducers. The teflon bottom cover has an air-gap so that it is better insulated leading to smaller heat loss from the bottom.

The microchannel width and length are $2540 \mu m$ and $25400 \mu m$ respectively and the height ranged from $0.14 - 0.42 mm$. The currently used silicon test-chip consists of an array of 10×1 thermal test dies (See figure 3.3(c)) $630 \mu m$ below the top (wetted) surface. Each of the thermal test dies has an area of $2540 \mu m \times 2540 \mu m$ and each of them consists of a heater and a diode. Each heater covers an area of $2000 \mu m \times 2000 \mu m$ and each doped diode temperature sensor covers an area of $400 \mu m \times 400 \mu m$ at the centre of the die. Each temperature sensor is a series connection of 5 diodes (p-n junction) with a total sensitivity of $-10 mV/^{\circ}C$.

It may be noted that the wetted silicon surface has a roughness of $Ra = 0.57 \mu m$ and $Rt = 5.45 \mu m$. The contact angle of water on silicon is 57° [26].

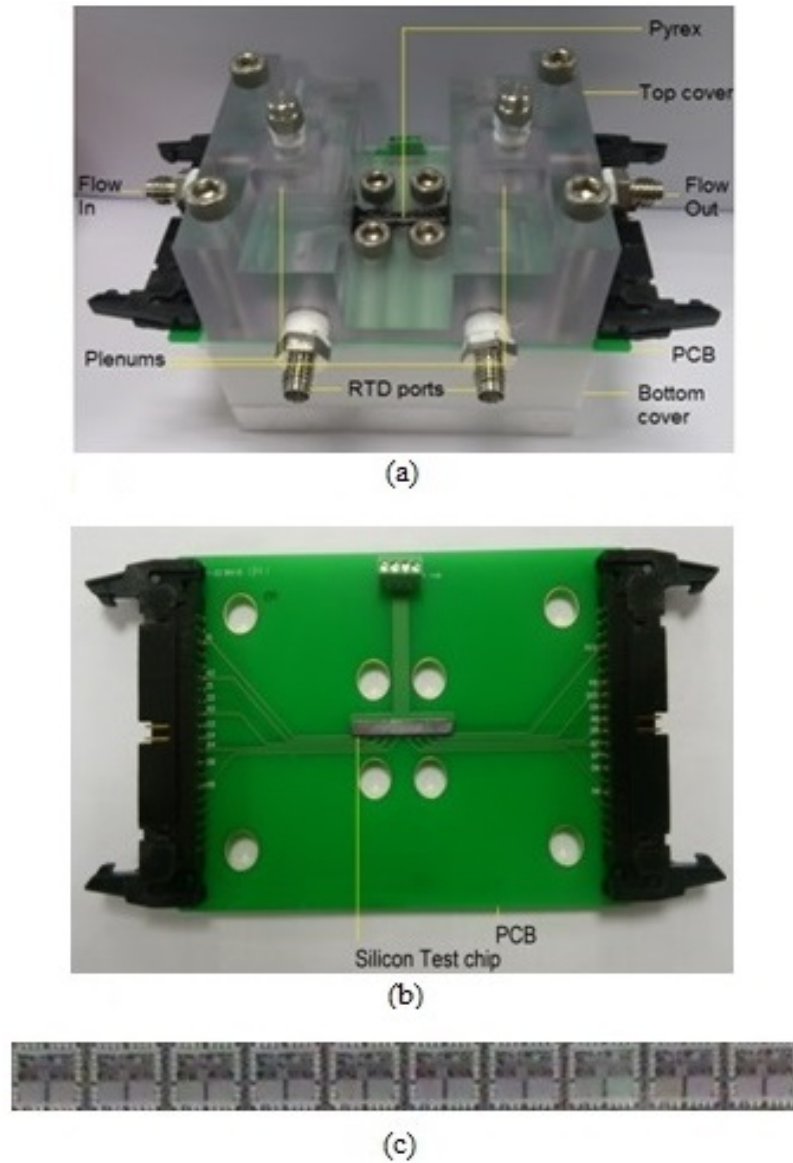


FIGURE 3.3: (a) Assembled test-section (b) Silicon test chip (wetted surface) on the PCB (c) 1 x 10 array of thermal test dies behind the silicon surface

3.1.2 Flow Loop

The flow loop schematic is as shown in Figure 3.4. The test-section is mounted on a X-Y stage so that it is easy to adjust the field of view of the camera. The temperature at the inlet and outlet plenums of the test-section are measured using RTDs (Omega 1/10 DIN class). At the inlet and the outlet plenums,

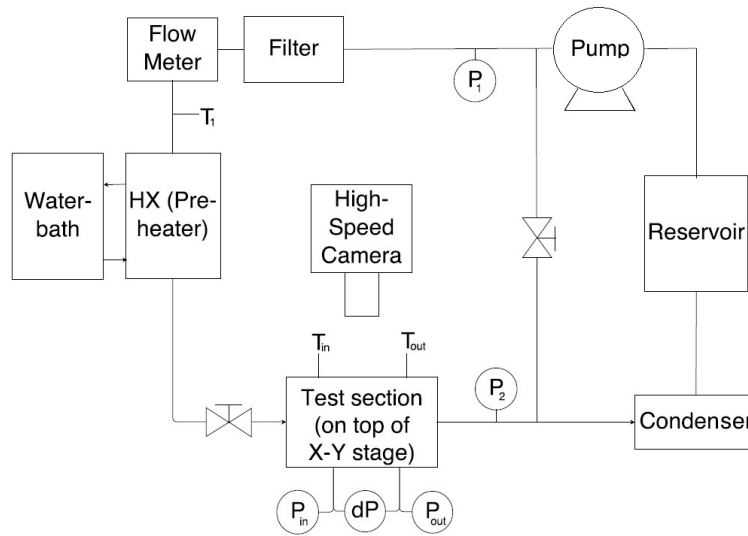


FIGURE 3.4: Schematic of the flow loop

gauge pressure was measured by Setra pressure transducers (Model 204) and the differential pressure was measured using Omega differential pressure transducer.

The reservoir is filled with de-ionized water. Immersion heaters (2 x 600 Watts) fitted into the reservoir are used to boil the water for degassing purpose. The gear pump (Micropump driven by Cole-parmer gear pump drive) drives the flow through the loop and the McMillan liquid flow sensor (Model 104) measures the flow rate. The water bath and liquid to liquid heat exchanger control the temperature of the fluid supplied to the test-section. Hot water that leaves the test section is cooled using a condenser (Theratron liquid-to-air heat exchanger (Model 735), before it flows back into the reservoir. All these components in the flow-loop were connected using Swagelok tubing.

The data from all the sensors were collected using a National Instruments

high speed Data Acquisition System. This system consists of a chassis (NI PXIe-1082), controller (NI PXIe-8135), a voltage module (NI PXIe-6363) and a RTD module (NI PXIe-4357).

High speed camera (Photron FASTCAM SA5) was used for flow visualization. A metal halide light source (Daitron MLDS250) provided the required lighting. However, if the light intensity was high, the measured (diode) temperature could increase by up to $1\text{ }^{\circ}\text{C}$. Similar phenomena was also reported by Rao et al. [64]. This problem was altogether avoided by keeping the light intensity very low and no temperature bias was observed. Yet, reasonably bright video quality was achieved by keeping the magnification and the frame rate of the video captured, relatively low.

3.2 Calibration of Temperature Sensors

First, calibration of the diode temperature sensors was carried out. For a constant current ($100\ \mu\text{A}$) the voltage drop across diodes is a linear function of temperature and the sensitivity is $-10\ \text{mV}/^{\circ}\text{C}$. The silicon test chip flip-chip packaged on to a PCB was placed inside a uniform-temperature forced convection oven along with a reference temperature sensor (Omega surface mount RTD) attached to the PCB.

Calibration was performed in the range of $40 - 120\text{ }^{\circ}\text{C}$ in steps of $10\text{ }^{\circ}\text{C}$. It took about 30 minutes to reach a steady-state when temperature fluctuations were reduced to within $\pm 0.05\text{ }^{\circ}\text{C}$. The voltage and temperature readings were then taken and calibration curve for each of the series of diodes was plotted.

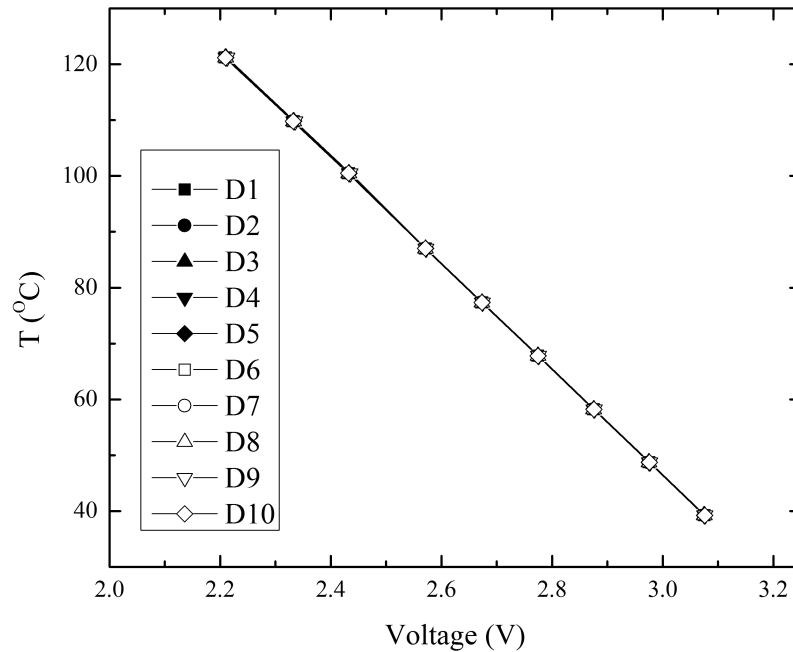


FIGURE 3.5: Calibration curves for diodes on the thermal test-chip

During actual experiments, this voltage-temperature relationship of each of the diodes was used to calculate the actual temperature. Figure 3.5 shows the calibration plot.

3.3 Characterization of Heat Loss

Before conducting the main experiments, heat-loss characterization was carried out. The heat loss occurring mainly through the bottom of the test section i.e. the heat loss that happens without the heat entering into the fluid within the channel, is estimated by conducting tests after the test-section is evacuated of the coolant. Power is supplied to the heaters and at a steady-state, all the heat supplied is lost. It takes about 30 minutes for the test-section to reach a

steady state, which is characterized by fluctuations of less than ± 0.1 °C for 5 minutes. Heat loss is plotted as a function of the average wall temperature. As shown in Figure 3.6, the relationship is linear. This method is similar to that adopted by Alam et al. [12]. For estimation of wall heat flux (during flow boiling experiments), this is the heat loss that is subtracted from the total heater power supplied.

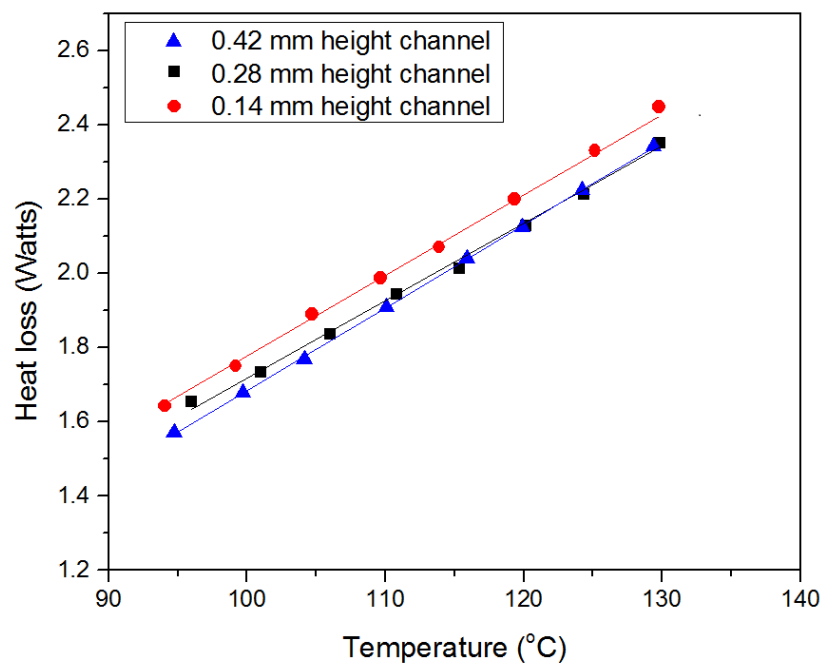


FIGURE 3.6: Heat loss vs. average substrate temperature

Out of the total heat that goes from the heated wall to the fluid, a part of it is convected by the fluid to the sides and top and then is lost to the ambient air, before the fluid goes to the outlet. Hence, the above heat loss is not the one used for estimation of mean temperature of the fluid at a cross-section. Instead,

since the cases presented herein are that of sub-cooled flow-boiling, linear interpolation of inlet and outlet plenum temperature gives a good estimate of mean temperature of fluid at a cross-section. This linearity can be easily understood from the equation (4.4) for sub-cooled boiling cases.

3.4 Experiment Procedure

Before each experiment session, degassing was carried out by vigorously boiling the de-ionized water in the reservoir for 2 hours after which the measured dissolved oxygen (DO) content was found to be ≈ 3.5 ppm. This DO measurement was done using a DO sensor (Fisher Scientific accumet AP84 meter) with a measurement uncertainty of ± 0.3 ppm. The boiled fluid was then cooled.

During actual experiments, flow rate as well as inlet fluid temperature were maintained throughout a session. Heat-flux was supplied/incremented and a quasi-steady state was considered to be achieved after the temperature fluctuations reduced to within ± 0.5 °C for 1 minute. A TTL signal was then sent by the camera to the DAQ thus triggering it to capture data synchronously with flow visualization. This data was captured at 10 kHz while the video was captured at a frame rate of 1 – 5 kHz, for a short duration of about 1 second. Under the same experimental conditions, data (not synchronous with video) was also captured at a frequency of 10 Hz for 5 minutes to get time-averaged values. The same procedure was repeated for several heat fluxes.

Chapter 4

Methodologies for Data Reduction

Since, some of the methodologies used for data reduction in this thesis are quite unique, this chapter exclusively deals with data reduction procedures. The steady state post-processing procedure is first presented. Next, the post-processing procedure for transient state heat transfer is presented. The discussion includes a literature review on the subject. The subsequent section deals with a procedure for post-processing to get a true frequency domain of temperature on the wetted surface, which is then used for identification of flow-regimes in the next chapter. Lastly, the estimated uncertainties in measured and derived quantities are presented.

4.1 Steady State Heat Transfer

The base heat flux is calculated by subtracting the heat loss happening through the bottom (as explained in Section 3.3) from the total heater power supplied and dividing it by the wetted/heated area. For measurement of the voltage drop across the heaters, the Kelvin connection (4-wire sensing) is used to eliminate the effects of voltage drops in the lead wires carrying high current, when calculating the voltage drop across the heaters. Current is calculated from

the voltage measurement across a shunt resistor connected in series with the load (heaters).

$$q_b(t) = \frac{VI - Q_l}{A_{ws}} \quad (4.1)$$

$$Q_l = V_l I_l \quad (4.2)$$

Wetted area is given as

$$A_{ws} = wl \quad (4.3)$$

Since, the bulk fluid is sub-cooled, the mean fluid temperature at a cross-section is given by energy balance assuming thermodynamic equilibrium condition [51, 64].

$$T_\alpha(z) = T_{in} + \frac{q_{fluid} w z}{m C_P} \quad (4.4)$$

The effective heat flux carried by the fluid for thermodynamic equilibrium condition is

$$q_{fluid} = \frac{m C_P (T_{out} - T_{in})}{wl} \quad (4.5)$$

Hence, this implies

$$T_\alpha(z) = T_{in} + \frac{(T_{out} - T_{in})z}{l} \quad (4.6)$$

Notice that q_{fluid} is different from q_b since after absorbing the heat flux q_b , the fluid also loses part of it through the top of the microchannel test section.

Wetted surface temperature is calculated from the sensor temperature, located $630\mu m$ below the surface assuming 1D conduction.

$$T_w(z) = T_{sensor}(z) - \frac{q_b t_s}{k_s} \quad (4.7)$$

Local heat transfer coefficient is calculated as

$$h(z) = \frac{q_b}{T_w(z) - T_\alpha(z)} \quad (4.8)$$

4.2 Transient Heat Transfer

During flow boiling in microchannels, high frequency temperature fluctuations occur on the wetted surface. The thermal diffusivity of the solid (wall material) leads to significant damping as well as lag of the measured temperature (generally at some distance away from the wetted surface) compared to the temperature variation occurring on the wetted surface. Such problems involving unknown boundary conditions (in this case, at the wetted surface) and known quantity at an interior location (such as temperature measured at an interior point within the solid), belong to ill-posed class of problems i.e., they yield large deviations in estimated quantities for small errors in measured data. Hence, estimation of variables is not straight-forward even for a one dimensional case. The use of simple direct numerical method would yield erroneous estimations (This would be seen later in Figure 4.3) due to noise involved in temperature

measurements and the ill-posed nature of the problem. In fact, noise in the temperature measurement data (which is some distance below the surface) can be misinterpreted as significant variation of temperature on the wetting surface.

This ill-posed problem is known as an inverse heat conduction problem (IHCP). To solve it, a suitable estimation algorithm that is efficient and minimizes the problem's sensitivity to noise [70], is required. There seems to be a promising scope of the use of such methods in conjunction with experimental temperature data (captured using fast-response temperature sensors) to study transient heat transfer along with synchronized flow visualizations at time scales small enough to capture boiling phenomena in microchannels. Before application of such methods, proper choice of certain variables, experimental as well as numerical, is necessary, since reliability of estimation results is sensitive to these. An uneducated guess of these parameters can lead to misleading results.

4.2.1 Literature Review

Methods to solve IHCP have been well compiled by Beck et al.[71] and Alifanov [72]. Some of the important methods to solve IHCP are functional specification method (variations include different functional relationships of heat flux with time), Tikhonov (zeroth, first and second order) regularization method and Iterative regularization method. A common approach is that an objective function, which involves the quadratic difference between measured and model imposed value of variables, is minimized. Blum and Marquardt [73] proposed an observer based method which is based on by-pass frequency filters, an approach

that is commonly used in Systems and Control theory. Moreover, Bayo et al. [74] suggested that low by-pass frequency filters can be used to eliminate the noise before applying the IHCP solution algorithm.

IHCP algorithms have over time been tested by various authors. Blum and Marquardt [73] used sinusoidal test-cases having non-dimensional angular frequencies of 5 and 20 and the ratio of noise to peak measurement signal of 0.2. A qualitative (graphical) assessment based on heat flux estimation was carried out. Raudenský et al. [75] tested IHCP algorithm using triangular heat transfer coefficient variation for noise of ± 1 , ± 2 and ± 5 °C. Su and Hewitt [76] used saw-tooth waveforms of heat transfer coefficient variation and tested two frequencies, 10 and 20 Hz to evaluate IHCP algorithms. The standard deviation in the noise tested were 0.1, 0.2 and 0.5 °C and data acquisition frequencies tested were 1 kHz and 10 kHz. They concluded that a standard deviation of 0.1 °C in the noise was well predicted and that the data acquisition frequency did not make a difference. Marquardt and Auracher [77] evaluated IHCP algorithm based on square heat flux variation of frequencies 5, 16 and 25 Hz. These aforementioned researchers carried out a qualitative assessment based on graphical comparison.

4.2.2 Scope

Sinusoidal test cases are used as recommended by Blum et al. [73] who pointed out that other test cases such as triangular and square wave-forms may not be sufficient to assess the algorithms for cases involving fast boundary condition dynamics. Moreover from application point of view, sinusoidal test cases

can offer better assessment, since experimentally measured temperature is often broken down into sine waves of various amplitudes and frequencies by Fast Fourier Transform (FFT).

Stloz's method (Direct numerical method) as well as some of the IHCP solution methods namely Functional Specification method-constant heat flux functional form, Functional Specification method-linear heat flux functional form [71] and Tikhonov First order Regularization method [71, 78] are first compared. In all cases, sequential estimation is carried out. Depending on performance and computational efficiency, one method is selected. Broadening the bounds of previous studies, a larger set of numerical and experimental variables are studied. Especially, the frequencies of sinusoidal temperature variation studied are high, noise to signal ratio is large and additionally, qualitative graphical comparison is supplemented with quantitative data ((%)MAE of heat transfer coefficient) to assess the performance of IHCP solution method under various cases.

The data acquisition frequencies (of temperature) studied are 1 kHz and 10 kHz implying time steps of 10^{-3} and 10^{-4} seconds corresponding to non-dimensional sampling time-steps (non-dimensionalized by dividing the time-step by t_s^2/α) of 0.13 and 0.013 respectively. The amplitudes and frequencies of sine wave temperature fluctuations (on wetted surface) studied are 0.1, 0.2, 0.6, 1 and 2 $^{\circ}C$ and 5, 30, 50, 100 and 300 Hz respectively, implying non-dimensional angular frequency of up to 15. Two standard deviations of the temperature measurement noise, 0.05 and 0.1 $^{\circ}C$ are studied to assess the IHCP solution method.

4.2.3 Test-case

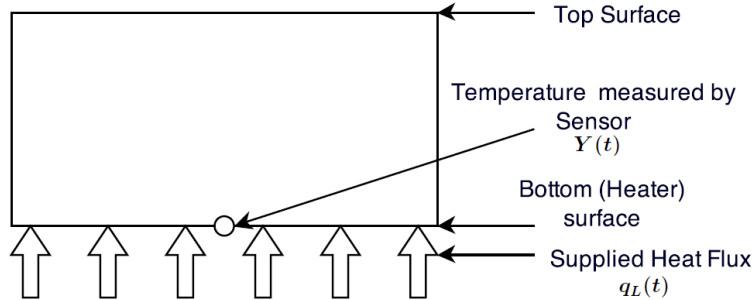


FIGURE 4.1: Schematic of solid domain

The 1-D test-case considered herein is that of a solid with known initial condition (temperature) and known bottom boundary conditions namely the supplied heat flux and temperature measured by sensor, as shown in Figure 4.1. Boundary conditions at the top surface are unknown. However to evaluate the methods to solve IHCP, a temperature signal is first simulated (Figure 4.2(a)) at the top surface, then the temperature (that should be measured by an ideal temperature sensor without any noise) is calculated at the sensor location (Figure 4.2(b)) using direct numerical method. The top surface temperature is then treated as unknown. Since all sensors and data acquisition systems are never ideal, to simulate the actual case, this temperature variation at the sensor location is corrupted with noise (Figure 4.2(c)) having a normal distribution. Lastly, using IHCP solution algorithm, the top surface/boundary temperature is estimated (Figure 4.2(d)) and is compared with the temperature signal that was first simulated at the top (Figure 4.2(a)). This is a standard method for evaluation of solution algorithms (see Alifanov [72] and Beck et al. [71]).

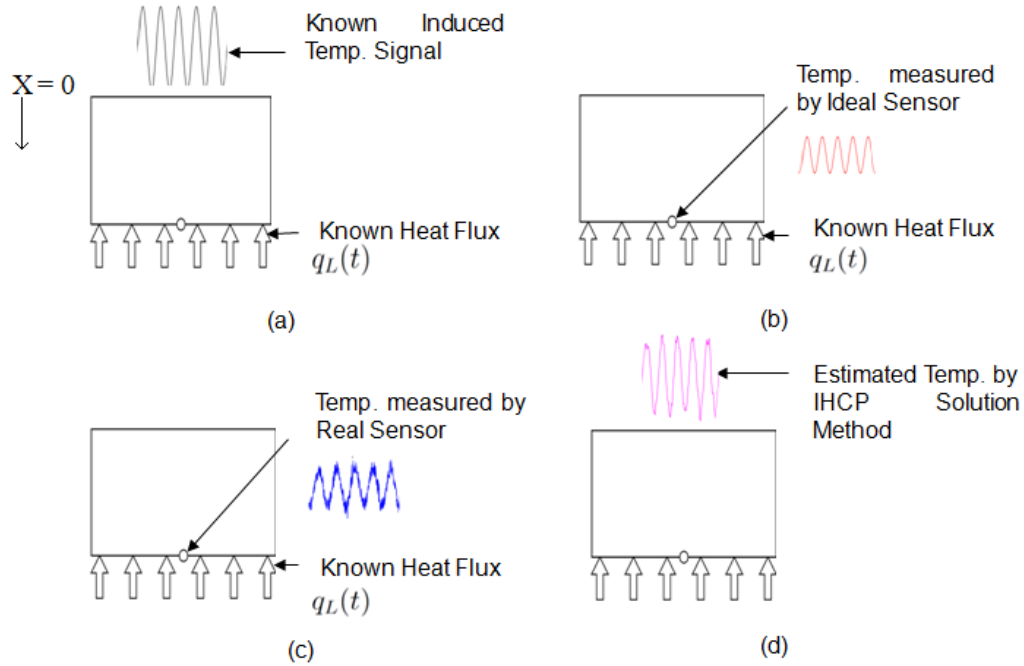


FIGURE 4.2: Testing of solution algorithm for IHCP

4.2.4 Mathematical Description

1D transient heat conduction equation is given as :

$$\rho c \frac{\partial T}{\partial t} = \frac{\partial}{\partial x} \left(k \frac{\partial T}{\partial x} \right) \quad (4.9)$$

The top surface temperature $T_w(0, t)$ and top surface heat flux $q_w(t)$ are unknown.

$$-k \frac{\partial T}{\partial x} \Big|_{x=0} = q_w(t) \quad (4.10)$$

The initial temperature T_0 is known too.

$$T(x, 0) = T_0 \quad (4.11)$$

The heat flux at the bottom surface q_b is known.

$$-k \left. \frac{\partial T}{\partial x} \right|_{x=L} = q_b \quad (4.12)$$

The temperature measured by temperature sensor at the bottom surface is given as

$$T(L, t) = T_{sensor}(t) = Y(t) \quad (4.13)$$

As discussed previously in this sub-section, to simulate $Y(t)$, a sine wave of the following form is induced at the top surface ($x = 0$).

$$T_{signal} = T_0 + A_1 \sin(2\pi ft) \quad (4.14)$$

Using the Finite Volume Method, equations (4.9) is solved using equation (4.11) as the initial condition and equations (4.12) and (4.14) as the boundary conditions. Temperature T_{ideal} measured by an ideal temperature sensor (i.e. $\sigma = 0$ or noiseless data) at the bottom surface is calculated. This temperature is corrupted by an additive error that has a normal distribution with a standard deviation σ , to simulate the real temperature sensors' measurements.

$$Y(t) = T_{ideal} + \omega\sigma \quad (4.15)$$

$Y(t)$ is then used in equation (4.13). As an initial condition, for equation (4.11), value of T_{signal} at some random time is used; this does not affect the

results. However, results for initial few milliseconds must be disregarded since in practice, T_0 is not known accurately throughout the solid domain and unlike uniform temperature represented by equation (4.11), in practice, the temperature is not actually uniform in the solid domain.

This linear equation (4.9) along with initial condition i.e. equation (4.11) and two boundary conditions at the bottom surface i.e. equations (4.12) and (4.13) can be solved using Stolz's method (Direct numerical method). However, as would be shown in Figure 4.3, the problem being ill-posed, IHCP solution method is required.

1. Function Specification Method: Constant heat flux functional form [71]

The objective for the function specification method is to minimize the function S (equation 4.16) with respect to top (wetted surface) surface heat flux q_M where M refers to the index of the current time-step. Function S is the summation for r future-time steps of the square of the difference between the sensor temperature Y and the numerical model imposed temperature T at the sensor location. Temporarily the heat flux q_M at time step t_M is assumed constant over r' future times. Future temperature information is used to reduce the sensitivity of the estimated heat flux to measurement noise and stabilize the computation as the time step size reduces. The heat flux q_M is determined such that the least square error between the model and experimentally measured temperatures is

minimized. The function S function is expressed as

$$S = \sum_{i=1}^r (Y_{M+i-1} - T_{M+i-1})^2 \quad (4.16)$$

where

$$T_{M+i-1} = \hat{T}_{M+i-1} |_{q_M=q_{M+1}=\dots=q_{M+i-1}=0} + \phi_i q_M \quad (4.17)$$

The resulting equation after minimization of S w.r.t q_M for the Function Specification Method-Constant heat flux functional form is

$$q_M = \frac{\sum_{i=1}^r (Y_{M+i-1} - \hat{T}_{M+i-1} |_{q_M=q_{M+1}=\dots=q_{M+i-1}=0}) \phi_i}{\sum_{i=1}^r \phi_i^2}, M = 1, 2 \dots M_{max} \quad (4.18)$$

where

$$\hat{T}_{M+i-1} |_{q_M=q_{M+1}=\dots=q_{M+i-1}=0} = T_0 + \sum_{n=1}^{M-1} q_n \Delta \phi_{M-n+i-1} \quad (4.19)$$

and the sensitivity coefficient for temperature at the sensor location and heat flux at the top surface is written as

$$\phi_i = \left. \frac{\partial T}{\partial q} \right|_{t_i} \quad (4.20)$$

$$\Delta \phi_i = \phi_{i+1} - \phi_i \quad (4.21)$$

2. Function Specification Method: Linear heat flux functional form [71]

For the linear heat flux functional form, heat flux is assumed to be varying

linearly. This linear equation is calculated based on the current and previous time-step's heat flux values. For this method, equation (4.18) is replaced by

$$q_M = \frac{\sum_{i=1}^r \psi_i (Y_{M+i-1} - \hat{T}_{M+i-1}|_{q_M=q_{M+1}\dots=0})}{\sum_{i=1}^r \psi_i^2} + q_{M-1} \frac{\sum_{i=1}^r \psi_{i-1} \psi_i}{\sum_{i=1}^r \psi_i^2} \quad (4.22)$$

where

$$\psi_i = \sum_{j=1}^i \phi_j \quad (4.23)$$

3. First Order Tikhonav Regularization Method [71]

First order Tikhonav Regularization Method adds a term to the minimization function S , the effect of this extra term is to reduce the magnitude of changes in heat flux from one time-step to the next.

$$S = \sum_{i=1}^r (Y_{M+i-1} - T_{M+i-1})^2 + \alpha_1 \sum_{i=1}^{r-1} (q_{M+i} - q_{M+i-1})^2 \quad (4.24)$$

Minimization of this function with respect to the top surface heat flux results in the following matrix formulation.

$$\mathbf{q} = [\mathbf{X}^T \mathbf{X} + \alpha_1 \mathbf{H}]^{-1} \mathbf{X}^T (\mathbf{Y} - \mathbf{\hat{T}}) \quad (4.25)$$

wherein

$$\mathbf{q} = \begin{bmatrix} q_M \\ q_{M+1} \\ \vdots \\ q_{M+r-1} \end{bmatrix} \quad (4.26)$$

$$\mathbf{X} = \begin{bmatrix} \Delta\phi_0 & 0 & 0 & \cdots & 0 \\ \Delta\phi_1 & \Delta\phi_0 & 0 & \cdots & 0 \\ \Delta\phi_2 & \Delta\phi_1 & \Delta\phi_0 & \cdots & 0 \\ \vdots & \vdots & \vdots & \ddots & \\ \Delta\phi_{M+r-1} & \Delta\phi_{M+r-2} & \Delta\phi_{M+r-3} & \cdots & \Delta\phi_0 \end{bmatrix} \quad (4.27)$$

$$\dot{\mathbf{T}} = \begin{bmatrix} \dot{T}_M|_{q_M=0} \\ \dot{T}_{M+1}|_{q_M=q_{M+1}=0} \\ \vdots \\ \dot{T}_{M+r-1}|_{q_M=q_{M+1}=\cdots=q_{M+r-1}=0} \end{bmatrix} \quad (4.28)$$

$$\mathbf{Y} = \begin{bmatrix} Y_M \\ Y_{M+1} \\ \vdots \\ Y_{M+r-1} \end{bmatrix} \quad (4.29)$$

$$\mathbf{H} = \begin{bmatrix} 1 & -1 & 0 & 0 & \cdots & 0 \\ -1 & 2 & -1 & 0 & \cdots & 0 \\ 0 & -1 & 2 & -1 & \cdots & 0 \\ \vdots & & \ddots & \ddots & \ddots & \\ 0 & 0 & \cdots & -1 & 2 & -1 \\ 0 & 0 & \cdots & 0 & -1 & 1 \end{bmatrix} \quad (4.30)$$

The value of α_1 is chosen based on the residual principle [72]. After the surface heat flux is calculated, the temperature distribution within the solid can be easily found out by direct numerical method using equations (4.9), (4.10), (4.11) and (4.12). The heat transfer coefficient at the top wetted surface is calculated as shown in equation (4.31), as suggested by Beck et al. [71].

$$h_i = \frac{q_i}{0.5(T_{1,i} + T_{1,i-1}) - T_\alpha} \quad (4.31)$$

In this equation, $T_{1,i}$ is the temperature at node 1 (top wetted surface) at time step i , $T_{1,i-1}$ is the same at time-step $i - 1$. q_i is the heat flux from the wetted surface between time-steps $i - 1$ and i .

For the test-cases simulated in this paper, the value of T_0 used was 115°C . The denominator (which is temperature difference between wetted surface and the fluid) of equation (4.31) ranged between 13 to 17°C and the bottom (supplied) heat flux was 30 W/cm^2 . These values were chosen so that the average value of h' are those that are typically encountered in flow boiling in microchannels (See Alam et al. [8], Balasubramanian et al. [13], Agostini et al. [46]) when

some of the common working fluids such as water or R236fa are used. It may be noted that any changes made to the value of heat flux and the range of the denominator of equation (4.31) would not in any way affect the trend in the surface temperature and heat transfer coefficient. The curve would simply shift by a factor. It may be noted that the thermal diffusivity of the solid and the depth of the sensor from the wetted surface are $5.5 \times 10^{-5} \text{ m}^2/\text{s}$ and $630 \mu\text{m}$ respectively.

4.2.5 Test-case Results and Discussion

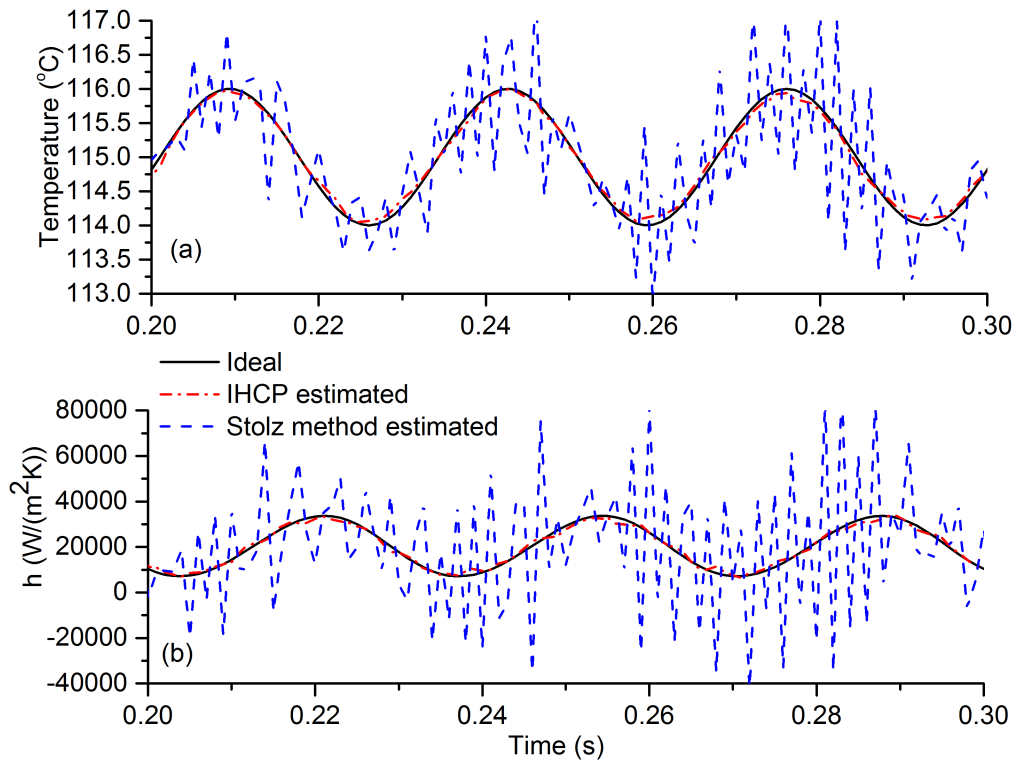


FIGURE 4.3: Direct Numerical (Stolz) method vs. Function Specification Method (Constant heat flux functional form) for $A_1 = 1 \text{ }^\circ\text{C}$ and $f = 30 \text{ Hz}$
 (a) Top surface temperature vs. time (b) Heat transfer coefficient vs. time

Figure 4.3(a) shows a comparison between temperature signal initially induced at the top surface (Ideal) using equation (4.14), surface temperature calculated using the Direct numerical method (or Stolz algorithm) and that using an

IHCP solution method (Function Specification Method) on simulated data at the sensor location. The utility of IHCP can be easily understood since the solution given by IHCP solution algorithm matches very well with the initially induced top-surface temperature, while that given by the direct numerical method is dismal. It may be observed that the errors in estimation of heat transfer coefficient in figure 4.3(b) are amplified compared to errors in temperature measurement. Also, since it is the heat transfer coefficient which is the general quantity of interest, evaluation of the IHCP solution algorithm for various cases is carried out by quantification of error in estimation of heat transfer coefficient rather than temperature. However, comparison of IHCP solution methods and optimization based on temperature estimation give results that are qualitatively similar.

Figure 4.4 shows a typical induced temperature signal on the top surface, the temperature measured by an ideal sensor located at the bottom surface and that measured by a real sensor (noise added to the ideal bottom temperature) at the same location. The temperature measured by the real sensor is then used in the IHCP solution algorithm to estimate the temperature at the top surface. It can be observed that amplitude of temperature fluctuation at the sensor location is significantly smaller compared to that at the wetted surface. This shows that there is significant amplitude attenuation. A noticeable phase difference is also observed. These are due to the finite thermal diffusivity of the solid. The amplitude attenuation as a function of the signal wave frequency is given in Figure 4.5. This is case specific depending on thermal diffusivity of the solid and the depth of the sensor from the top surface. The amplitude ratio is the ratio

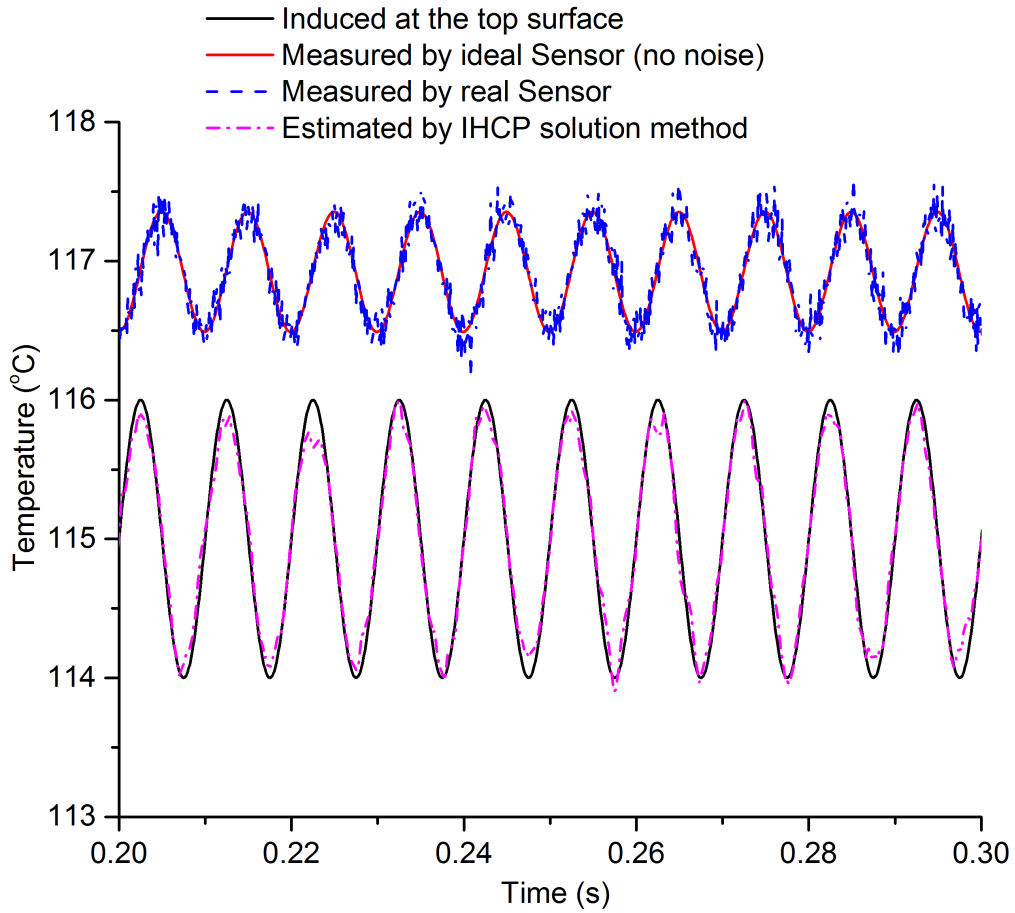


FIGURE 4.4: Induced temperature signal, signal measured by an ideal sensor, signal measured by a real sensor and the estimated signal using IHCP solution method for $A_1 = 1 \text{ } ^\circ\text{C}$ and $f = 100 \text{ Hz}$

of the amplitude of the signal captured by the sensor A_S to the signal (induced on the top surface) amplitude A_1 . This amplitude ratios are derived for several frequencies of the sine wave and are then plotted and curve fitted.

It may be noted that the graph plotted in Figure 4.5 can have general applicability for a similar problem if non-dimensional frequency given by Equation (4.32) is instead plotted on the top x-axis of Figure 4.5. Non-dimensionalization makes the damping independent of depth of the sensor and thermal diffusivity

of the solid substrate.

$$f^* = \frac{t_s^2}{\alpha} f \quad (4.32)$$

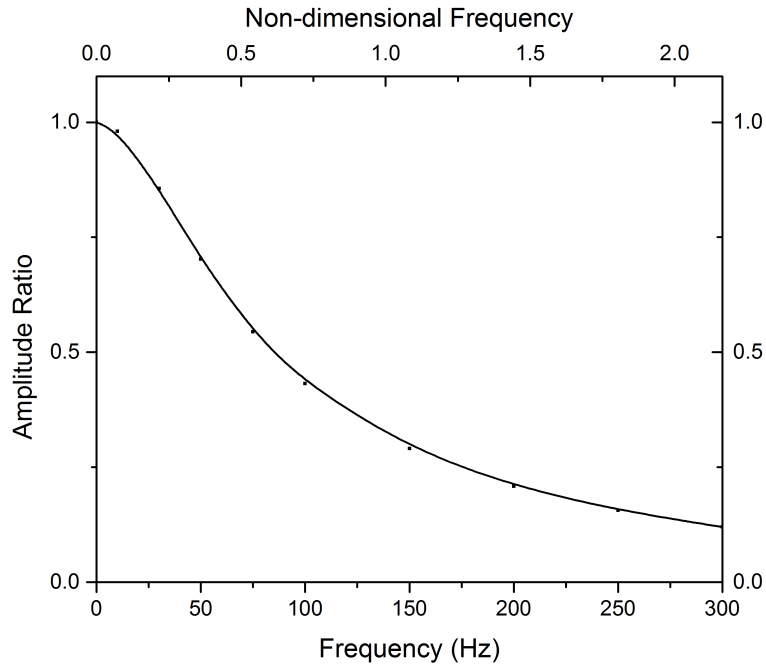


FIGURE 4.5: Amplitude ratio vs. frequency

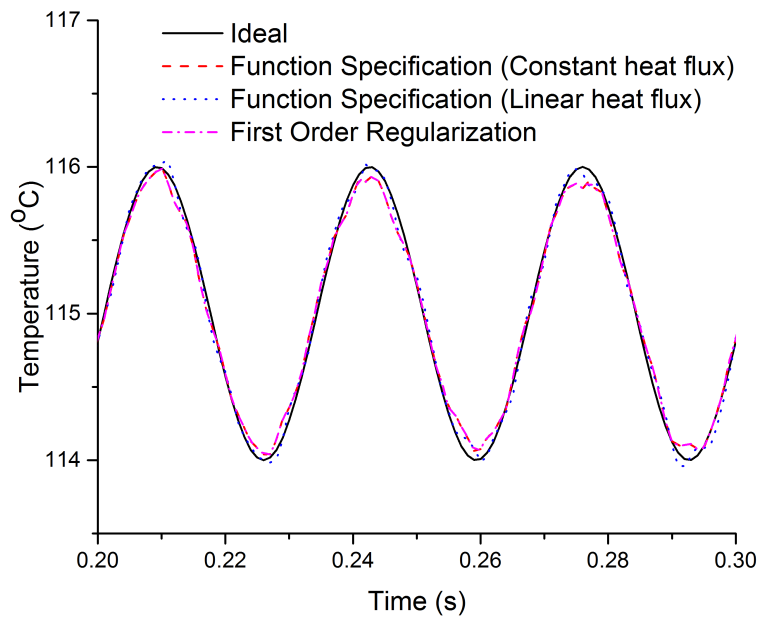


FIGURE 4.6: Comparison of IHCP solution methods

Figure 4.6 shows that the Beck's Function Specification Method-constant heat flux functional form, Function Specification Method-linear heat flux functional form and Regularization method give very similar results for optimal tuning parameter ' r '. Since the function specification method-constant heat flux functional form is the simplest and computationally most efficient, it was the preferred method and is the only method used henceforth. Although for brevity, only one set of amplitude and frequency is shown for comparison of the solution methods, it may be noted that other sets of amplitudes and frequency were tested too and the results from different methods were very close. Beck et al. [79] reached similar conclusions for their experimental test cases.

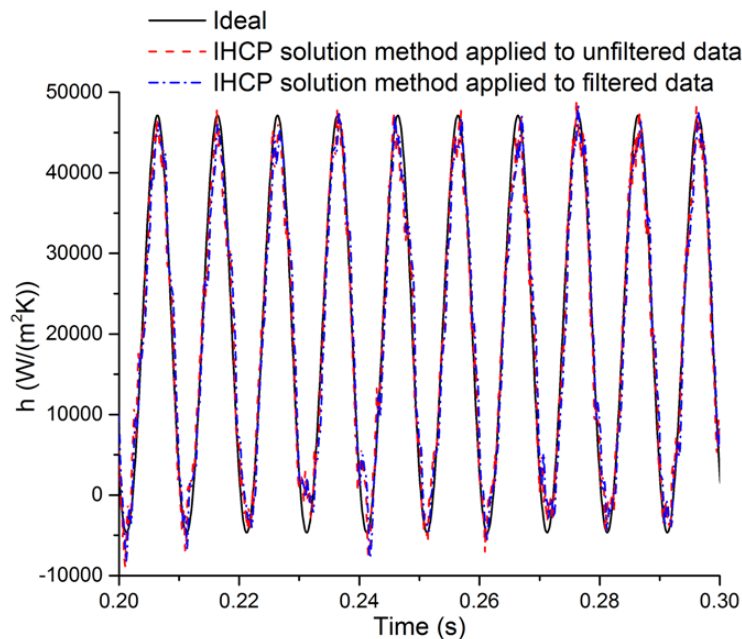


FIGURE 4.7: IHCP solution method applied to filtered and unfiltered data

Figure 4.7 shows the difference between raw data that is filtered (Low-pass Butterworth filter) and not filtered before using IHCP solution methodology. In general, no improvement was found in the estimation of the temperature and the

resultant heat transfer coefficient. Blum and Marquardt [73] reached a similar conclusion. So, filtering is not used henceforth.

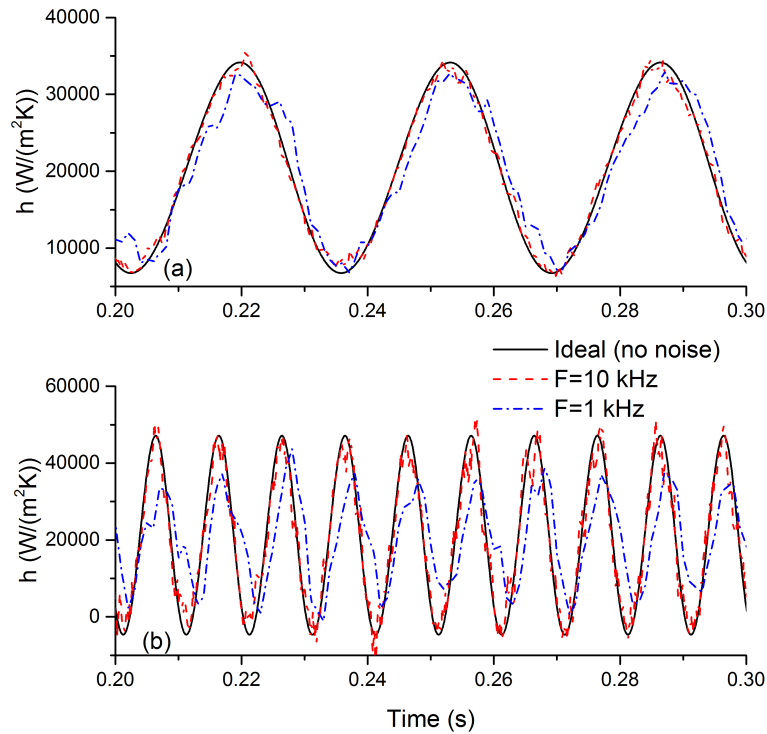


FIGURE 4.8: Comparison of data-logging frequency (a) $f = 30 \text{ Hz}$, $\sigma = 0.1 \text{ }^\circ\text{C}$ (b) $f = 100 \text{ Hz}$, $\sigma = 0.1 \text{ }^\circ\text{C}$

Quite noticeably a higher data logging frequency yields better results (see Figure 4.8). The difference in the results for lower and higher data logging frequencies is especially prominent at higher temperature signal frequencies.

Although in Figure 4.8(b), the heat transfer coefficient becomes very small and negative for a short while, such values are not actually encountered during flow-boiling experiments. The choice of different parameters for some of the numerical test-cases presented lead to such values. The higher the amplitude and frequency of temperature oscillations induced on the wetted surface, the greater are the fluctuations of the heat transfer coefficient. Although, in practical

applications, high frequencies and amplitudes are possible, actual temperature signature consist of a number of frequencies superimposed on each other in such a way that it would not lead to negative values of heat transfer coefficient. Also, when $'h'$ tends to zero, MAE(%) tends to infinity. Hence, a cut-off heat transfer coefficient is fixed at $5000 \text{ W}/(\text{m}^2\text{K})$ (since, generally the experimental heat transfer coefficient remained above this value) and the values below this are disregarded for comparison of Percentage Mean Absolute Error (% MAE).

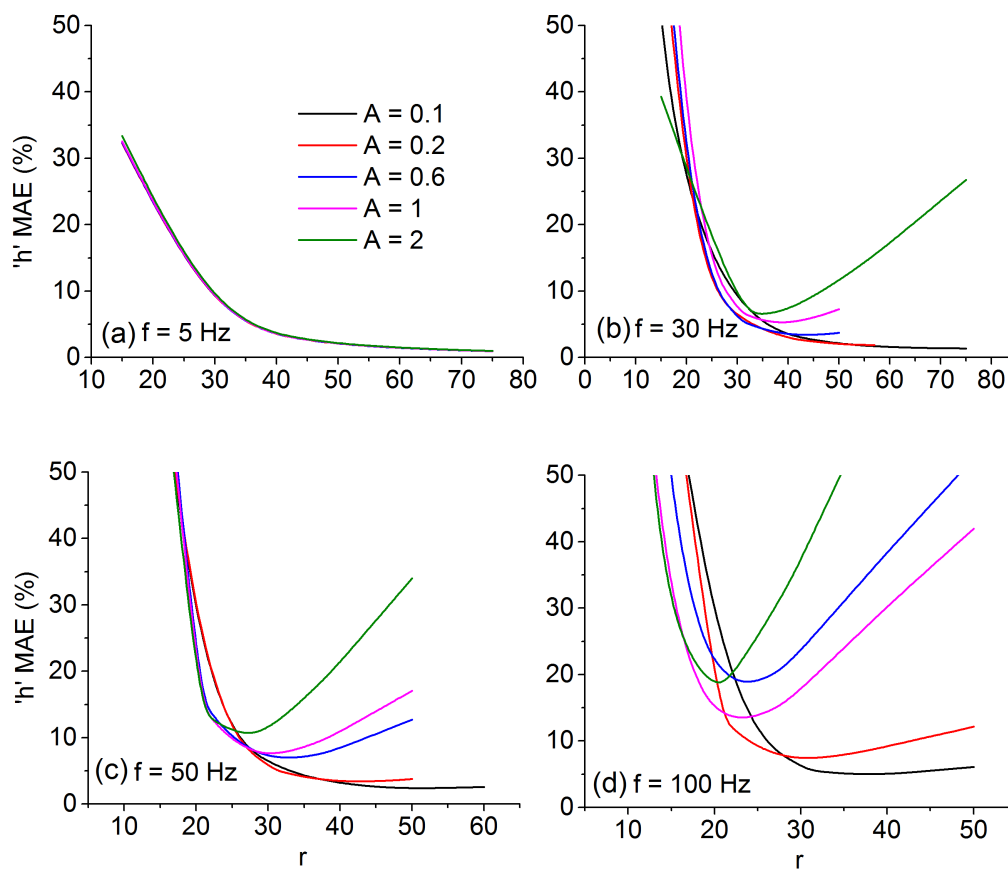


FIGURE 4.9: MAE(%) in Heat transfer coefficient vs. $'r'$ for $\sigma = 0.1 \text{ }^\circ\text{C}$, $F = 10 \text{ kHz}$ (a) $f = 5 \text{ Hz}$ (b) $f = 30 \text{ Hz}$ (c) $f = 50 \text{ Hz}$ (d) $f = 100 \text{ Hz}$

From Figure 4.9 it can be clearly observed that the success of the IHCP

solution methodology is dependent on r' . An unfortunate choice of the tuning parameter can lead to very poor estimations. As would be discussed later, 300 Hz frequency of temperature fluctuations is deemed unfit to be captured by this methodology and hence, has not been shown in Figure 4.9 for brevity. It may also be noted that for data logging frequency of 1 kHz, as well as for $\sigma = 0.05$ °C, the trends of r_{opt} are similar although the values are different.

The values of r_{opt} are summarized in Tables 1 and 2. After some of the optimization results were obtained, since it was observed that higher data-logging frequency gives better results, not all frequencies were tested for lower data-logging frequency of 1 kHz. It is interesting to note that for $F = 1$ kHz, although the Nyquist criteria is satisfied for frequency of 300 Hz, it was found that the sine wave trend could not be properly captured and hence 300 Hz frequency is not analyzed at 1 kHz data-logging frequency. For $F = 10$ kHz, $f = 5$ Hz, the optimum r' could have been higher but since the improvement in $MAE(\%)$ was insignificant after $r' = 75'$, further optimization was not carried out. For higher value of σ' , the optimum value of r' is higher. In general, for high f' and high A_1' , the r_{opt} was lower.

Figures 4.10 and 4.11 show the maximum and minimum of the tested amplitudes for all tested frequencies. Several important observations can be made from these figures and Table 4.1. The results are better for smaller value of σ' since the data is less corrupted. Unfortunately, σ can only be controlled to a limited extent during practical experiments. Its value as obtained from experiments was 0.1 °C. With increase in frequency, the predictions became worse. For a

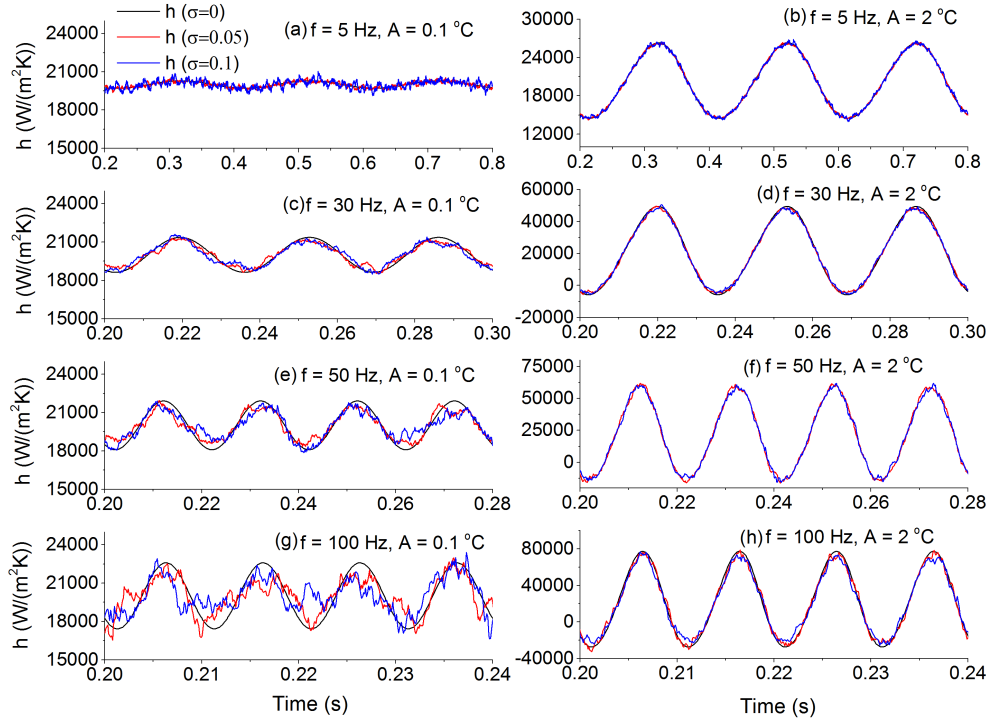


FIGURE 4.10: Heat transfer coefficient vs. time for $F = 10 \text{ kHz}$ (a) $f = 5 \text{ Hz}$, $A_1 = 0.1 \text{ }^\circ\text{C}$ (b) $f = 5 \text{ Hz}$, $A_1 = 2 \text{ }^\circ\text{C}$ (c) $f = 30 \text{ Hz}$, $A_1 = 0.1 \text{ }^\circ\text{C}$ (d) $f = 30 \text{ Hz}$, $A_1 = 2 \text{ }^\circ\text{C}$ (e) $f = 50 \text{ Hz}$, $A_1 = 0.1 \text{ }^\circ\text{C}$ (f) $f = 50 \text{ Hz}$, $A_1 = 2 \text{ }^\circ\text{C}$ (g) $f = 100 \text{ Hz}$, $A_1 = 0.1 \text{ }^\circ\text{C}$ (h) $f = 100 \text{ Hz}$, $A_1 = 2 \text{ }^\circ\text{C}$

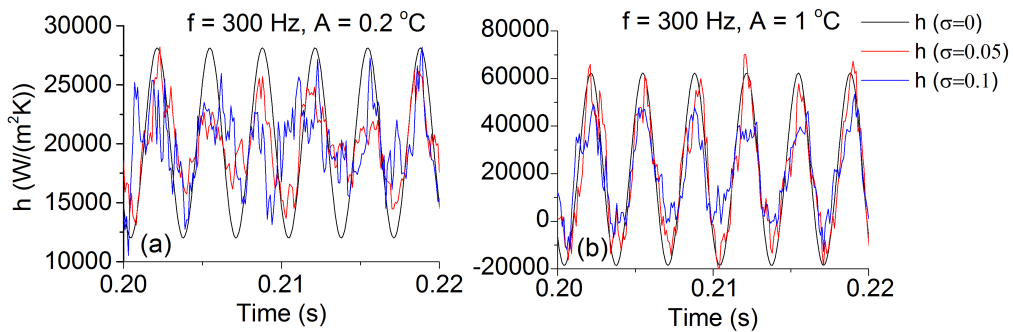


FIGURE 4.11: Heat transfer coefficient vs. time for $F = 10 \text{ kHz}$ (a) $f = 300 \text{ Hz}$, $A_1 = 0.2 \text{ }^\circ\text{C}$ (b) $f = 300 \text{ Hz}$, $A_1 = 1 \text{ }^\circ\text{C}$

TABLE 4.1: MAE(%) in heat transfer coefficient at data-logging frequency of 10 kHz

| f | σ | A_1 | A_s/σ | r_{opt} | h (%MAE) | f | σ | A_1 | A_s/σ | r_{opt} | h (%MAE) |
|-----|----------|-------|--------------|-----------|---------------|-----|----------|-------|--------------|-----------|---------------|
| 5 | 0.05 | 0.1 | 1.98 | 75 | 0.44 | 50 | 0.05 | 1 | 14.04 | 25 | 5.48 |
| 5 | 0.05 | 0.2 | 3.96 | 75 | 0.44 | 50 | 0.05 | 2 | 28.1 | 23 | 6.97 |
| 5 | 0.05 | 0.6 | 11.88 | 75 | 0.45 | 50 | 0.1 | 0.1 | 0.7 | 53 | 2.39 |
| 5 | 0.05 | 1 | 19.8 | 75 | 0.45 | 50 | 0.1 | 0.2 | 1.40 | 43 | 3.40 |
| 5 | 0.05 | 2 | 39.6 | 75 | 0.48 | 50 | 0.1 | 0.6 | 4.21 | 33 | 6.83 |
| 5 | 0.1 | 0.1 | 0.99 | 75 | 0.92 | 50 | 0.1 | 1 | 7.02 | 28 | 7.95 |
| 5 | 0.1 | 0.2 | 1.98 | 75 | 0.92 | 50 | 0.1 | 2 | 14.04 | 27 | 10.14 |
| 5 | 0.1 | 0.6 | 5.94 | 75 | 0.93 | 100 | 0.05 | 0.1 | 0.86 | 30 | 3.59 |
| 5 | 0.1 | 1 | 9.9 | 75 | 0.94 | 100 | 0.05 | 0.2 | 1.73 | 25 | 5.28 |
| 5 | 0.1 | 2 | 19.8 | 75 | 0.97 | 100 | 0.05 | 0.6 | 5.18 | 20 | 12.57 |
| 30 | 0.05 | 0.1 | 1.71 | 60 | 0.99 | 100 | 0.05 | 1 | 8.63 | 18 | 9.98 |
| 30 | 0.05 | 0.2 | 3.42 | 50 | 1.37 | 100 | 0.05 | 2 | 17.26 | 16 | 13.15 |
| 30 | 0.05 | 0.6 | 10.27 | 38 | 2.45 | 100 | 0.1 | 0.1 | 0.43 | 36 | 4.98 |
| 30 | 0.05 | 1 | 17.12 | 33 | 3.82 | 100 | 0.1 | 0.2 | 0.86 | 30 | 7.38 |
| 30 | 0.1 | 2 | 34.2 | 30 | 4.63 | 100 | 0.1 | 0.6 | 2.59 | 23 | 18.17 |
| 30 | 0.1 | 0.1 | 0.855 | 75 | 1.35 | 100 | 0.1 | 1 | 4.32 | 20 | 14.74 |
| 30 | 0.1 | 0.2 | 1.71 | 57 | 1.89 | 100 | 0.1 | 2 | 8.64 | 20 | 17.83 |
| 30 | 0.1 | 0.6 | 5.14 | 43 | 3.39 | 300 | 0.05 | 0.2 | 0.48 | 20 | 20.63 |
| 30 | 0.1 | 1 | 8.56 | 38 | 5.27 | 300 | 0.05 | 0.6 | 1.44 | 15 | 28.72 |
| 30 | 0.1 | 2 | 17.1 | 35 | 6.32 | 300 | 0.05 | 1 | 2.40 | 12 | 42.25 |
| 50 | 0.05 | 0.1 | 1.4 | 47 | 1.81 | 300 | 0.1 | 0.2 | 0.24 | 20 | 24.16 |
| 50 | 0.05 | 0.2 | 2.81 | 38 | 2.46 | 300 | 0.1 | 0.6 | 0.72 | 15 | 40.04 |
| 50 | 0.05 | 0.6 | 8.43 | 28 | 4.84 | 300 | 0.1 | 1 | 1.20 | 15 | 60.12 |

TABLE 4.2: MAE(%) in heat transfer coefficient at data-logging frequency of 1 kHz

| f | σ | A_1 | A_s/σ | r_{opt} | h (%MAE) | f | σ | A_1 | A_s/σ | r_{opt} | h (%MAE) |
|-----|----------|-------|--------------|-----------|---------------|-----|----------|-------|--------------|-----------|---------------|
| 30 | 0.05 | 0.2 | 3.42 | 7 | 2.4 | 50 | 0.1 | 0.2 | 1.40 | 6 | 5.7 |
| 30 | 0.05 | 0.6 | 10.27 | 5 | 4.2 | 50 | 0.1 | 0.6 | 4.21 | 4 | 12.0 |
| 30 | 0.05 | 1 | 17.12 | 4 | 6.5 | 50 | 0.1 | 1 | 7.02 | 4 | 13.2 |
| 30 | 0.1 | 0.2 | 1.71 | 8 | 3.5 | 100 | 0.05 | 0.2 | 1.73 | 3 | 9.2 |
| 30 | 0.1 | 0.6 | 5.14 | 6 | 6.3 | 100 | 0.05 | 0.6 | 5.18 | 3 | 25.9 |
| 30 | 0.1 | 1 | 8.56 | 5 | 9.5 | 100 | 0.05 | 1 | 8.63 | 2 | 26.4 |
| 50 | 0.05 | 0.2 | 2.81 | 5 | 4.4 | 100 | 0.1 | 0.2 | 0.86 | 4 | 12.3 |
| 50 | 0.05 | 0.6 | 8.43 | 4 | 8.9 | 100 | 0.1 | 0.6 | 2.59 | 3 | 31.4 |
| 50 | 0.05 | 1 | 14.04 | 3 | 9.5 | 100 | 0.1 | 1 | 4.32 | 3 | 34.1 |

given frequency and ' σ ' if the amplitude of sine wave is large, then although the signal to noise ratio ' A_s/σ ' is larger, the MAE(%) in ' h ' is generally not smaller. It is the combined effect of higher amplitude, higher frequency and higher noise which make the estimation of temperature more difficult. $f = 300 Hz$ is deemed unfit to be estimated for present work since MAE(%) is high and graphical trend too is not captured properly as can be seen from Table 4.1 and Figure 4.11 respectively.

For certain applications, it is the trend which is more important to capture than the actual value of heat transfer coefficient. Although from Table 4.1 it can be seen that predictions for smaller amplitudes for a given ' σ ' and frequency are better, graphically it is the larger amplitudes for which the IHCP solution algorithm is more successfully able to capture the trend. This is especially true for $f = 100 \text{ Hz}$ when fluctuation amplitude is small. Although the $MAE(\%)$ is small for smaller amplitudes, the graph shows that the trend captured does not give a good idea about the simulated sinusoidal signal. Small value of $MAE(\%)$ is due to large value of ' h' '. To avoid any misleading conclusions due to high ' h' ' by use of just $MAE(\%)$, it may be useful to note that for frequencies up to $f = 50 \text{ Hz}$ and all amplitudes, the peaks and valleys in heat transfer coefficient were captured to within $\pm 1000 \text{ W}/(\text{m}^2\text{K})$ accuracy, while for frequency of 100 Hz , for all amplitudes except for $A_1 = 2 \text{ }^\circ\text{C}$ the peaks and valleys in heat transfer coefficient values were in general captured to within $\pm 2000 \text{ W}/(\text{m}^2\text{K})$ accuracy.

4.2.6 Validation of IHCP Solution Method for Experiment Based Superimposed Sinusoidal Test-cases

Test cases used in Subsection 4.2.5 were pure sinusoidal temperature variations. To confirm the validity of those results for cases that are not pure sinusoids but have a temperature signal consisting of a number of superimposed sine waves, the IHCP solution method is tested on a more realistic temperature signal representing temporal temperature fluctuations during actual flow boiling

experiments. Two test cases are presented; each one consists of a few sinusoidal waves with frequencies and amplitudes selected from frequency domain of temperature-time variations obtained during actual flow boiling experiments.

Test Case 1

For the first test-case, FFT is done on transient temperature-data captured during flow-boiling experiments on a microchannel with height $420 \mu m$, at a mass flux of $200 kg/(m^2s)$ and heat flux of $17.2 W/cm^2$. Following the methodology which will be given in Section 4.3, amplitude in the frequency-domain of the sensor temperature were corrected and frequency-domain representative of wetted surface temperature is obtained as shown in Figure 4.12. The notable amplitudes and frequencies fall within the maximum amplitude and frequencies of sinusoidal temperature fluctuations tested numerically in Section 4.2.5. For $\tau' = 50$, the $MAE(\%)$ for all sinusoids falling within the range of amplitudes and frequencies in Figure 4.12 are 5 % (Figure 4.9).

Some of the representative amplitude and frequencies of the sine waves in Figure 4.12 are enlisted in Table 4.3. These have been superimposed on one another to form a temperature signal on the wetted surface. Figure 4.13 shows that IHCP solution methodology can estimate h' very well. The Percentage Mean Absolute Error ($MAE(\%)$) for the tested case was 5.4 % for value of future-time steps $\tau' = 40$.

Test Case 2

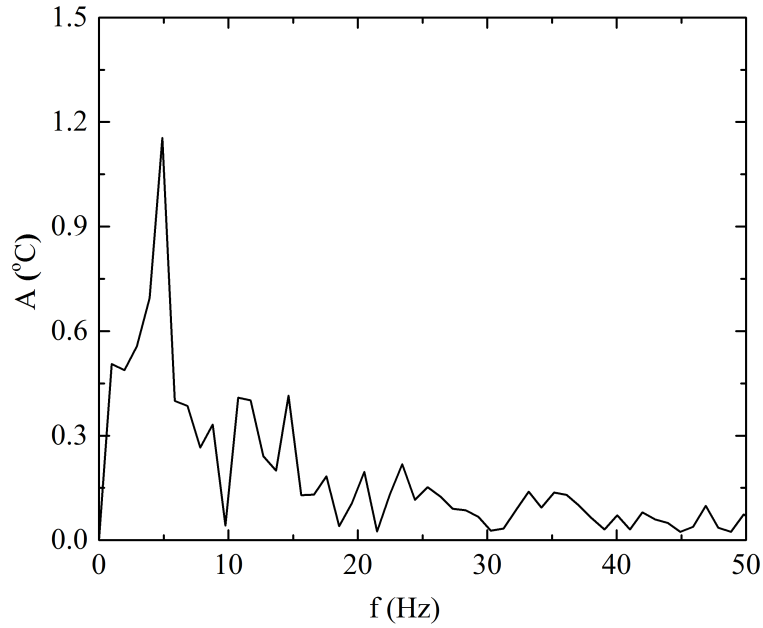


FIGURE 4.12: FFT for $G = 200 \text{ kg}/(\text{m}^2\text{s})$, $q_b = 17.2\text{W}/\text{cm}^2$

TABLE 4.3: Constituent sine-waves' frequency and amplitude for test-case 1

| No. | $f(\text{Hz})$ | $A_1(^{\circ}\text{C})$ |
|-----|----------------|-------------------------|
| 1 | 1 | 0.5 |
| 2 | 2 | 0.5 |
| 3 | 3 | 0.56 |
| 4 | 4 | 0.7 |
| 5 | 5 | 1.15 |
| 6 | 6 | 0.4 |
| 7 | 7 | 0.4 |
| 8 | 8 | 0.26 |
| 9 | 9 | 0.3 |
| 10 | 11 | 0.4 |
| 11 | 12 | 0.4 |
| 12 | 13 | 0.23 |
| 13 | 14 | 0.2 |
| 14 | 15 | 0.4 |
| 15 | 23 | 0.22 |
| 16 | 35 | 0.15 |
| 17 | 46 | 0.1 |

The same procedure was adopted as that of the previous test-case. The heat flux and mass flux were $32 \text{ W}/\text{cm}^2$ and $400 \text{ kg}/\text{m}^2\text{s}$ respectively for microchannel height of $420 \mu\text{m}$. Frequency domain of the temperature-time data is as shown in Figure 4.14 and the representative sine waves' amplitudes and frequencies are enlisted in Table 4.4.

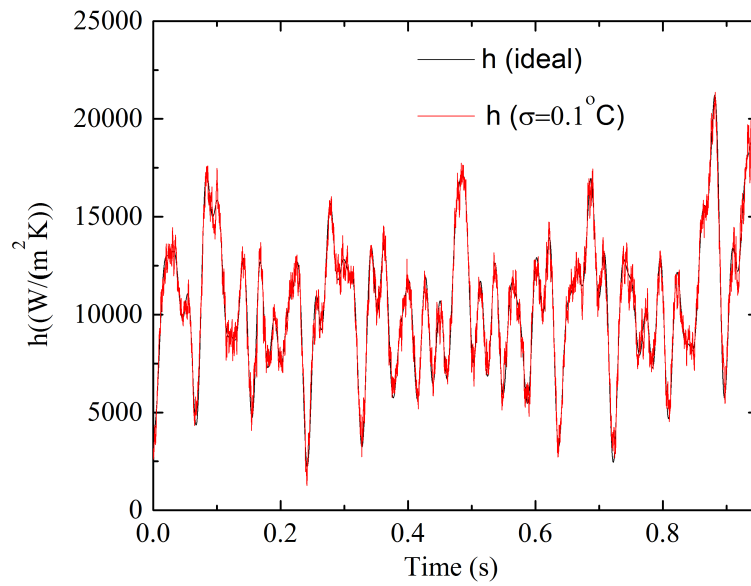


FIGURE 4.13: Assessment of IHCP solution method with superimposed sine waves as the test-case for $H = 0.42 \text{ mm}$, $G = 200 \text{ kg}/(\text{m}^2 \text{ s})$, $q_b = 17.2 \text{ W}/\text{cm}^2$

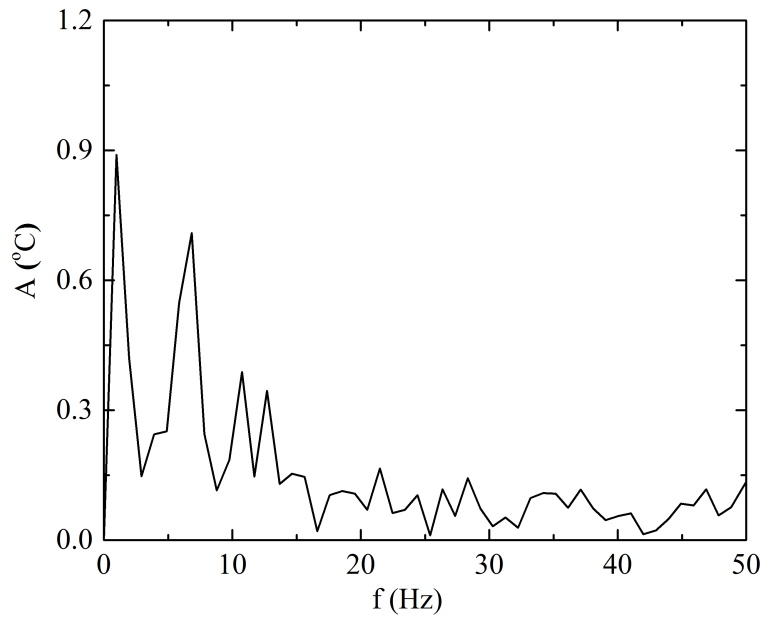


FIGURE 4.14: FFT for $G = 400 \text{ kg}/(\text{m}^2 \text{ s})$, $q_b = 32 \text{ W}/\text{cm}^2$

TABLE 4.4: Constituent sine-waves' frequency and amplitude for test case 2

| No. | $f(Hz)$ | $A_1(^{\circ}C)$ |
|-----|---------|------------------|
| 1 | 1 | 0.9 |
| 2 | 2 | 0.4 |
| 3 | 4 | 0.25 |
| 4 | 5 | 0.25 |
| 5 | 6 | 0.54 |
| 6 | 7 | 0.7 |
| 7 | 8 | 0.24 |
| 8 | 11 | 0.4 |
| 9 | 13 | 0.33 |
| 10 | 21 | 0.15 |
| 11 | 50 | 0.1 |

Just as the test-case 1, for optimum value of ' r' ', the $MAE(\%)$ for all sinusoids falling within the range of amplitudes and frequencies in Figure 4.14 are within 5 % (Figure 4.9) for ' $r' = 40$.

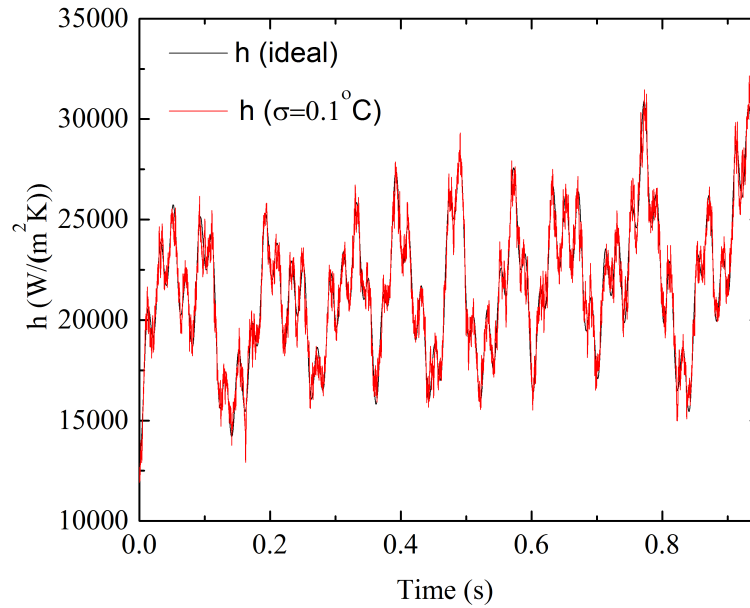


FIGURE 4.15: Assessment of the IHCP solution methodology with superimposed sine waves as the test-case for $H = 0.42 \text{ mm}$, $G = 400 \text{ kg}/(\text{m}^2\text{s})$, $q_b = 32 \text{ W}/\text{cm}^2$

The (%) MAE for this case is 2.7% for ' $r' = 40$. The graphical result has been depicted in figure 4.15. Hence, it is concluded that indeed individual sine-waves' results provide a good estimate of (%) MAE for superimposed waves,

typical of temperature variations observed during flow boiling experiments.

4.2.7 Summary

- (a) Use of conventional noise filter did not have any effect on the estimation of wetted surface temperature and the heat transfer coefficient.
- (b) Estimation of the heat transfer coefficient improved with increase in data-logging frequency. The improvement was especially more prominent for higher frequency temperature fluctuations.
- (c) It is the combined effect of high amplitude, high frequency and high noise which make the estimation of temperature more difficult.
- (d) From both, graphical results as well as quantitative results, it is concluded that frequencies up to 100 Hz can be captured well with a data-logging frequency of 10 kHz even for data that is corrupted with noise having a standard deviation of $0.1\text{ }^\circ\text{C}$. For frequencies up to $f = 50\text{ Hz}$, for all amplitudes, the peaks and valleys in the variation of ' h ' is captured within an error of $\pm 1000\text{ W}/(\text{m}^2\text{K})$ while for $f = 100\text{ Hz}$, for all amplitudes except $A_1 = 2\text{ }^\circ\text{C}$, are captured with a maximum error of $\pm 2000\text{ W}/(\text{m}^2\text{K})$.
- (e) The error in the estimation of heat transfer coefficient for pure sine waves gives a good estimate for more realistic cases for which a number of sine waves are superimposed on each other.

4.3 Fast Fourier Transform (FFT) of the Wetted Surface Temperature

Fourier analysis is performed using Discrete Fourier Transform (DFT) on the transient temperature measured by the diode sensor. DFT breaks down the signal into constituent sinusoidal signals of different frequencies and amplitudes. The governing equation for temperature distribution within the solid is the transient heat conduction equation (4.9). Because of thin substrate, temperature difference within the solid domain are small enough so that changes in substrate properties can be neglected. This implies that this equation (4.9) is linear. The principle of superposition is hence valid. Thus, the original signal can be broken down into a number of constituent signals.

The algorithm used for computing the DFT is Fast Fourier Transform (FFT). FFT transforms the time-dependent temperature signal into frequency domain data. During actual experiments, temperature measurement is done $630 \mu m$ below the wetted surface. The requirement however, is to get frequency domain of temperature on the wetted surface rather than that at the sensor location. However, the difficulty here is that due to finite thermal diffusivity of the silicon substrate, the temperature signal on the wetted surface gets damped as it penetrates the substrate.

To correct for this damping and to get the actual frequency domain that represents temperature variations on the wetting surface, amplitude ratio (damping) plotted in figure 4.5 is used. This amplitude ratio is a function of the sine

wave signal frequency. The amplitudes in the frequency domain (by FFT) of temperature-time data obtained from the sensor ($630 \mu m$ below the wetted surface) are then divided by these amplitude ratios (corresponding to the individual frequencies) and the frequency domain of the temperature signal at the wetting surface is thus derived.

4.4 Uncertainties

Diode sensors (embedded on Delphi Electronics Thermal Test Chip) and RTDs (Omega 1/10 DIN class) measure the temperature with an uncertainty of $\pm 0.4 \text{ }^\circ C$ and $\pm 0.12 \text{ }^\circ C$ respectively. The uncertainties in wall heat flux and heat transfer coefficient ranged from $\pm 0.73 - 2 \%$ and $\pm 1.64 - 3.75 \%$ respectively. The greatest contribution to the uncertainty in heat transfer coefficient measurement comes from temperature measurement errors. However, since the inlet sub-cooling is substantial, the temperature difference between the fluid and wall is substantial and hence the relatively low values of uncertainty in heat transfer coefficient. Differential pressure transducers and gauge pressure transducer readings have an uncertainty of $\pm 0.14 \text{ mbar}$ and $\pm 1.92 \text{ mbar}$ respectively. The uncertainty in pressure measurement was found to be in the range of $\pm 0.28 - 5.6\%$. Flow rate was measured with an uncertainty of $\pm 0.5 \text{ ml/min}$. Uncertainty for geometrical dimension measurements is $\pm 10 \mu m$. The uncertainty analysis according to that proposed by Taylor[80] is briefly discussed in Appendix A.

Chapter 5

Results and Discussion

This chapter presents the major experimental results of this thesis and the relevant discussion. A description of microchannels tested and the experimental conditions is given first. Next, the pressure drop data as well as the boiling curve for various conditions is presented and explained. Variation of time-averaged heat transfer coefficient is also studied with various microchannel heights and mass fluxes. The uniqueness of this study is that in addition to time-averaged study of heat transfer variables, a detailed transient study coupled with flow-visualization (captured synchronously with data) is presented. This has given detailed insights into the mechanisms of heat transfer. Lastly, based on temperature signature, it is found that flow regimes can be distinguished.

It may be noted that the presented heat transfer variables are for data captured by diode 8 (diode 1 is the most upstream while diode 10 is the most downstream). The reason for the choice of this diode is because it is nearly in center of the field of view of the high speed camera used to capture video frames when it was adjusted towards the most downstream end of the microchannel.

For all the conditions presented in Table 5.1, inlet fluid temperature was 86 °C. Notice the range of heat flux for various cases. For each case, the

TABLE 5.1: Microchannel dimensions and experimental test conditions

| <i>Case</i> | <i>W</i> (<i>mm</i>) | <i>H</i> (<i>mm</i>) | <i>D_h</i> (<i>mm</i>) | <i>G</i> actual (nominal) (<i>kg/(m²s)</i>) | <i>q_b</i> (<i>W/cm²</i>) | <i>Co</i> [42] | <i>D_{tran}</i> [43] (<i>mm</i>) |
|-------------|---------------------------|---------------------------|---------------------------------------|---|---|-------------------|---|
| 1.1 | 2.54 | 0.14 | 0.265 | 557 (600) | 0-29 | 9.51 | 3.27 |
| 1.2 | 2.54 | 0.14 | 0.265 | 994 (1000) | 0-44 | 9.51 | 1.01 |
| 2.1 | 2.54 | 0.28 | 0.504 | 393 (400) | 0-36 | 5.01 | 6.59 |
| 2.2 | 2.54 | 0.28 | 0.504 | 600 (600) | 0-46 | 5.01 | 2.82 |
| 2.3 | 2.54 | 0.28 | 0.504 | 998 (1000) | 0-105 | 5.01 | 1.01 |
| 3.1 | 2.54 | 0.42 | 0.721 | 182 (200) | 0-27 | 3.5 | 30.8 |
| 3.2 | 2.54 | 0.42 | 0.721 | 380 (400) | 0-50 | 3.5 | 7.05 |
| 3.3 | 2.54 | 0.42 | 0.721 | 580 (600) | 0-60 | 3.5 | 3.02 |
| 3.4 | 2.54 | 0.42 | 0.721 | 1028 (1000) | 0-94 | 3.5 | 0.954 |

maximum heat flux was determined by maximum of the transient wall temperature encountered during experiments. Even though the time-averaged maximum temperature would quite often be less than 110 °C, the very seldom dry-outs could sometimes cause over-shoot in wall temperature to above 150 °C. Such high wall temperature often lead to the failure of the test-chip, either due to softening of the solder bumps connecting the test-chip to the PCB (by flip chip packaging) or due to mechanical failure of the solder bumps due to thermal stresses induced on account of difference in thermal expansion of the silicon test chip and PCB material. Due to this reason, high wall heat fluxes could not be tested and sub-cooled boiling prevailed for all cases even for the most downstream region.

Confinement number [42, 81] (equation 2.1) was always large. Also, the value of D_{tran} ([43]) (equation 2.2) is larger compared to diameter of all microchannels used in this study. Hence, under all tested conditions, the term "microchannel" is considered most appropriate. However, it may be noted that the aspect ratio (H/W) of all microchannels is small. Yet, the aspect ratios

are much larger compared to the that of so called micro-gaps used by some researchers [21, 82].

Figure 5.1 shows various flow regimes observed during experiments conducted under conditions mentioned in table 5.1. Location of diode 8 is shown by a blue dot.

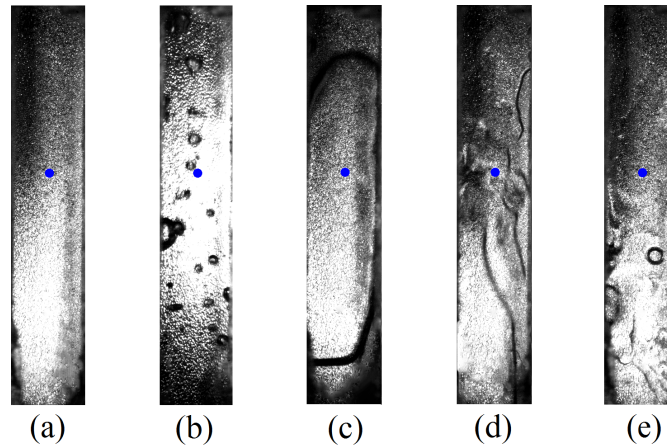


FIGURE 5.1: Flow regimes observed during experiments were (a) Single phase flow (b) Bubbly flow (c) Slug flow (d) Churn flow (e) Wispy Annular flow

5.1 Pressure Drop Characteristics

Figure 5.2 shows the effect of microchannel height on pressure drop plotted as a function of heat flux for various mass fluxes. For low heat fluxes, single phase flow was observed. With increase in heat flux, temperature increases which reduces the viscosity of the fluid and hence up to a certain value of heat flux until which single phase flow was observed, the pressure drop decreases somewhat. After commencement of phase change process, the pressure drop increases monotonically with increase in heat flux except for the case for microchannel with height 0.42 mm at a mass flux of $1000 \text{ kg}/(\text{m}^2\text{s})$. This is due

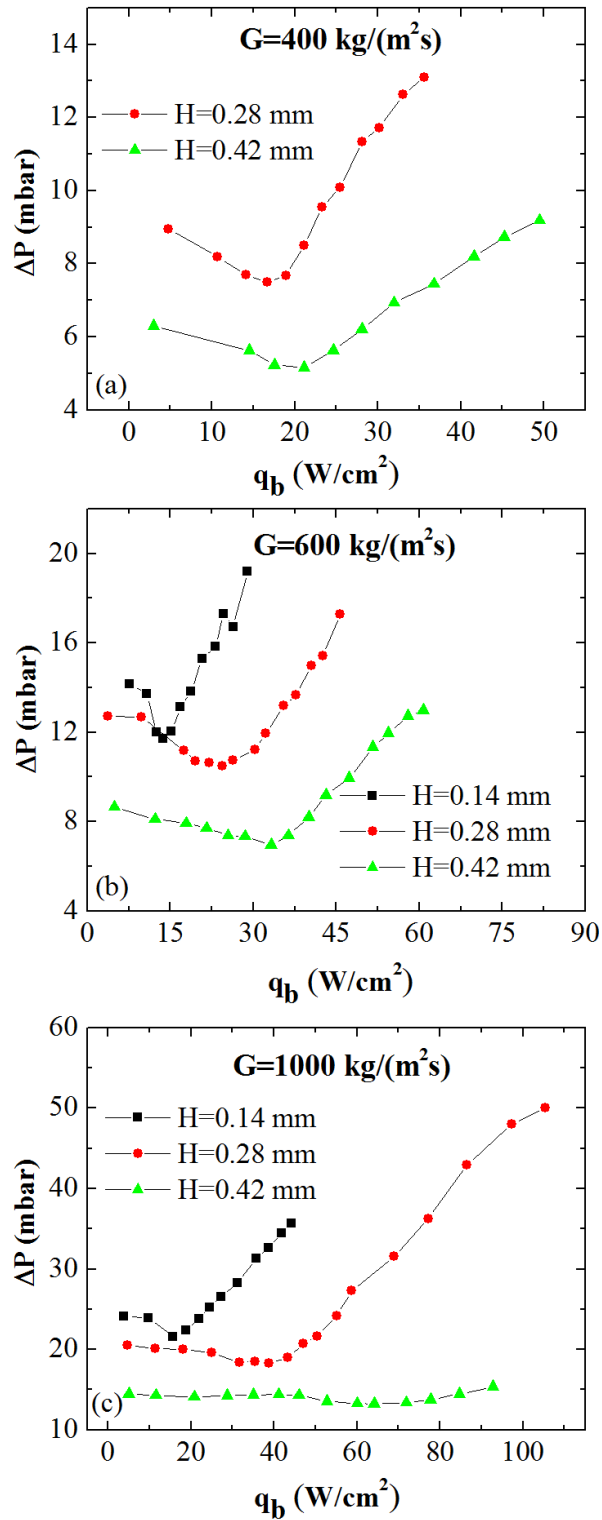


FIGURE 5.2: Effect of microchannel height on pressure drop versus heat flux curves for various mass fluxes

to the fact that as heat flux increases, the vapour quality increases which leads to greater accelerational pressure drop.

It can also be observed that for smaller microchannel heights, the pressure drop is larger since frictional pressure drop larger as well as the accelerational pressure drop is larger due to greater quantity of vapour generated in the coolant flowing through microchannel with smaller heights, for a given value of heat flux. It is also worth noting that the slope of pressure drop verses heat flux curve is steeper for smaller channels compared to larger ones. This was also observed by Harichian and Garimella [10].

While for microchannel with height 0.42 mm , at a mass flux of $1000\text{ kg}/(\text{m}^2\text{s})$ bubbly flow was observed, slug flow was the dominant flow regime for other cases. Hence for the former case, the pressure drop is insensitive to heat flux as also observed by Alam et al.[12].

In Figure 5.2(b), for microchannel with height 0.14 mm , there is a slight anomaly in the trend since pressure drop decreases for a heat flux of $25\text{ W}/\text{cm}^2$. Boiling is stochastic in nature. Pressure drop is influenced by the nucleation site distribution, the number of nucleation sites, etc. which can change with change in heat flux. Moreover, since it is sub-cooled boiling and the channel is long; there could have been more instances of nucleation and detachment of small bubbles and their collapse in the upstream for this heat flux compared to slightly lower heat flux which led to lower pressure drop.

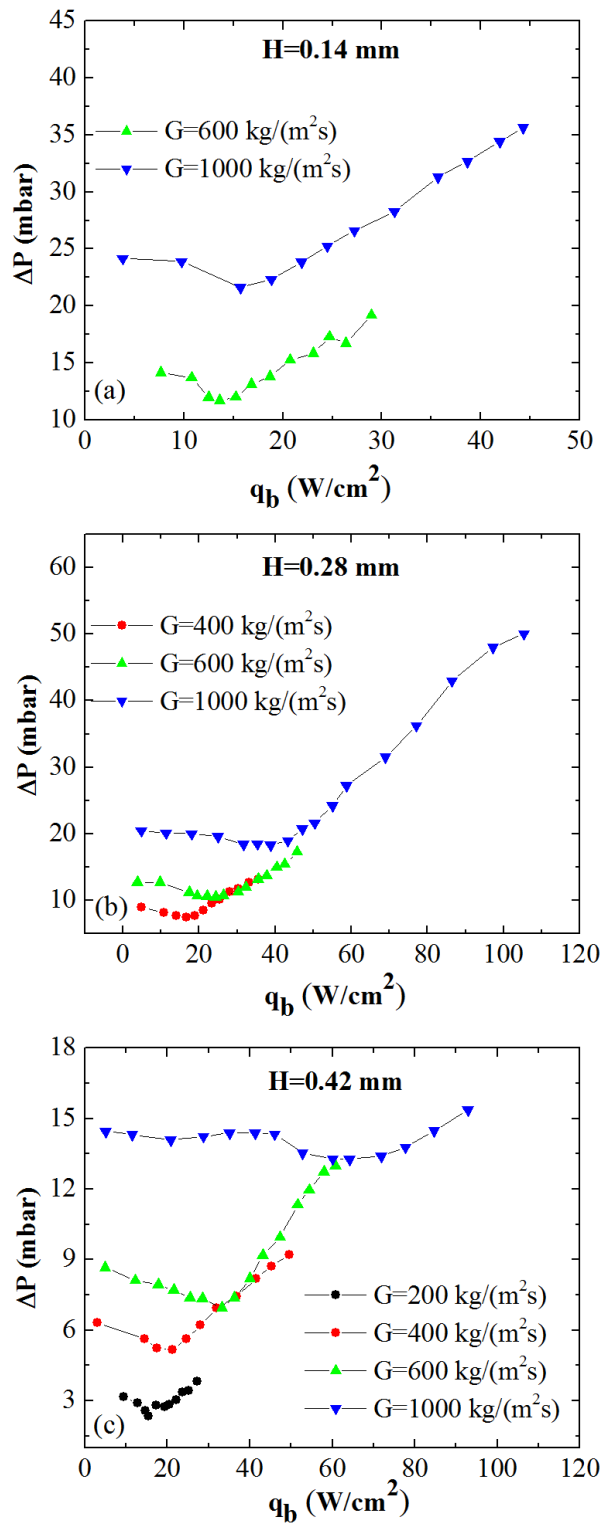


FIGURE 5.3: Effect of mass flux on pressure drop versus heat flux curves for various microchannel heights

Figure 5.3 shows the effect of mass flux on pressure drop versus heat flux curve for three microchannel heights tested. In general, pressure drop increases as the mass flux increases, since the frictional pressure drop component is more dominant. However, the pressure drop due to the accelerational component is greater for smaller mass fluxes since for smaller mass fluxes, the amount of vapour generated for a given heat flux is greater. Hence, it is sometimes possible to see, the pressure drop trend to be contrary to what is generally seen herein. It can be noticed from Figures 5.3(b) and (c) that for $G = 400$ and $600 \text{ kg}/(\text{m}^2\text{s})$, that the pressure drop is the same for several values of heat flux. Thus, for these cases, the increase in frictional component of pressure drop with mass flux is balanced by decrease in accelerational pressure drop with increase in mass flux. Such mass flux independence of pressure drop was also noted by Chen and Garimella [83].

5.2 Heat Transfer Characteristics

5.2.1 Boiling Curves

Curves shown in this sub-section are for time-averaged variables. Figure 5.4 shows the effect of microchannel height on the boiling curve for various mass fluxes. ONB (Onset of Nucleate Boiling) is characterized by a sudden change in slope of the curve. For heat flux beyond this point, slug flow was the main flow boiling regime observed except for microchannel height of 0.42 mm at a mass flux of $1000 \text{ kg}/(\text{m}^2\text{s})$ as well as for mass flux of $600 \text{ kg}/(\text{m}^2\text{s})$ below heat flux of $28.6 \text{ W}/\text{cm}^2$. For those conditions, bubbly flow was observed.

In the single phase region, the slope is not steep. In two phase region, as the wall heat flux increases, generally the wall superheat (difference between the temperature of the wall and the local saturation temperature of the fluid) increases. However, at times it is seen that the slope of the curve becomes negative implying a decrease in wall superheat with increase in heat flux. This is because the liquid is superheated before nucleation occurs and then the temperature suddenly drops as bubbles nucleate.

For smaller microchannel heights, ONB occurs at a smaller wall superheat. Moreover, for two-phase region, wall superheat is lower for smaller microchannel heights. This is due to more amount of vapour being generated for smaller heights for a given heat flux and greater confinement effects.

Figure 5.5 shows the effect of mass flux on the boiling curve for various microchannel heights. For smaller mass fluxes, ONB occurs earlier. For a given heat flux, for smaller mass fluxes, the wall superheat is lower since the vapour generated is greater than that for higher mass fluxes. In the single phase region, since flow is developing, the trend can be contradictory, since for higher mass flux, the boundary layer is thinner leading to better heat transfer compared to that for lower mass fluxes.

The general trend is also not seen in Figure 5.5(c). For mass flux of $200 \text{ kg}/(\text{m}^2\text{s})$, for somewhat larger heat fluxes, the wall superheat is greater compared to that for mass flux of $400 \text{ kg}/(\text{m}^2\text{s})$. This is due to larger mean fluid temperature for the former, since it is sub-cooled boiling. The same is true

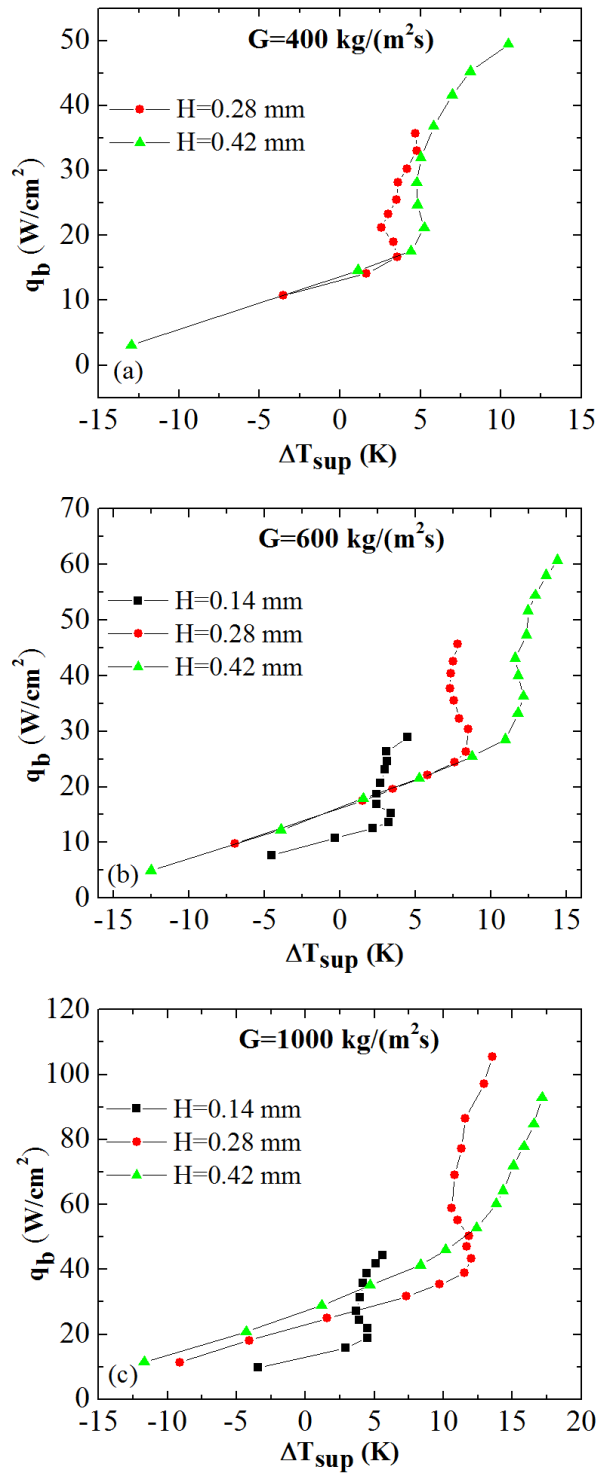


FIGURE 5.4: Effect of microchannel height on the boiling curves for various mass fluxes

for mass flux of $600 \text{ kg}/(\text{m}^2\text{s})$ having a higher wall superheat compared to that of $1000 \text{ kg}/(\text{m}^2\text{s})$. The trends observed in Figures 5.5 and 5.4 are similar to that of Alam et al. [12].

5.2.2 Time-averaged Heat Transfer Coefficient Characteristics

Figure 5.6 shows the effect of microchannel height on heat transfer coefficient as a function of heat flux for various mass fluxes. ONB is characterized by change in slope of the curve. After ONB, the heat transfer coefficient increases substantially with heat flux. In some cases, at much greater heat fluxes, heat transfer coefficient decreases slightly or almost remains constant since enhancement in heat transfer coefficient due to larger vapour quality is compensated by more frequent and longer periods of dry-outs during which heat transfer is poor.

Heat transfer coefficient for smaller heights is greater due to greater confinement effects and larger quantity of vapour generated for a given heat flux. This is further elaborated while presenting transient heat transfer characteristics.

Figure 5.7 shows the effect of mass flux on heat transfer coefficient as a function of heat flux for various microchannel height. After ONB, the heat transfer coefficient is consistently seen to be sensitive to mass flux. For smaller mass fluxes, heat transfer coefficient was always higher since for a given value of heat flux, the amount of vapour generated is greater compared to that for larger mass fluxes.

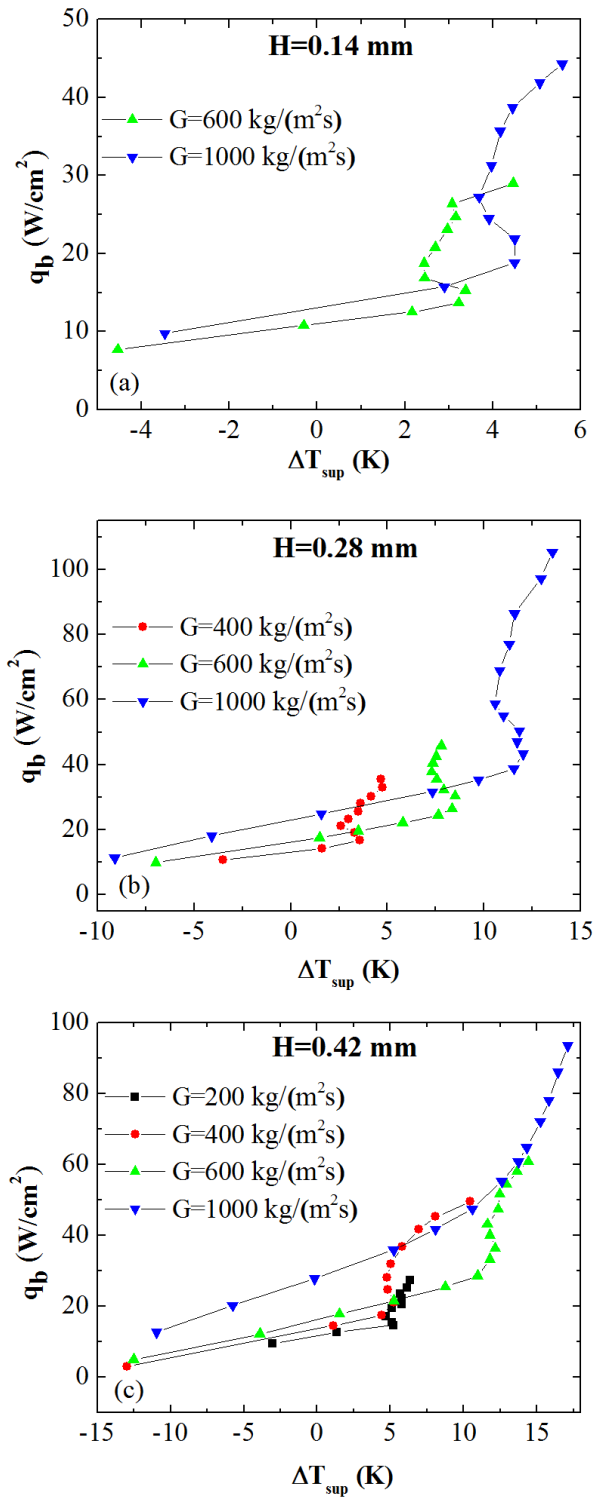


FIGURE 5.5: Effect of mass flux on the boiling curves for various microchannel heights

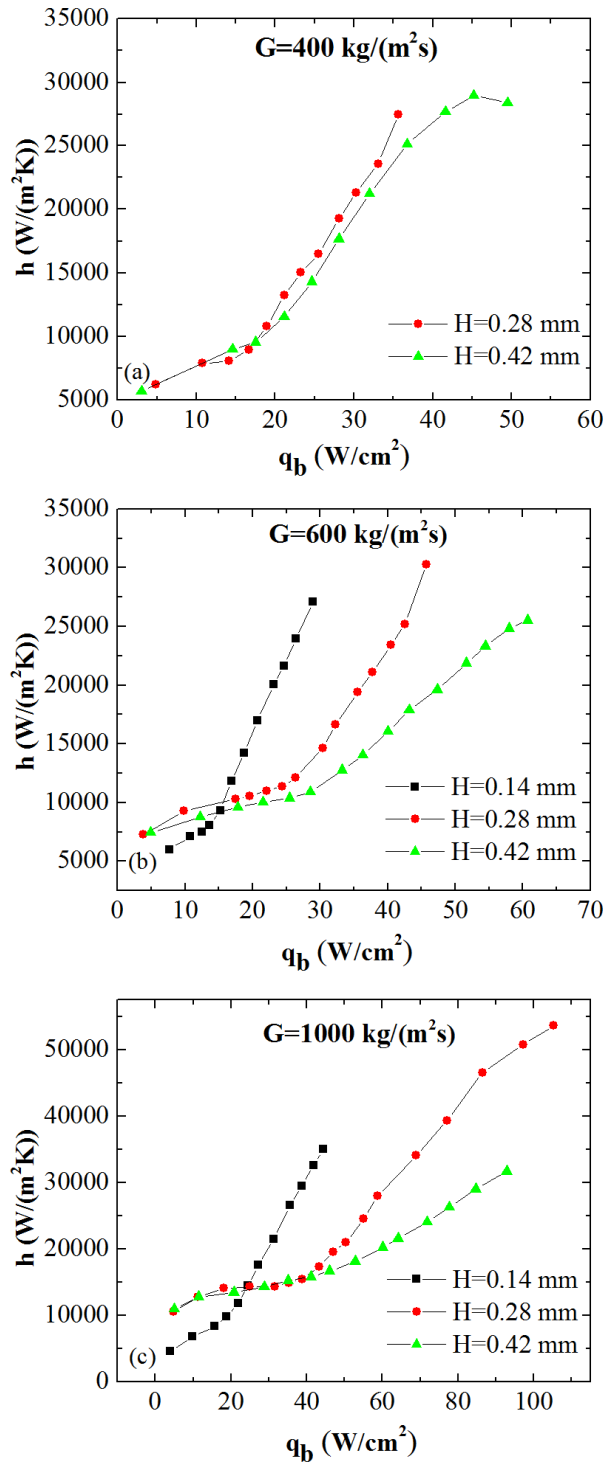


FIGURE 5.6: Effect of microchannel height on heat transfer coefficient as a function of heat flux for various mass fluxes

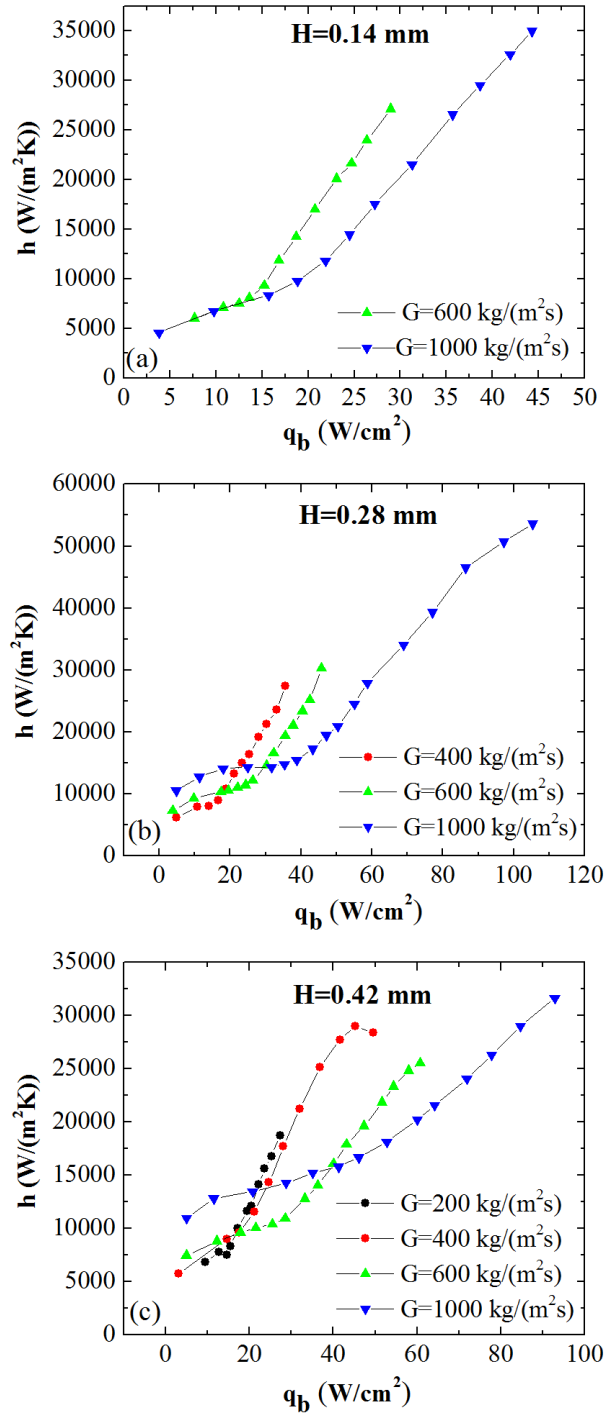


FIGURE 5.7: Effect of mass flux on heat transfer coefficient as a function of heat flux for various microchannel height

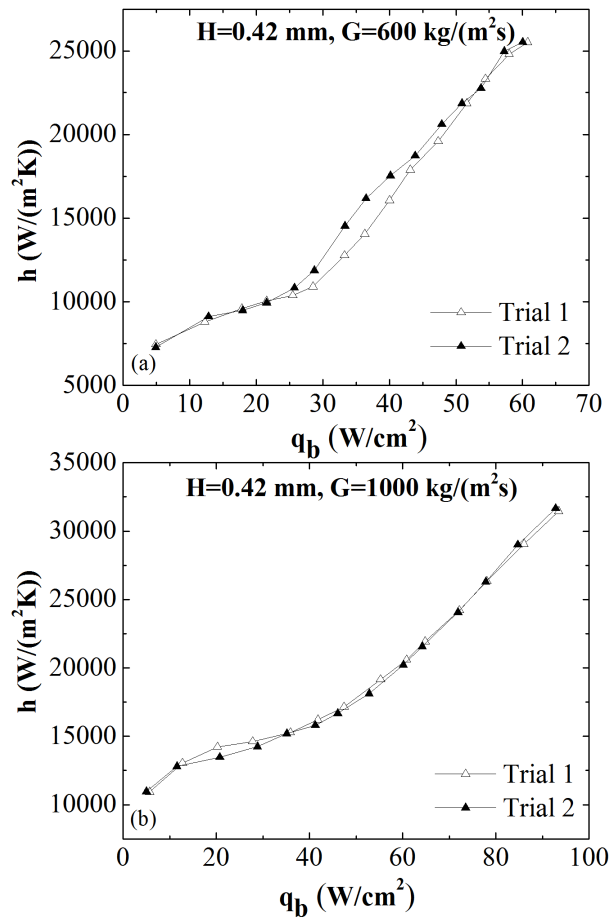


FIGURE 5.8: Heat transfer coefficient as a function of heat flux for two separate trials for two cases

Repeatability experiments were performed for all channel heights and mass fluxes. As can be seen from Figure 5.8, the experimental results had good repeatability.

5.2.3 Transient Heat Transfer Characteristics

Estimation of all transient variables shown in figures of this Sub-section are based on the methodology discussed in Section 4.2. Figures 5.9(a) and (b) and 5.11(a) and (b) show the heat transfer coefficient, wall (wetted surface) heat flux and temperature as a function of time for two base heat fluxes for each of

them. The experimental data along with video is recorded for a period of one second. However, because of lack of knowledge of initial condition (temperature distribution) within the solid domain (between the wetted surface and the sensor), the temperature throughout the domain is assumed to be uniform, equal to the temperature reading of the sensor at initial time 0, in the numerical model discussed in section 4.2. Due to this, the values for the first few milliseconds are erroneous and must be discarded. But since the time axis is shifted, for all subsequent Figures, the time axis begins from 0. Moreover, the IHCP solution algorithm requires information regarding future time steps. Hence, several milliseconds of data just before 1 second is discarded and thus time axis ends at 0.95 seconds.

It is clearly visible from Figures 5.9 and 5.11 that the trends in wall heat flux follow that of heat transfer coefficient. In contrast, the wall temperature falls quickly as the heat transfer coefficient increases sharply. When the heat transfer coefficient value is small, initially, the wall temperature increases quickly and then increases relatively slowly as it approaches the steady state value of temperature corresponding to that (low) value of heat transfer coefficient.

It is interesting to note that the constant wetted surface heat flux boundary condition is not valid. Because of synchronized flow visualization with data capture, it was possible to note that in general, nucleation of a bubble/slug happens when the wall temperature is relatively high. When the slug passes over, due to thin film evaporation, the heat transfer coefficient shoots up, leading to lowering of wall temperature. This often leads to flow of liquid only, during which

time the wall temperature generally starts rising again leading to nucleation of a bubble and the cycle continues. However, nucleation of bubble being a highly stochastic phenomenon, the trends in heat transfer variables in the Figures 5.9 and 5.11 seems haphazard since time intervals between consecutive slugs is not fixed due to nucleation sites being distributed near the sensor location as well as further upstream.

It is worth mentioning that the rate at which the temperature rises/falls corresponding to liquid/slug flow, also depends on thermal mass of the solid substrate. The rate of rise/fall of temperature would be high if thermal mass of the solid substrate were low. Hence the time it takes for the wall temperature to rise/fall in this manner depends not only on the boiling phenomena but also on the material properties of the substrate material and heater depth. Any change in thermal mass may change the flow boiling behavior. For instance, a very small heater depth could have led to very quick rise/fall in temperature thus possibly leading to slugs at a much greater frequency resulting in higher average heat transfer coefficient. Due to this kind of coupling between wall temperature and flow boiling phenomena leading to variations in heat transfer, the heater depth as well as substrate properties could be important for numerical and semi-analytical modeling of heat transfer during flow boiling in microchannels. This kind of study is beyond the scope of this thesis and is suggested as future work.

It can also be seen from Figures 5.9 and 5.11 that for higher base heat fluxes (sub-figure (b) for both cases), the amplitudes of the peaks in heat transfer coefficient are greater compared to lower base heat fluxes (sub-figure (a) for both

cases). Although, there are large variations in the amplitude of peak values of heat transfer coefficient for a given condition (of H , G and q_b), some of the highest of the peaks are clearly greater for higher heat flux. Even the frequency of peaks is much greater for higher heat fluxes for both figures, since higher heat fluxes imply faster rate of rise in wetted surface temperature leading to higher rate of nucleation. For Figure 5.9, at times when heat transfer coefficient is low and flat, some bubbles were observed as can be seen from Figure 5.10(a) (the blue dot indicates the sensor location), while at higher heat flux the bubble density was greater (Figure 5.10(b)) due to higher wall temperature. Hence for higher heat flux case, at times when the heat transfer coefficient is low, its value is higher than those encountered for lower heat flux case. Hence, average heat transfer coefficient for higher heat flux was higher as indicated by dashed lines in the figures.

However, it can be observed from Figure 5.11(a), that some of the peak heights are lower for higher heat flux. The reason is that while nucleation sites were generally closer to the sensor, for low heat flux (as shown in Figure 5.12(a1)), the slugs used to come from further upstream for high heat flux (as shown in Figure 5.12(b1)). Another observation is that valleys are higher and narrower for higher heat flux of 32 W/cm^2 since as seen in Figure 5.12(b2), liquid slugs were very short, while for lower heat flux of 24.6 W/cm^2 , liquid slugs were long (Figure 5.12(a2)).

For microchannel of height 0.42 mm , for almost the same heat flux of approximately 25 W/cm^2 , Figures 5.9(b) and 5.11(a) may be compared which

are for mass fluxes of 200 and 400 $kg/(m^2s)$ respectively. The peaks in heat transfer coefficient for lower mass flux are much greater than those for higher mass flux. This is the reason for higher average heat transfer coefficient for lower mass flux for a given heat flux and given microchannel dimensions.

At low heat flux and mass flux condition of Figure 5.9(a), the fluctuations seem to be cyclic while the same for high heat flux and mass flux of Figure 5.11(b) do not seem to be cyclical. This is because, at higher heat flux, generally the number of active nucleation sites are more. This leads to more number of slugs resulting in more number of peaks in Figure 5.11(b) compared to Figure 5.9(a). Since the peak value of heat transfer coefficient depends on location of slug incipience as well as whether a downstream slug is present or not (as would be seen in the discussion of the subsequent figures in this section), the trends in heat transfer coefficient may not follow a regular pattern due to the stochastic nature of boiling.

To gain more detailed insights into the variation of heat transfer coefficient and its correlation with boiling phenomena (captured in video frames), three time-intervals of interest in Figure 5.9(a) have been chosen and heat transfer coefficient verses time curve has been replotted in Figures 5.13, 5.16 and 5.18. The corresponding video frames for each of these plots have been shown respectively in Figures 5.14, 5.17 and 5.19.

The horizontal dashed line on heat transfer coefficient verses time curve indicate the time-averaged value. The vertical dashed lines have been labeled and

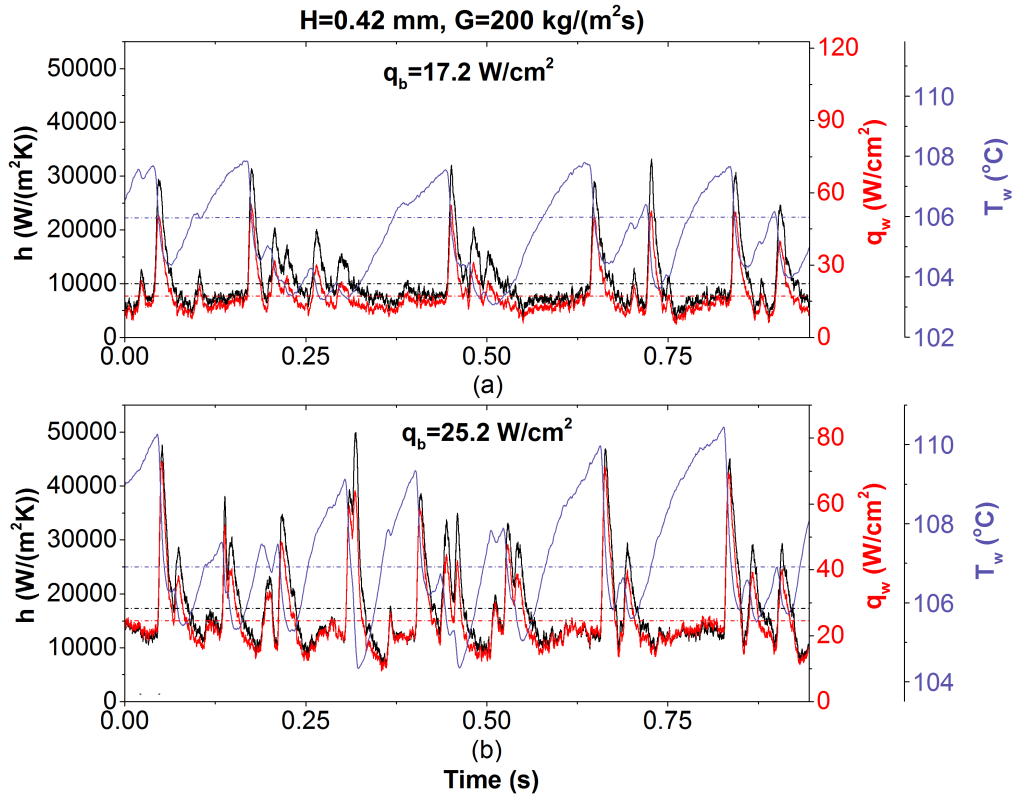


FIGURE 5.9: Variation of heat transfer coefficient, wall (wetted surface) heat flux and wall (wetted surface) temperature with time for $H = 0.42 \text{ mm}$, $G = 200 \text{ kg}/(\text{m}^2 \text{ s})$ for (a) $q_b = 17.2 \text{ W}/\text{cm}^2$ (b) $q_b = 25.2 \text{ W}/\text{cm}^2$

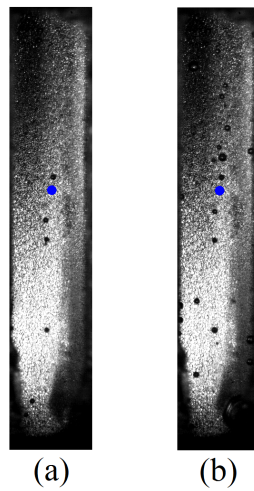


FIGURE 5.10: Bubbly flow at times when heat transfer coefficient is low in Figure 5.9 at heat fluxes (a) $q_b = 17.2 \text{ W}/\text{cm}^2$ (b) $q_b = 25.2 \text{ W}/\text{cm}^2$

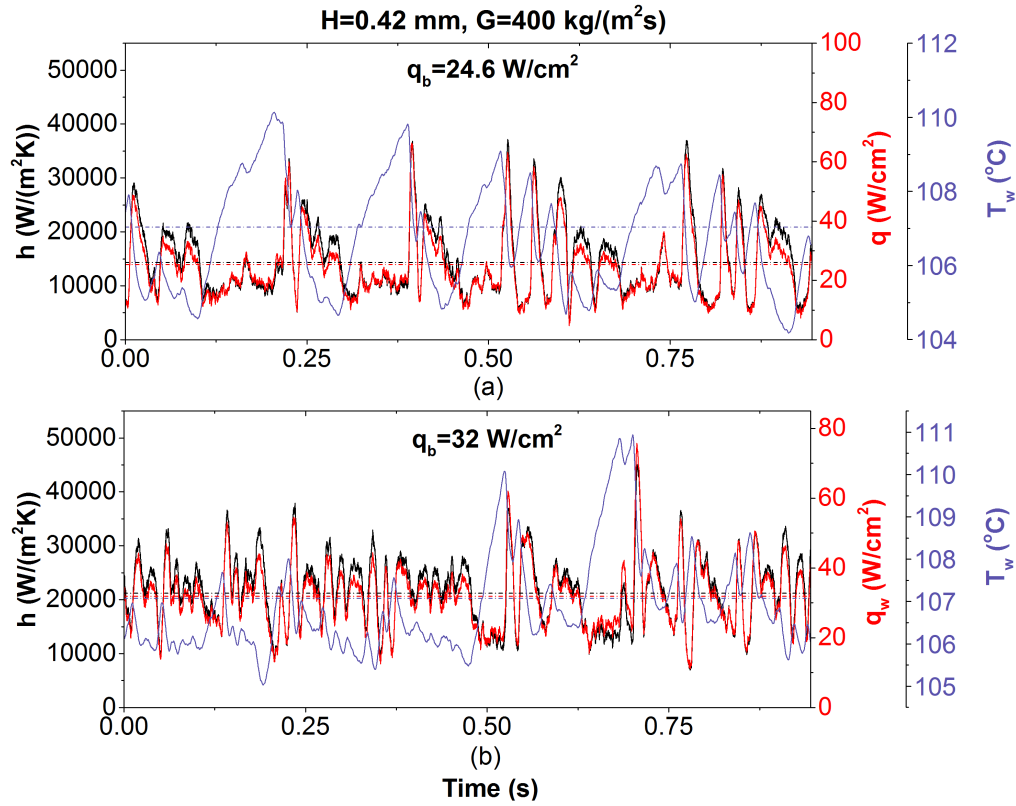


FIGURE 5.11: Variation of heat transfer coefficient, wall (wetted surface) heat flux and wall (wetted surface) temperature with time for $H = 0.42 \text{ mm}$, $G = 400 \text{ kg}/(\text{m}^2\text{s})$ for (a) $q_b = 24.6 \text{ W}/\text{cm}^2$ (b) $q_b = 32 \text{ W}/\text{cm}^2$

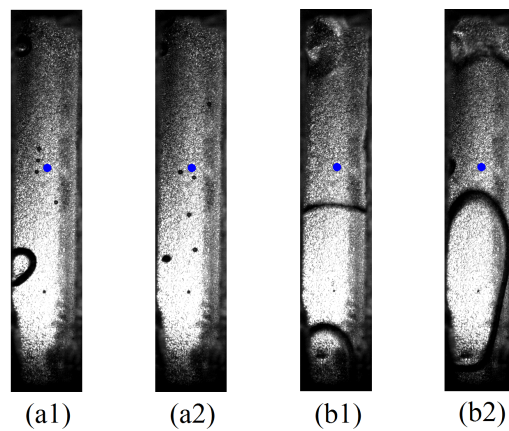


FIGURE 5.12: Time frames corresponding to Figure 5.11 for (a1) $q_b = 24.6 \text{ W}/\text{cm}^2$, nucleation site is close to sensor location (a2) $q_b = 24.6 \text{ W}/\text{cm}^2$, long liquid slug (b1) $q_b = 32 \text{ W}/\text{cm}^2$, nucleation site is further upstream outside the field of view of the camera (b2) $q_b = 32 \text{ W}/\text{cm}^2$, short liquid slug

the corresponding event has been described in the "Legend". The figures following each of the plots show video-frames labeled in a similar manner showing the flow-boiling phenomena corresponding to labeled time-instants in the heat transfer coefficient verses time plots. The blue dot in each of the video frames indicates the location of the centroid of temperature sensor.

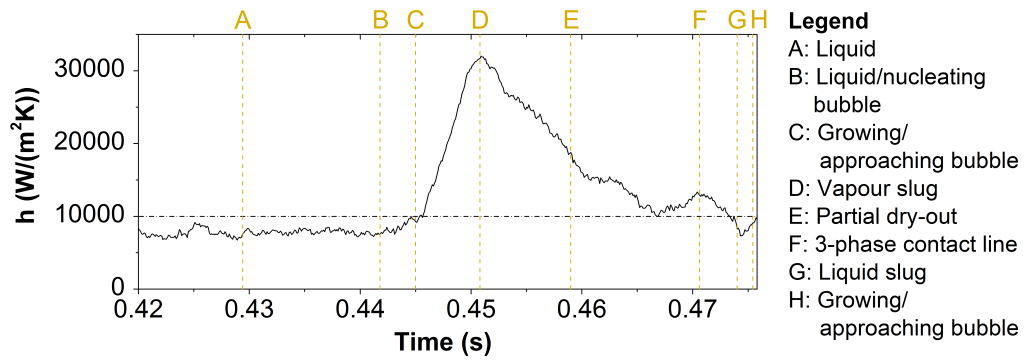


FIGURE 5.13: Variation of heat transfer coefficient with time for $H = 0.42 \text{ mm}$, $G = 200 \text{ kg}/(\text{m}^2\text{s})$, $q_b = 17.2 \text{ W}/\text{cm}^2$ from 0.42-0.476 seconds

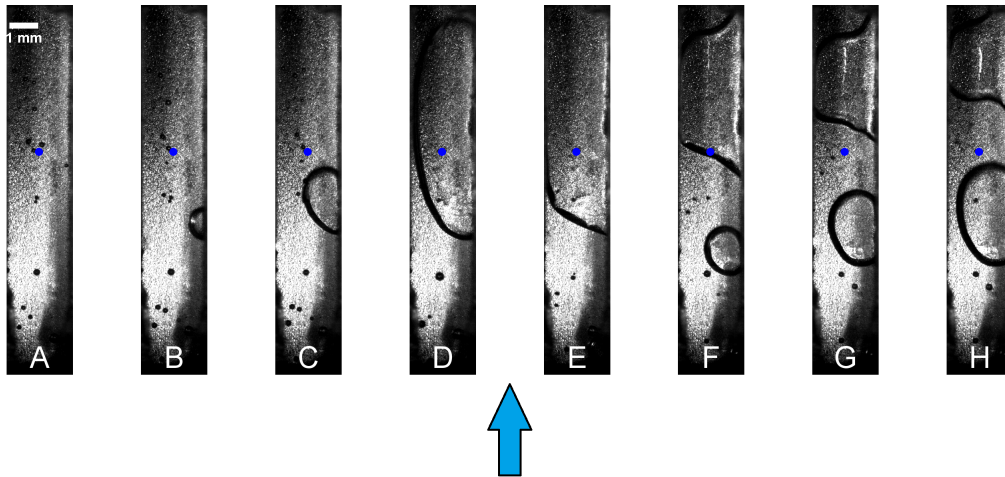


FIGURE 5.14: Video frames corresponding to Figure 5.13

For a bubble travelling at a mean velocity of single phase flow, it would take ≈ 0.1 second to traverse the length of the microchannel at a mass flux of $200 \text{ kg}/(\text{m}^2\text{s})$. Hence, for time interval greater than 0.1 second, if no slug is

seen in flow visualization, the flow is labeled as liquid flow and is distinguished herein from liquid slug flow.

In Figure 5.13, time instant A indicates flow of liquid only as is shown in video frame A of Figure 5.14. Several small bubbles were seen during flow of liquid. The heat transfer coefficient is relatively low and the curve is almost flat during liquid flow. Frame B shows the incipience of a bubble at a nucleation site close to the sensor. At time instant C, the bubble nose is close to the sensor and is approaching it leading to a slight increase in heat transfer coefficient. This could be due to evaporation of liquid near the nose (front interface) of the bubble and quenching of surrounding liquid as well as due to flow structures at the bubble nose that promote mixing as suggested by Rao and Peles [84]. From time instant C to D, the slug grows and traps a thin film of liquid over the wetted surface. Schematic of slug flow is shown in Figure 5.15.

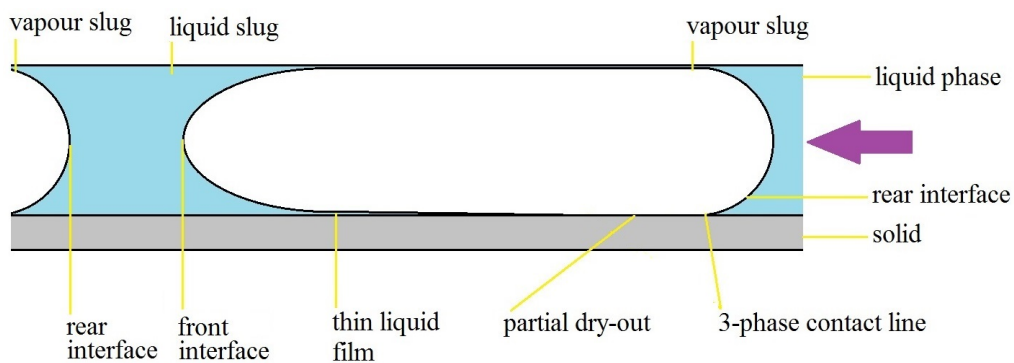


FIGURE 5.15: Schematic of slug flow

The film evaporates with time and with thinning down of the film, the heat transfer coefficient increases and reaches a maximum at time instant D. The inverse relationship of heat transfer coefficient and thin film thickness may be

understood by Equation 5.1 suggested by Thome et al. [15] for steady conduction through the thin film of liquid.

$$h = \frac{k_l}{\delta} \quad (5.1)$$

After time-instant D, the thin film was seen to break and accumulate leading to partial dry-out (as can be seen in frame E) due to which the wetted surface is progressively exposed to more and more vapour. The liquid film does not thin down uniformly throughout and so dry-out does not appear simultaneously throughout. Hence, the heat transfer coefficient decreases gradually rather than dropping sharply

The mechanism of partial dry-out was observed to be due to accumulation of liquid at a location due to cohesive force by virtue of which the liquid tries to maintain a certain contact angle with the wetted surface. Hence, very high peaks in heat transfer coefficient predicted by Equation 5.1 for infinitesimally thin film of liquid, are not observed. The average surface roughness was $Ra = 0.6$ microns and hence for the case of perfectly hydrophilic surface, the potentially minimum thin film thickness would be $O(10^{-6})$ meters corresponding to which the maximum heat transfer coefficient would be $O(10^6) W/(m^2K)$ for water.

At time-instant F, the rear interface of the vapour slug passes over the sensor and a small peak is observed in Figure 5.13. This is because of 3-phase contact line evaporation mechanism. During passage of a liquid slug (time-instant and frame G) having a short length, it was observed that the rear interface of

the downstream slug, moving with a velocity of 0.38 m/s almost stagnated the liquid since the bubble tries to expand both, upstream and downstream. Hence, heat transfer coefficient was low. As another slug approaches in frame H, the heat transfer coefficient again starts increasing.

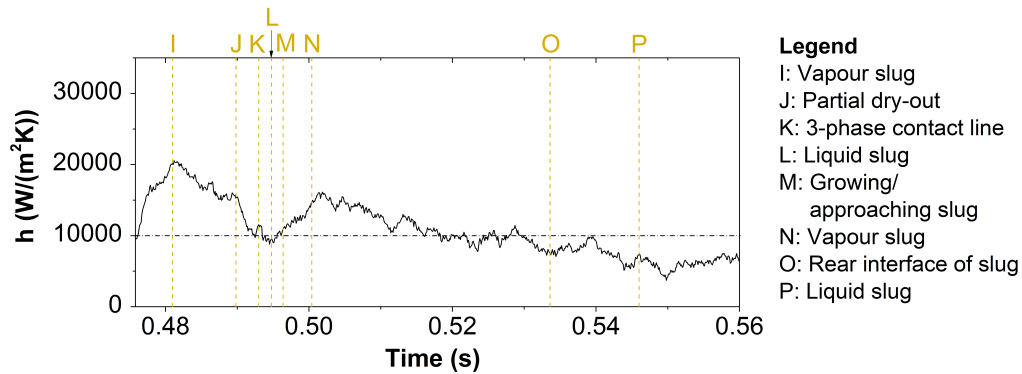


FIGURE 5.16: Variation of heat transfer coefficient with time for $H = 0.42 \text{ mm}$, $G = 200 \text{ kg}/(\text{m}^2\text{s})$, $q_b = 17.2 \text{ W}/\text{cm}^2$ from 0.476-0.56 seconds

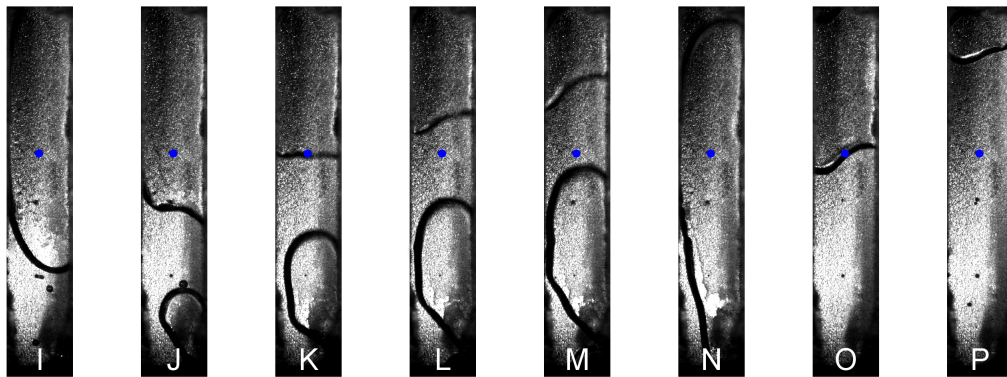


FIGURE 5.17: Video frames corresponding to Figure 5.16

Figures 5.16 and 5.17 respectively show the immediately following time-interval of interest. Similar trend in heat transfer coefficient with sequence of boiling event follows. At time-instants (and corresponding frames in Figure 5.17) I,J,K and L, vapour slug (thin film evaporation), partial dry-out, 3-phase contact line and a short liquid slug were observed over the sensor location. It can be clearly observed that the peak heat transfer coefficient ($20,568 \text{ W}/(\text{m}^2\text{K})$)

at time-instant I is significantly lower than that at D (Figure 5.13) at which it is $32,043 W/(m^2K)$.

The difference is due to the difference in the initial thickness of the liquid film trapped between the slug and the heated/wetted surface. Zhang et al.[85] have explained that hydrodynamic boundary layer plays a role in determining the thickness for which the low velocity liquid near the wall offers resistance to the in-coming bubble/slug front. For frame D, it was observed that the nucleation site was near to the sensor. Moreover, there was no hindrance to the fluid-flow since there was no vapour slug in the downstream region. Hence the boundary layer just starts developing and its thickness is very small at the sensor location. So a very thin layer of liquid offered resistance to the bubble motion. Hence, a very thin liquid film was trapped by the incoming slug which later lead to a high heat transfer coefficient as can be understood from Equation 5.1. For the slug in Frame I, although the nucleation was quite near to the sensor location too (See trailing bubble in frame F in Figure 5.14), the presence of another slug just downstream, moving with a velocity of $0.38 m/s$ stagnated the liquid slug between them. When the velocity of the fluid is small, the boundary layer develops quickly, hence the boundary layer is thicker, implying a thicker layer of liquid resisting the in-coming slug. Hence, the peak heat transfer coefficient seen at time-instant I is smaller than that at time-instant D. It may be again be noted that before the thin film of liquid could become thinner, the cohesive forces in the liquid tends to accumulate the liquid film causing partial dry-out so that peaks in heat transfer coefficient are low.

A very small peak was observed at K during the passage of 3-phase contact line (See Figure 5.17). The peak value ($11,570 \text{ W}/(\text{m}^2\text{K})$) is smaller compared to that observed at F (Figure 5.13). The differences are due to the fact that 3-phase contact line is not always well established since partial rather than complete dry-outs were observed leading to differences in length of 3-phase contact lines over the sensor location.

Following this, a short liquid slug is again observed at time-instant L. Since the downstream slug causes flow-stagnation, again the expected improvement in heat transfer coefficient is not seen. Again, the same sequence of events follows. At time-instants M,N,O and P, approaching/growing slug, vapour slug, rear interface of the slug and liquid slug are respectively observed. During this cycle, the peak heat transfer coefficient at N, due to thin film evaporation is even lower ($15,747 \text{ W}/(\text{m}^2\text{K})$). This is due to larger thickness of boundary layer due to both, bubble incipience further upstream (See small bubble in bottom right of frame I which later grows in frame J) as well as flow stagnation due to downstream slug moving with a velocity of 0.19 m/s . Another difference observed was that even though it seems that 3-phase contact line passes over the sensor location, since there was still liquid in the thin film near the rear vapour-liquid interface, 3-phase contact line was not well established and a small peak observed before was not seen at time-instant O.

As can be seen in Figures 5.18 and 5.19, the same cycle repeats. A small bubble seen in Frame Q (at the lower right hand corner of the frame in Figure 5.19) grows to become a slug in frames R and S. The nucleation site is relatively

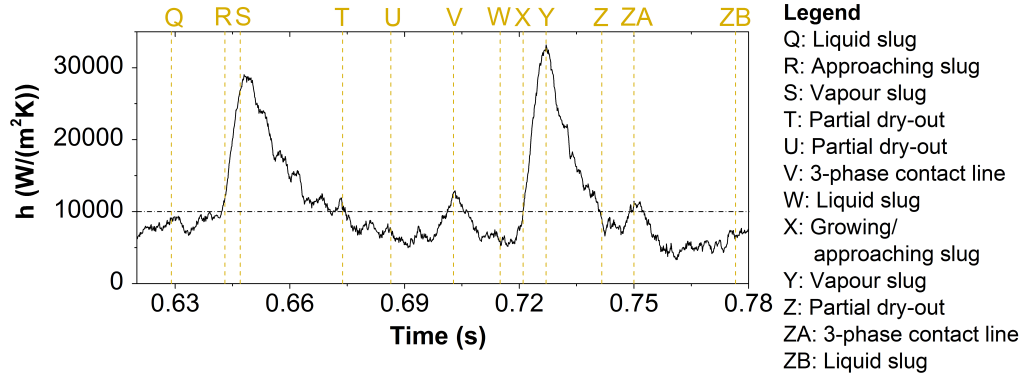


FIGURE 5.18: Variation of heat transfer coefficient with time for $H = 0.42 \text{ mm}$, $G = 200 \text{ kg}/(\text{m}^2\text{s})$, $q_b = 17.2 \text{ W}/\text{cm}^2$ from 0.62-0.78 seconds

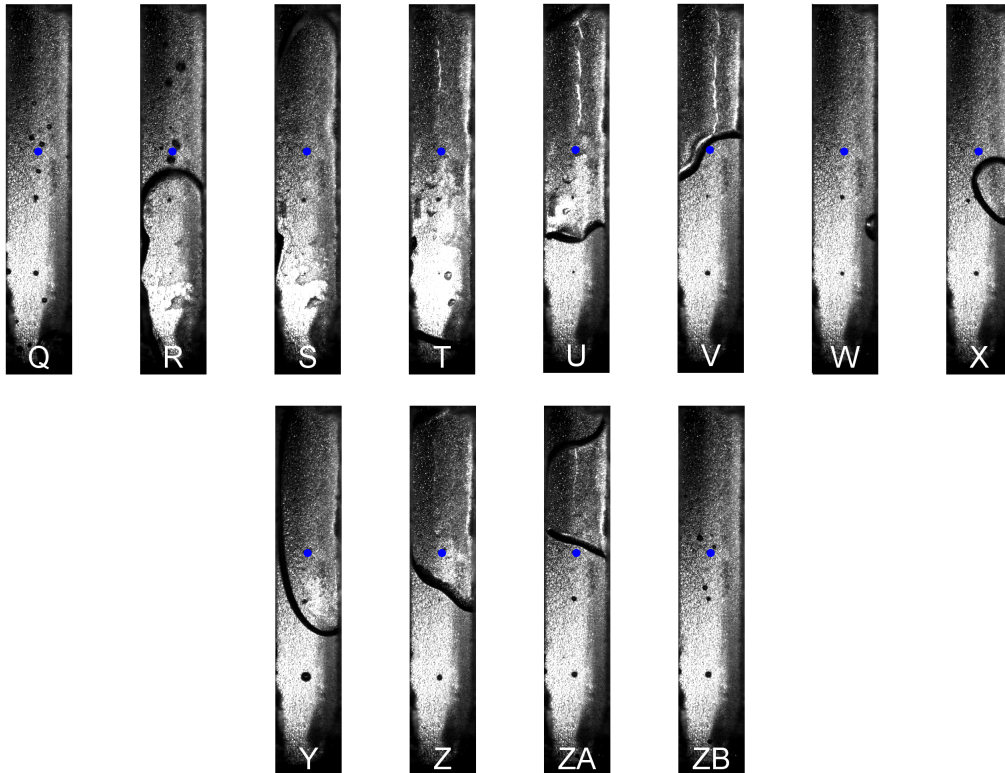


FIGURE 5.19: Video frames corresponding to Figure 5.18

upstream compared to that at frame B. Hence the boundary layer thickness is greater for slug in this case compared to that in frame D. Thus heat transfer coefficient for time-instant S is slightly lower $29,049 \text{ W}/(\text{m}^2\text{K})$ compared to that at time-instant D (Figure 5.13). However, the peak is still larger at S compared to I and N (Figure 5.16) since there was no downstream vapour slug to cause flow stagnation and the front interface of the bubble moved with a velocity of 1.46 m/s .

Small bubble in frame W grows to become a larger bubble in frame X and eventually a slug in frame Y. The nucleation site is the same as that in frame B (Figure 5.14). Moreover, in both cases, no downstream vapour slug was observed. Hence, for both cases the peak heat transfer coefficient is very similar, $33,178 \text{ W}/(\text{m}^2\text{K})$ at time instant Y and $32,043 \text{ W}/(\text{m}^2\text{K})$ at time instant D.

For frames V and ZA in Figure 5.19, due to a relatively well stabilized 3-phase contact line, small peaks are observed at time-instants V and ZA in Figure 5.18

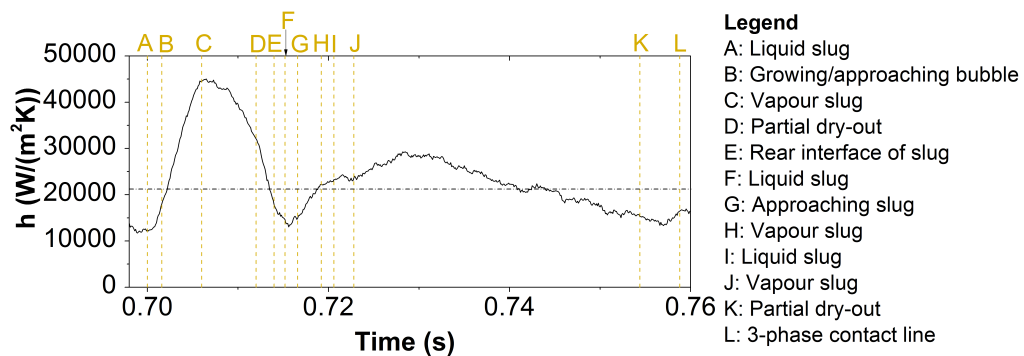


FIGURE 5.20: Variation of heat transfer coefficient with time for $H = 0.42 \text{ mm}$, $G = 400 \text{ kg}/(\text{m}^2\text{s})$, $q_b = 32 \text{ W}/\text{cm}^2$

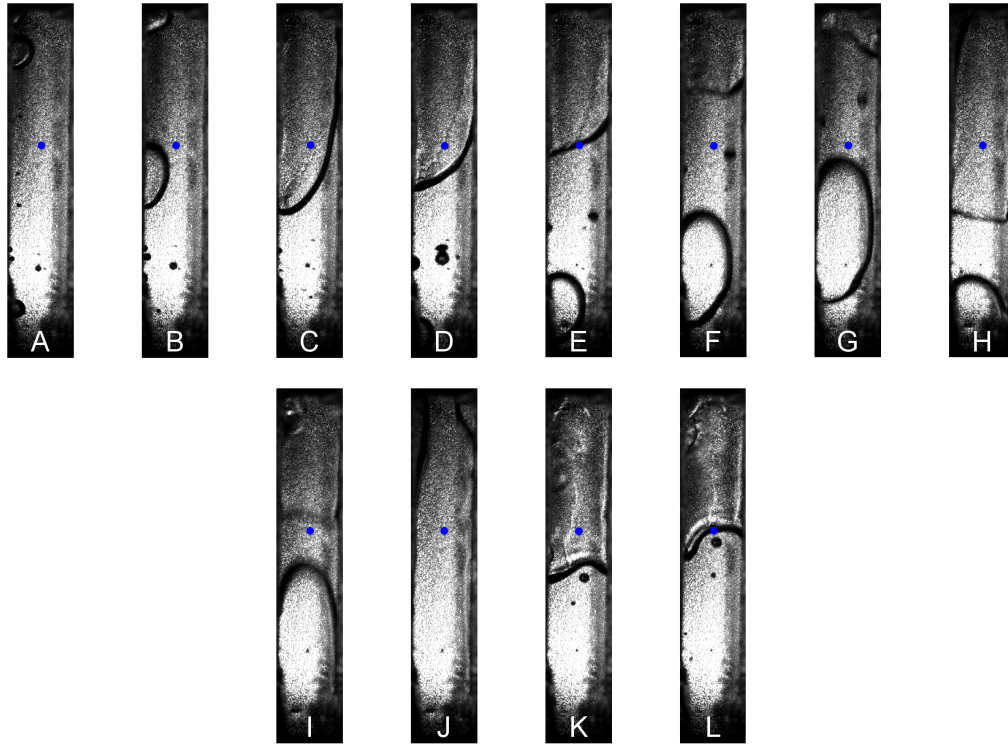


FIGURE 5.21: Video frames corresponding to Figure 5.20

Figure 5.20 shows transient variations in heat transfer coefficient in a certain time-interval of interest. The video file from which these frames were extracted has been uploaded in the attached CD for reference. The condition is same as that of Figure 5.11(b). The sequence of events repeat for this condition too. For this condition however, the peak heat transfer coefficient at time-instant C is significantly larger compared to all previously discussed cases. This is because of several reasons. The nucleation site is very close to the sensor (See frame B), there is no downstream slug to restrict to cause flow stagnation. Additionally, the higher heat flux (32 W/cm^2) implies faster thinning down of the thin film liquid layer so that heat transfer coefficient reaches a higher peak before the thin film liquid layer gets enough time to accumulate at a location to cause partial dry-out and the consequent lowering of heat transfer coefficient.

Subsequently, due to partial dry-out as shown in frame D, the heat transfer coefficient drops. The 3-phase contact line is not well established at time-instant E and so small peak is not observed. Since flow was stagnated by downstream bubble (whose rear interface moved with a velocity of 0.52 m/s) during the passage of liquid slug at time instant F, heat transfer coefficient is low. Subsequently, during the passage of slug in frame H, due to previously stagnated liquid, the boundary layer thickness being larger and nucleation site being upstream, the heat transfer coefficient is low. However, during the passage of very short liquid slug in frame I, the heat transfer coefficient is relatively much higher compared to similar events discussed previously. Although there was a vapour slug just downstream, the upstream bubble was observed to grow somewhat rapidly and accelerate. Hence, there was no stagnation and velocity of the liquid slug was quite large (2.7 m/s) leading to high heat transfer coefficient at time instant I (liquid slug). In fact, due to high velocity of slug, the rear interface of downstream slug in frame I appears blurred. The subsequent peak in heat transfer coefficient is reached during thin film evaporation a little after time-instant J. However, this peak is relatively still lower than that at C since the nucleation was further upstream outside the field of view of the camera.

The peaks observed during thin film evaporation are in accordance with the model proposed by Thome et al. [15] as well as the findings of Rao and Peles [84] and Bigham and Moghaddam [65].

There are however, certain differences in the heat transfer coefficient trends

during passage of liquid slug. In contrast to the conclusions arrived at by Kandlikar [60] and Magnini et al.[38], the heat transfer coefficient for the present experimental conditions was lower than that encountered during thin film evaporation.

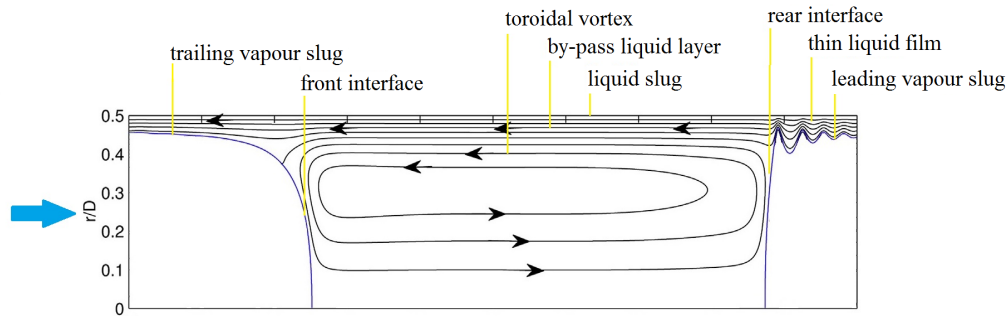


FIGURE 5.22: Streamlines within a liquid slug trapped between vapour slugs, in a reference frame moving with the bubble (Adapted from Magnini et al. [38])

Kandlikar [60], based on analogy of heat transfer in microchannels to that during pool boiling as well as experiments on evaporating meniscus on a moving heated surface [86] opined that the combination of micro-convection and transient conduction are responsible for high heat transfer coefficient during liquid slug flow. Circulation is induced (as shown in Figure 5.22) in the liquid slug and this provides a path for the heat to be transported from superheated liquid layer experiencing transient conduction to liquid-vapour interface of the trailing vapour slug. This in turn helps to reduce temperature behind the front interface within the liquid which leads to high heat transfer rate.

Magnini et al.[38] carried out simulations to investigate the influence of leading and sequential bubbles during slug flow in a microchannel. They concluded that due to a re-circulating toroidal vortex (Figure 5.22) within the liquid

slug trapped between two consecutive vapour slugs, the by-pass liquid layer refreshes with cooler fluid and hence the heat transfer coefficient was much higher than that which is otherwise expected in liquid slug region. For the conditions of their simulations (short bubble length and low heat flux), this heat transfer coefficient was comparable to thin liquid film region during vapour bubble flow. In the figure, ripples at the interface can also be observed at the rear end of the leading vapour slug. These are capillary waves whose dynamics are in general influenced by surface tension, gravity and fluid inertia. In the present work however, these capillary waves were not observed.

Unlike the case considered by Magnini et al. [38], in the current case flow stagnation was sometimes observed in the liquid behind the rear vapour slug interface due to bubble growth towards the upstream which may happen due to upstream compressibility. The resulting difference in the heat transfer trend can be explained based on the work by Thulasidas et al. [87]. Using Particle Imaging Velocimetry (PIV), they studied toroidal vortices in liquid slugs trapped between strings of bubbles in circular and square capillaries, for various capillary numbers for 2 phase flows without phase change. Recirculation time was pointed out to be an important measure of radial mixing which is responsible for good heat transfer performance. For small capillary numbers, the dimensionless recirculation time was found to be almost constant (≈ 3). This means that the time taken by a typical particle inside the liquid slug to move from one end to the other end of the slug is equal to the time taken by the slug to move 3 times its length.

Hence, assuming the applicability of these results to flow boiling in microchannels with rectangular cross-section, it can be concluded that longer is the liquid slug length and smaller is the bubble velocity, the longer would be the time the particle would take to circulate within the liquid slug and slower would be the rate at which the fluid near the wall would be replenished with cooler fluid resulting in lesser enhancement in heat transfer. As mentioned before, somewhat high heat transfer coefficient was observed when the liquid slug was short and its velocity was high. However, if the liquid slug was long and/or velocity was low (due to stagnation), the heat transfer coefficient was low.

Another difference between the present case and the cases considered by Kandlikar [60] and Magnini et al. [38] is that the current case is that of sub-cooled boiling. The recirculation may not enhance heat transfer performance as much as it is expected to, for the case of saturated flow boiling since the bulk of the fluid is anyways cooler, below saturation temperature. This likely prevented the re-circulating fluid from losing as much amount of thermal energy at the front bubble interface of the vapour bubble (due to phase change) as it would for saturated flow boiling condition.

Effect of Channel Height

From Figure 5.23, it is evident that many of the peaks in heat transfer coefficient are much greater in magnitude for microchannel with height 0.28 mm compared to that for microchannel with height 0.42 mm . This is due to bubble nucleation sites often being closer to the sensor location for smaller channel as

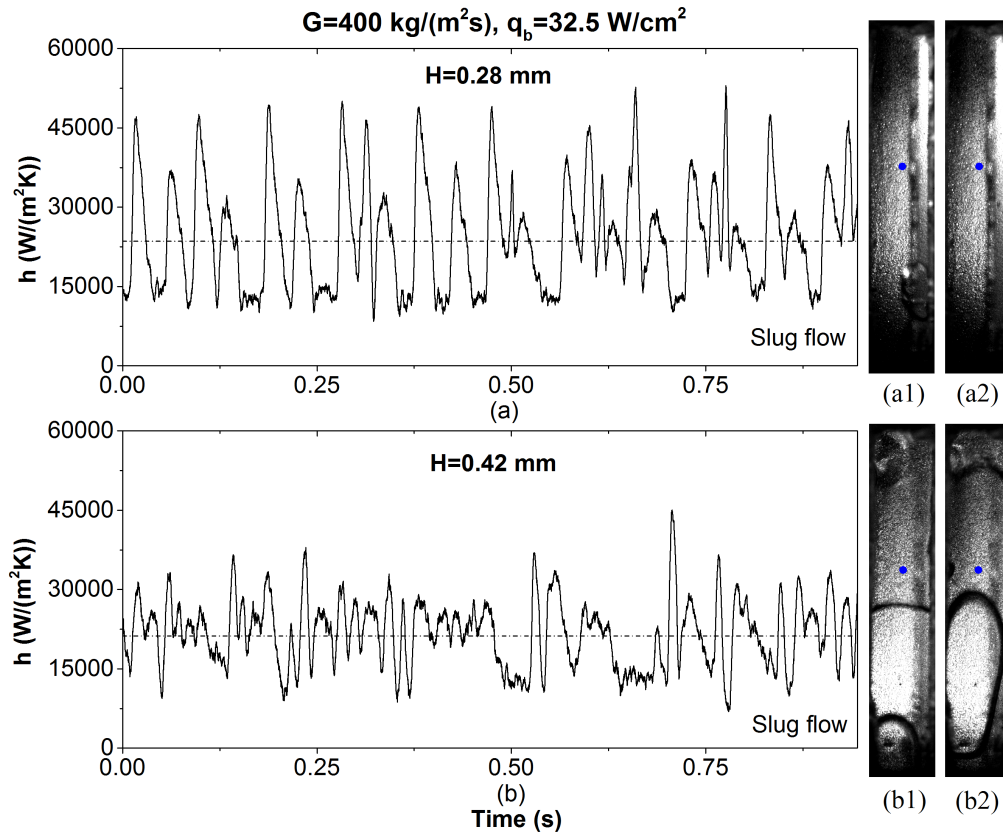


FIGURE 5.23: Variation of heat transfer coefficient with time for $G = 400 \text{ kg}/(\text{m}^2\text{s})$, $q_b = 32.5 \text{ W}/\text{cm}^2 (\pm 1.5\%)$ for microchannel heights of (a) 0.28 mm (b) 0.42 mm . Video frames (a1) Nucleation site is close to sensor location for condition (a) (a2) Liquid slug is long for condition (a) (b1) Nucleation site is upstream outside the field of view of the camera for condition (b) (b2) Liquid slug length is short for condition (b)

seen in frame (a1) (Figure 5.23) compared to upstream location of nucleation sites for larger microchannel as seen in frame (b1). This could be due to larger average (temporally and spatially) wall superheat of $5 \text{ }^\circ\text{C}$ for $H = 0.42 \text{ mm}$ channel compared to $3.9 \text{ }^\circ\text{C}$ for $H = 0.28 \text{ mm}$ channel. The frequency of peaks (caused by thin film evaporation during passage of slugs) was greater for larger microchannel, which again can be due to larger wall superheat (however, as would be seen in subsequent cases, a counter effect can be caused by larger channel heights and/or mass fluxes since such conditions are less conducive for

bubble confinement to happen, thus for many cases, it leads to more small bubbles and lesser confined bubbles/slugs that lead to peaks in heat transfer coefficient).

The valleys too were higher for 0.42 mm channel. This is due to shorter liquid slugs for larger microchannel. Frame (a2) (for $H = 0.28\text{ mm}$) shows that liquid slug is so long that it occupies the complete channel in the field of view of the camera, while frame (b2) (for $H = 0.42\text{ mm}$) shows a short liquid slug. Because of long slugs for microchannel with $H = 0.28\text{ mm}$, the valleys are generally flatter compared to microchannel with $H = 0.42\text{ mm}$.

As can be seen from Figure 5.24, the average heat transfer coefficient for smaller microchannels is much larger. For smallest microchannel ($H = 0.14\text{ mm}$), churn as well as wispy annular flow was observed. The trend in temporal variations in heat transfer coefficient is similar to that during slug flow. When slugs (that may be oddly shaped) passed over the sensor location, the heat transfer coefficient rises and when dry-out commences, it falls. During the passage of liquid slugs, the heat transfer coefficient was low. The peaks and valleys for the smallest microchannel are usually greater than those for larger microchannels. This is due to thinner film of liquid trapped for microchannels with smaller heights as noted by Zhang et al. [85]. Although the nucleation site was quite often close to the sensor location for sub-figure (b) as shown in frame (b1), the effect of smaller height supersedes the effect of closeness of nucleation site so that peaks for sub-figure (a) are greater.

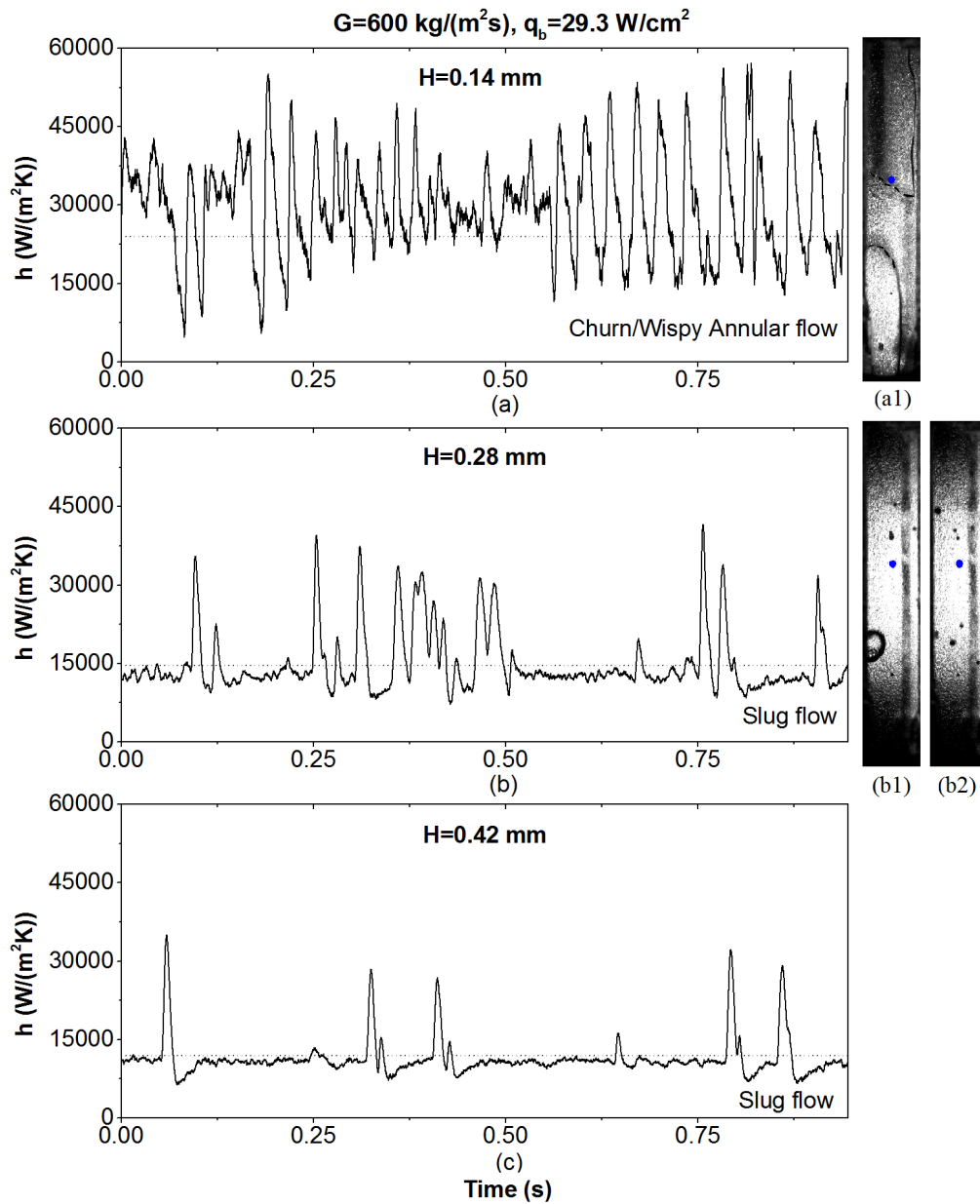


FIGURE 5.24: Variation of heat transfer coefficient with time for $G = 600 \text{ kg}/(\text{m}^2\text{s})$, $q_b = 29.3 \text{ W}/\text{cm}^2 (\pm 3.6\%)$ for microchannel heights (a) 0.14 mm (b) 0.28 mm (c) 0.42 mm. Video frames (a1) Short liquid slug for condition (a) (b1) Nucleation site is near to the sensor for condition (b) (b2) Bubbles observed during passage of long liquid slug for condition (b)

The length of liquid slugs too were shorter for smaller microchannel as can be seen by comparing frames (a1) and (b2). In frame (b2), liquid and few small bubbles completely occupy the microchannel length seen in the field of view of the camera. Hence the valleys for smaller microchannels were often higher. Some of the valleys with very low heat transfer coefficient indicate partial dry-out conditions.

The average (temporally and spatially) wall superheat for $H = 0.14 \text{ mm}$, $H = 0.28 \text{ mm}$ and $H = 0.42 \text{ mm}$ were 4.1, 6 and 6.2 °C. The effect of greater bubble confinement and earlier ONB for smaller channels outweighs the effect of wall superheat in determining the slug frequency.

The trends shown in Figure 5.25 are quite similar to those seen in Figure 5.24. Notable difference is that for microchannel with $H = 0.14 \text{ mm}$, the valleys are often very low. This was due to very frequent partial dry-out conditions arising from relatively greater heat flux.

For microchannel with $H = 0.42 \text{ mm}$, bubbly flow was observed. However, very seldom, large bubbles were seen as shown in frame (c).

Effect of Mass Flux

Figure 5.26 shows the effect of mass flux on transient heat transfer for mass fluxes of 600 $\text{kg}/(\text{m}^2\text{s})$ and 1000 $\text{kg}/(\text{m}^2\text{s})$. The frequency of peaks (slugs) is greater for smaller mass flux since lower mass flux condition is more favourable for confinement.

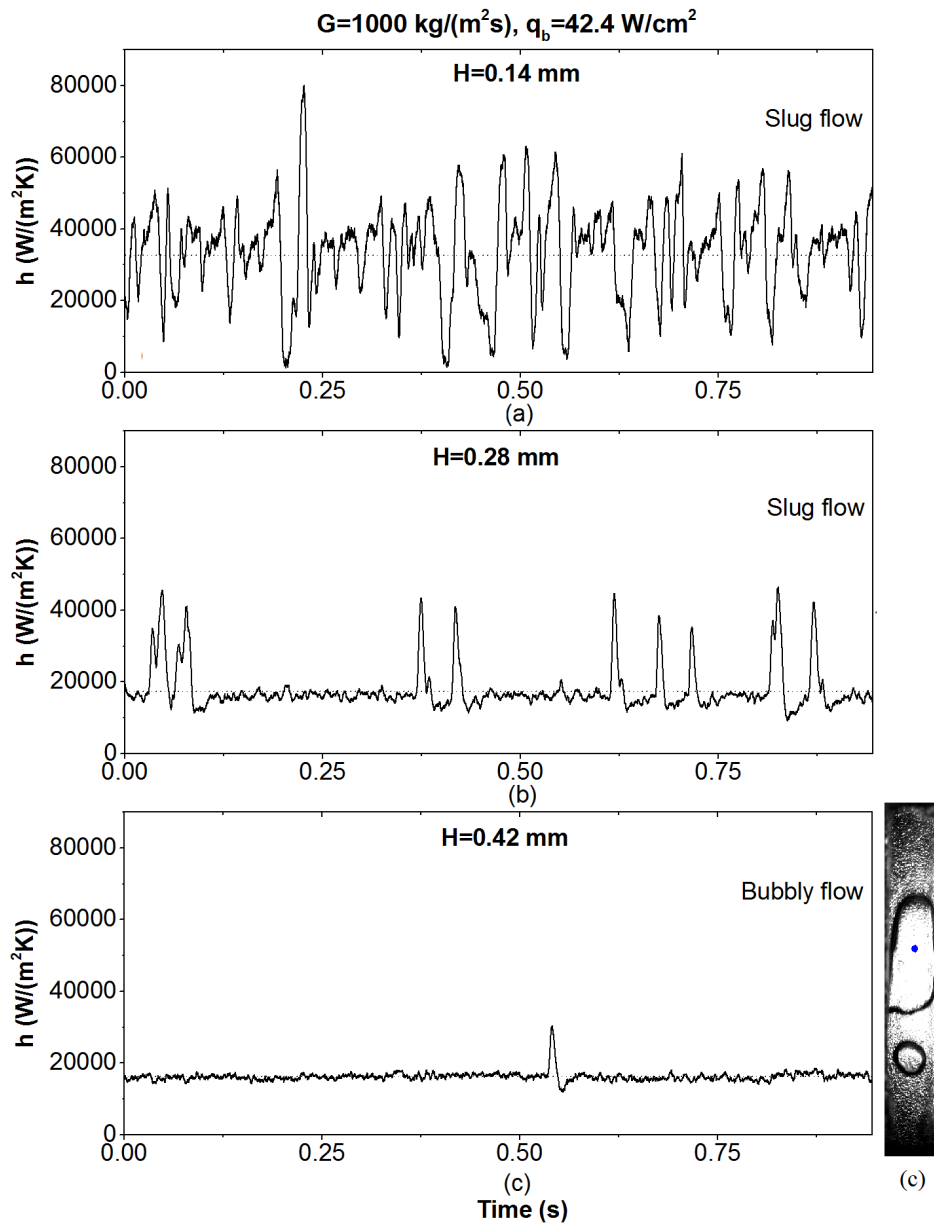


FIGURE 5.25: Variation of heat transfer coefficient with time for $G = 1000 \text{ kg}/(\text{m}^2\text{s}), q_b = 42.4 \text{ W}/\text{cm}^2 (\pm 2.4\%)$ for various microchannel heights (a) 0.14 mm (b) 0.28 mm (c) 0.42 mm. Video frame (c) Very rarely observed short vapour slug for condition (c)

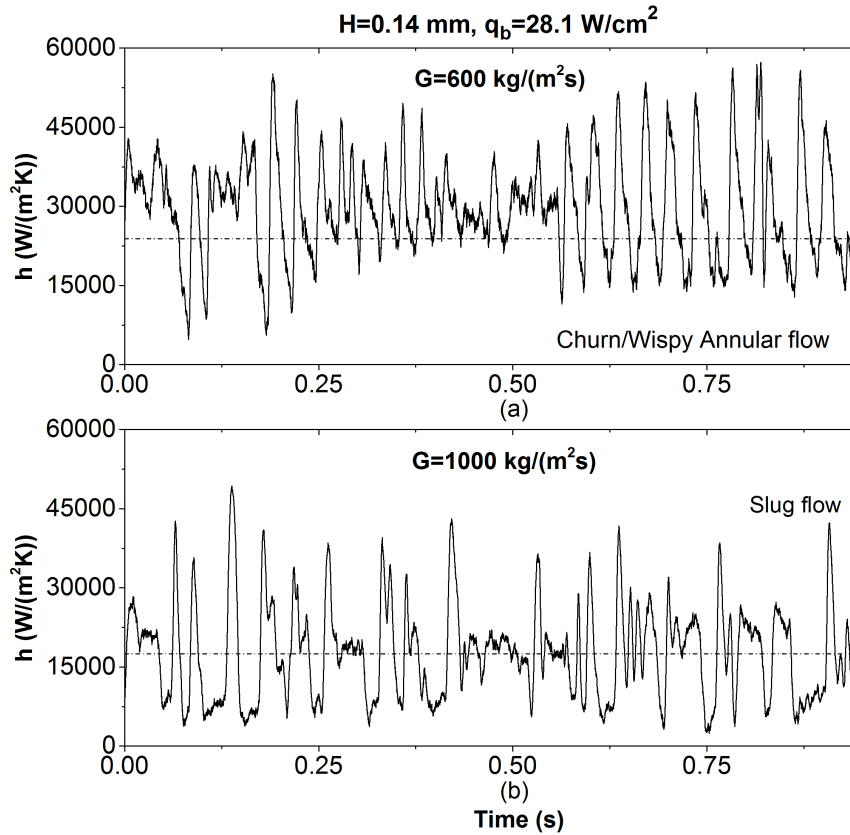


FIGURE 5.26: Variation of heat transfer coefficient with time for $H = 0.14 \text{ mm}$, $q_b = 28.1 \text{ W/cm}^2 (\pm 3.2\%)$ for mass fluxes (a) $600 \text{ kg/(m}^2\text{s)}$ (b) $1000 \text{ kg/(m}^2\text{s)}$

The peaks in heat transfer coefficient too are higher for low mass flux case. This could be due to higher bulk mean fluid temperature of $95.6 \text{ }^\circ\text{C}$ for $G = 600 \text{ kg/(m}^2\text{s)}$ compared to $90.4 \text{ }^\circ\text{C}$ for $G = 1000 \text{ kg/(m}^2\text{s)}$ at the sensor location. Lower fluid temperature of the fluid implies more heat being used for sensible heating of the liquid rather than evaporating the thin film during passage of vapour slug, thus preventing thinning down of the liquid film before it gets accumulated by virtue to cohesive force to maintain a certain wall contact angle.

Due to more frequent slugs, the liquid slugs were comparatively short for $G = 600 \text{ kg/(m}^2\text{s)}$. So the heat transfer coefficient at valleys was generally

larger than those seen for $G = 1000 \text{ kg}/(\text{m}^2\text{s})$. At times however, partial dry-out lead to very low valleys.

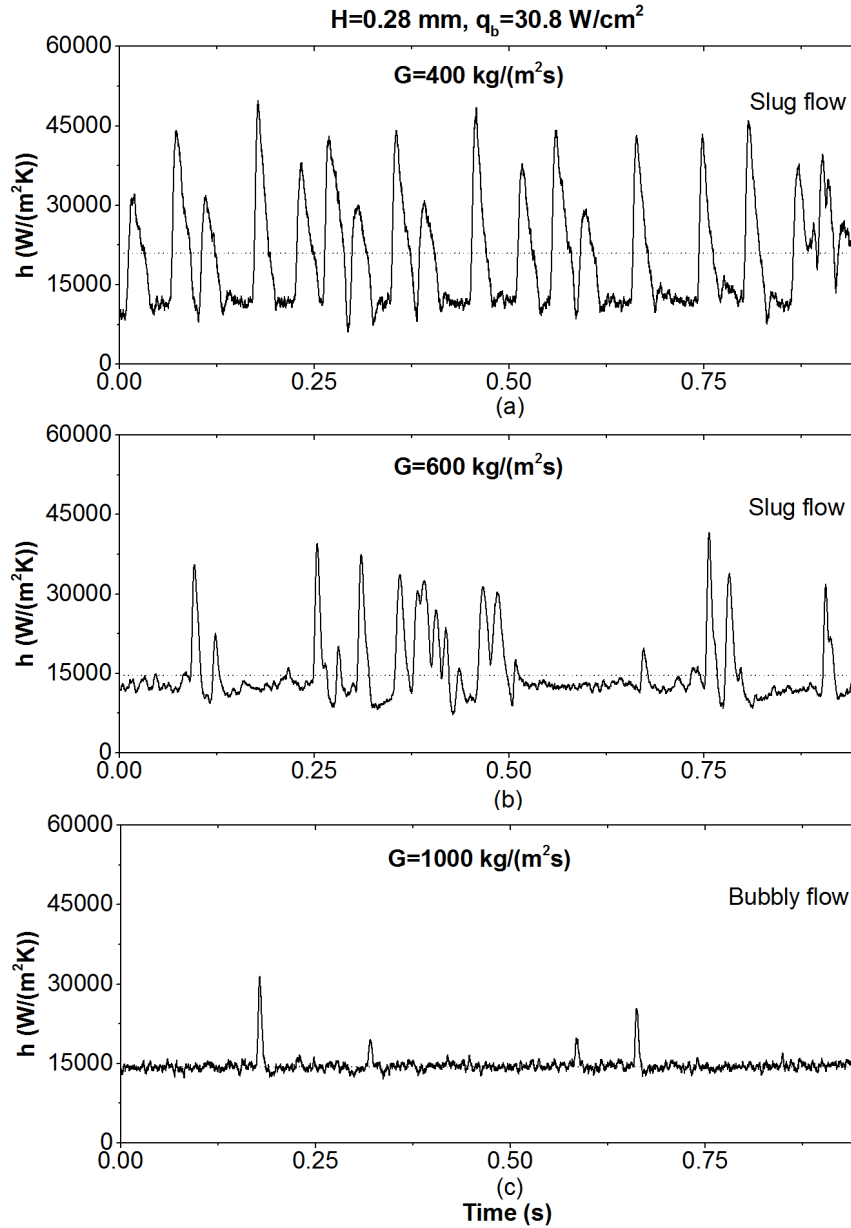


FIGURE 5.27: Variation of heat transfer coefficient with time for $H = 0.28 \text{ mm}$, $q_b = 30.8 \text{ W}/\text{cm}^2 (\pm 3\%)$ for mass fluxes (a) $400 \text{ kg}/(\text{m}^2\text{s})$ (b) $600 \text{ kg}/(\text{m}^2\text{s})$ (c) $1000 \text{ kg}/(\text{m}^2\text{s})$

The trends seen for Figure 5.27 are similar to those seen in Figure 5.26 and explanation that follows is similar. For highest mass flux of $1000 \text{ kg}/(\text{m}^2\text{s})$,

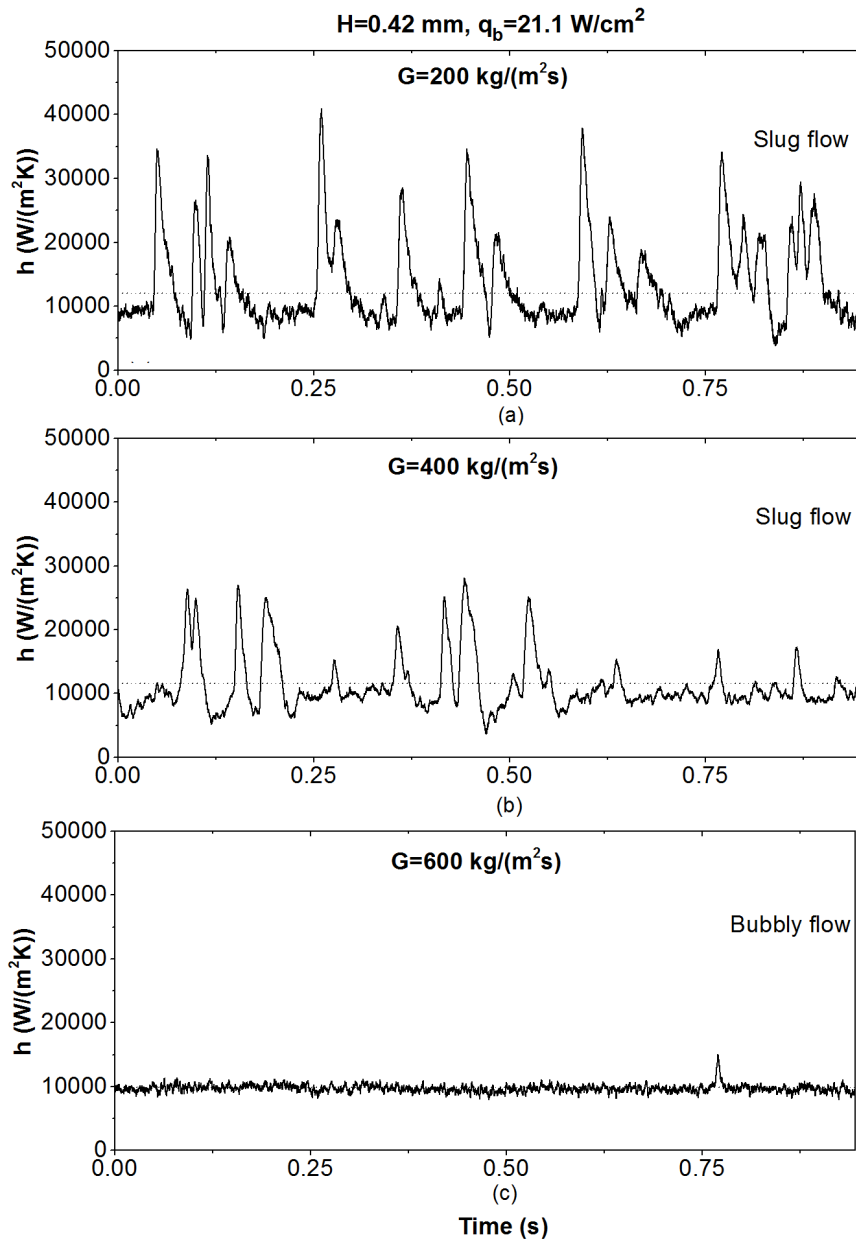


FIGURE 5.28: Variation of heat transfer coefficient with time for $H = 0.42 \text{ mm}$, $q_b = 21.1 \text{ W/cm}^2 (\pm 2.8\%)$ for mass fluxes (a) $200 \text{ kg/(m}^2\text{s)}$ (b) $400 \text{ kg/(m}^2\text{s)}$ (c) $600 \text{ kg/(m}^2\text{s)}$

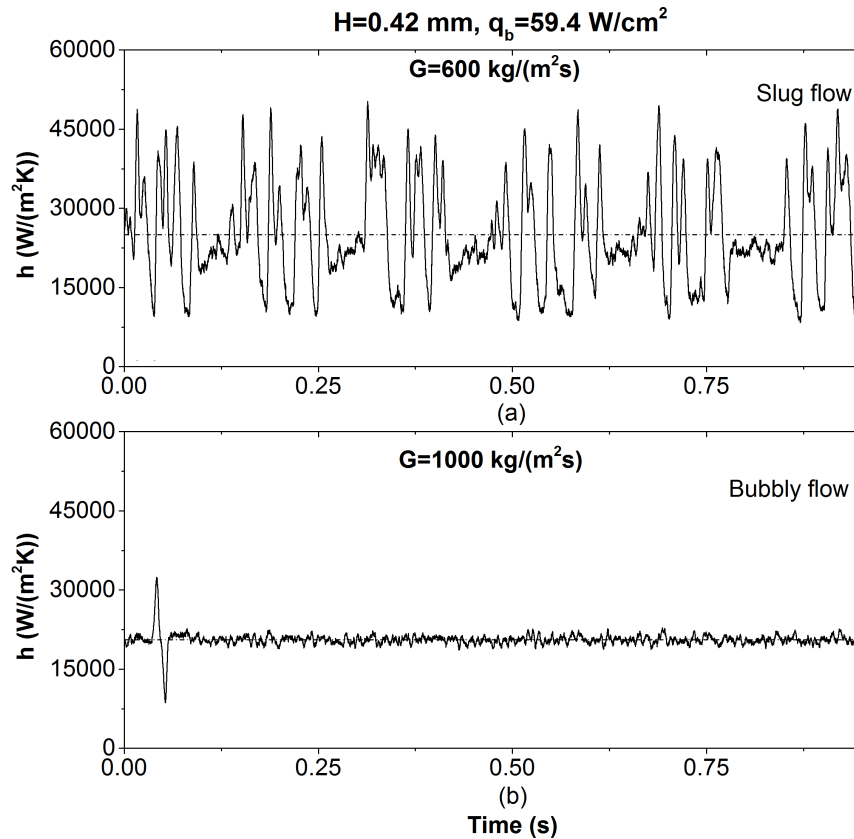


FIGURE 5.29: Variation of heat transfer coefficient with time for $H = 0.42$ mm, $q_b = 59.4$ W/cm^2 ($\pm 2.3\%$) for mass fluxes (a) 600 $kg/(m^2s)$ (b) 1000 $kg/(m^2s)$

hardly any bubbles were seen since the average wall superheat was only $2.4^\circ C$. Hence the peaks in heat transfer which happen due to elongated bubbles/slugs are very scarce.

The average wall superheat for 400 $kg/(m^2s)$ and 600 $kg/(m^2s)$ was $3.3^\circ C$ and $6^\circ C$. Yet, due to greater effect of flow confinement for smaller mass flux, the slug frequency and hence the number of peaks are much greater for mass flux of 400 $kg/(m^2s)$. The peak values are somewhat greater due to larger bulk mean temperature of $92.9^\circ C$ for $G = 400$ $kg/(m^2s)$ compared to $90.2^\circ C$ for $G = 600$ $kg/(m^2s)$.

The trend for Figure 5.28 is same as those observed for Figures 5.26 and 5.27. Due to less confinement effects, bubbly flow was observed for mass flux of $G = 600 \text{ kg}/(\text{m}^2\text{s})$.

Figure 5.29 shows that for mass flux of $600 \text{ kg}/(\text{m}^2\text{s})$, slug flow was observed and the fluctuations in heat transfer coefficient were very significant. Due to high frequency of slugs and fairly high peak values, the average heat transfer coefficient value is higher than that for mass flux of $1000 \text{ kg}/(\text{m}^2\text{s})$ during which bubbly flow was observed.

The high and low value of heat transfer coefficient in valleys for mass flux of $600 \text{ kg}/(\text{m}^2\text{s})$ were due to short liquid slugs and partial dry-outs respectively.

5.3 Detection of Flow Regimes

Figure 5.30 shows typical sensor temperature verses time data for some of the selected conditions under which various flow regimes were observed. A cursory look gives an idea about the unique temperature signature of each of the flow regimes. While single phase flow has the least fluctuations, the same for bubbly flow are relatively larger. For slug flow as well as for Churn/Wispy annular flow, the fluctuations are even larger.

There were three probable data-reduction procedures considered that could be used to identify flow regimes.

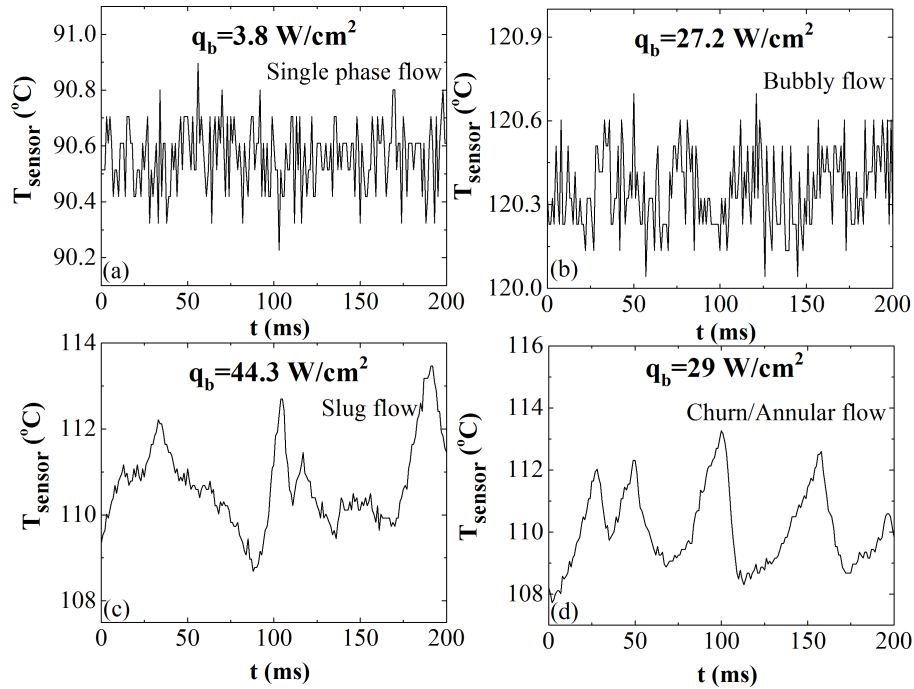


FIGURE 5.30: Typical temperature (measured by sensor) versus time curve for different flow regimes (a) Single phase flow for $H = 0.14 \text{ mm}$, $G = 1000 \text{ kg}/(\text{m}^2\text{s})$ (b) Bubbly flow for $H = 0.42 \text{ mm}$, $G = 1000 \text{ kg}/(\text{m}^2\text{s})$ (c) Slug flow for $H = 0.14 \text{ mm}$, $G = 1000 \text{ kg}/(\text{m}^2\text{s})$ (d) Churn/Wispy-annular flow for $H = 0.14 \text{ mm}$, $G = 600 \text{ kg}/(\text{m}^2\text{s})$

1. Standard deviation of sensor temperature data: Although very simple to apply, the difficulty with standard deviation is that temperature data is typically measured below the wetted surface. This leads to damping (due to thermal capacitance of the solid substrate) of temporal fluctuations in temperature due to phenomena occurring on the wetted surface. This damping is not only a function of substrate properties and depth of temperature sensor from the wetted surface but also the frequency components present in the temperature-time data as shown in Figure 4.5. Even if regimes could be differentiated for the present experimental conditions from standard deviation values, it would lack general applicability. This method is thus

avoided.

2. Direct application of FFT on temperature sensor data followed by the use of methodology described in section 4.3 to correct for damping of amplitudes of different frequencies.
3. The use of IHCP solution method to first calculate the wetted surface temperature followed by application of FFT on this temperature.

Figure 5.31 shows a comparison between the second and third idea considered for various experimental conditions under which different flow regimes were observed. It can be observed from Figures 5.31 (c),(d) and (e) that there is a very good agreement in the frequency domain, between the two methods, especially for lower frequencies (below 80 Hz). For higher frequencies, the data reduction procedure based on the third method (involving the use of T_w) leads to smaller amplitudes compared to that obtained from the second method (involving the direct use of T_{sensor}). For Figure 5.31 (a) and (b) the difference in amplitude seems much more prominent, since the y-scale is relatively smaller. The discrepancy in the frequency domain for the two methods increases as the frequency increases. This is due to the presence of noise in the T_{sensor} data. Also, the correction for higher frequency is much larger (refer to Figure 4.5 and note the decreasing value of amplitude ratio with increasing frequency) leading to much greater amplification of noise at higher frequencies. Contrastingly, for T_w , since IHCP solution dampens the noise very well, this effect is not observed

for T_w based curve. These are the reasons for differences in the frequency-domain of the two methodologies.

The second method seems to be the best due to clear distinction in the some of the highest peak amplitudes for different flow regimes. However, the algorithm for post-processing is much more complex than that for the third method. This could make things difficult for real-time applications. Fortunately, within certain limits the third method is still applicable.

For frequency components less than 80 Hz , the third method is nearly as good as the second method for distinction of the flow regimes. Moreover, the relative simplicity of the method makes it more practical for application purpose. Hence, unless much higher frequencies are dominant and unless the sensor noise (having standard deviation of $\approx 0.1 \text{ }^\circ\text{C}$ in the present case) is too large, the third method is good enough. If sensor noise is much smaller and/or if the sensor depth is smaller and/or the thermal diffusivity of the solid substrate material is large (non-dimensional frequency would be less in that case and amplitude ratio would be large implying a smaller amplification of noise), it is expected that frequencies much greater than 80 Hz can also be well captured.

For each of the conditions presented in table 5.1, a number of heat fluxes were tested. However, for brevity, results of only some of the heat fluxes have been shown in Figures 5.32 to 5.40 to demonstrate the differences in some of the maximum peak amplitudes in the frequency for different flow regimes.

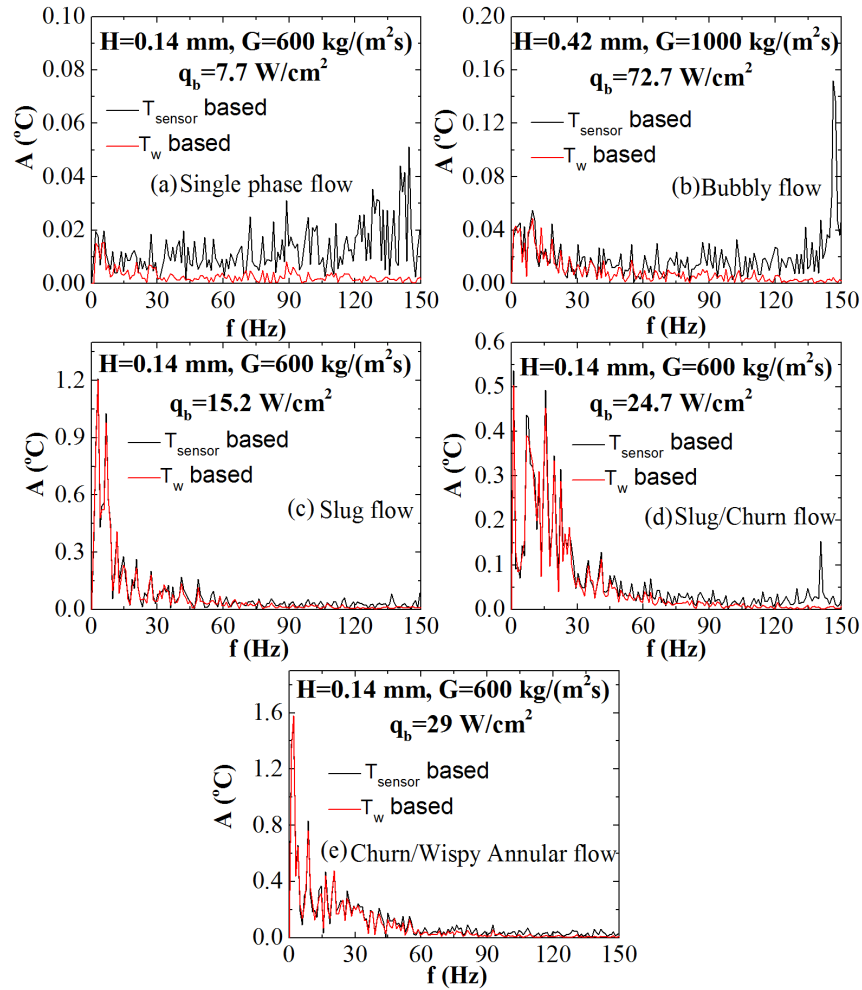


FIGURE 5.31: Comparison of frequency domain obtained directly using transient wall (wetted surface) temperature and corrected frequency domain of temperature sensor data for (a) Single phase flow (b) Bubbly flow (c) Slug flow (d) Slug/Churn flow (e) Churn/Wispy Annular flow

Figure 5.41, shows the regime detection chart summarizing the observations. For single phase flow, amplitude of all peaks were below $0.03\text{ }^{\circ}\text{C}$ for frequencies less than 80 Hz . For bubbly flow several of the highest of amplitude peaks ranged from $0.04 - 0.25\text{ }^{\circ}\text{C}$. While Slug flow, Churn flow and Wispy annular flow could not be distinguished among each other, some of the highest of peaks for all cases were much greater ($> 0.35\text{ }^{\circ}\text{C}$) compared to single phase and bubble flow.

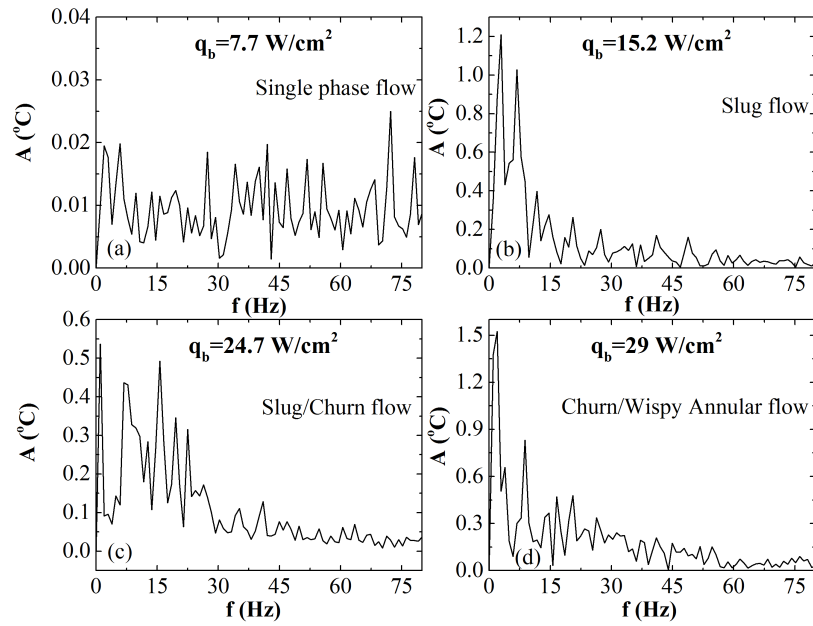


FIGURE 5.32: Corrected frequency domain of temperature (measured by sensor) versus time data for $H = 0.14 \text{ mm}$, $G = 600 \text{ kg}/(\text{m}^2 \text{ s})$ for various heat fluxes

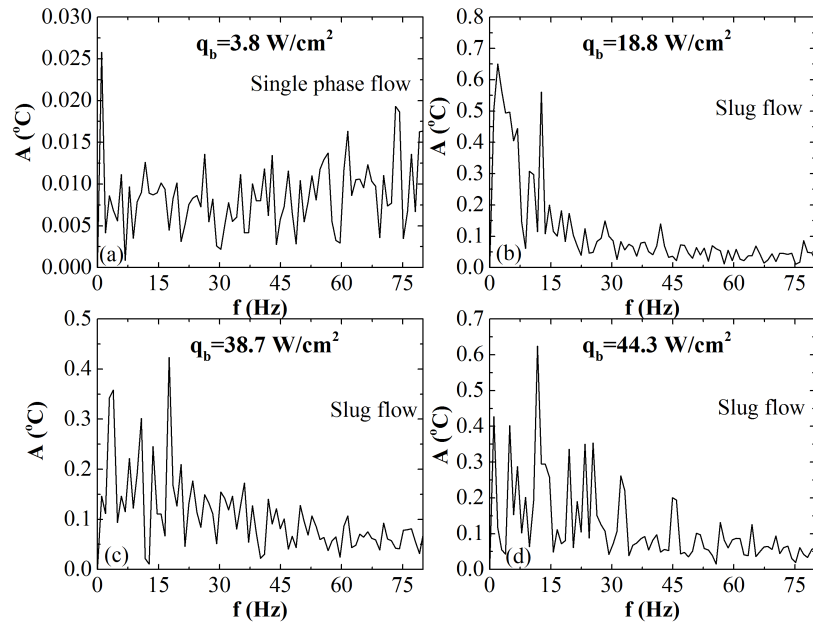


FIGURE 5.33: Corrected frequency domain of temperature (measured by sensor) versus time data for $H = 0.14 \text{ mm}$, $G = 1000 \text{ kg}/(\text{m}^2 \text{ s})$ for various heat fluxes

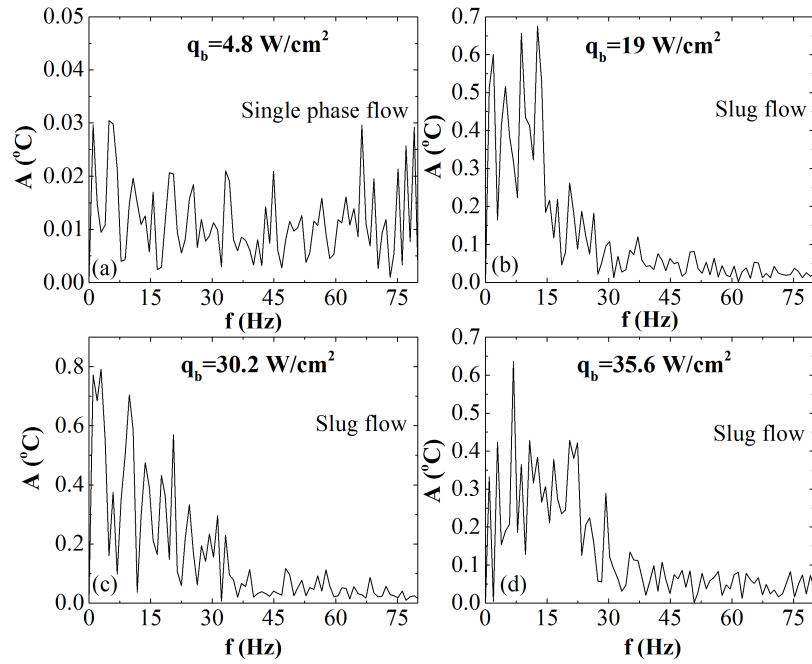


FIGURE 5.34: Corrected frequency domain of temperature (measured by sensor) verses time data for $H = 0.28 \text{ mm}$, $G = 400 \text{ kg}/(\text{m}^2\text{s})$ for various heat fluxes

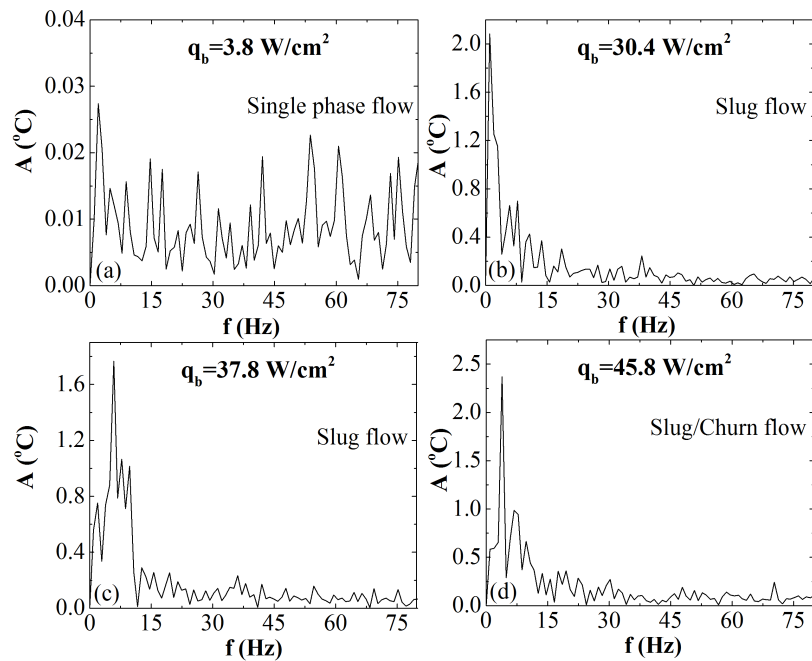


FIGURE 5.35: Corrected frequency domain of temperature (measured by sensor) verses time data for $H = 0.28 \text{ mm}$, $G = 600 \text{ kg}/(\text{m}^2\text{s})$ for various heat fluxes

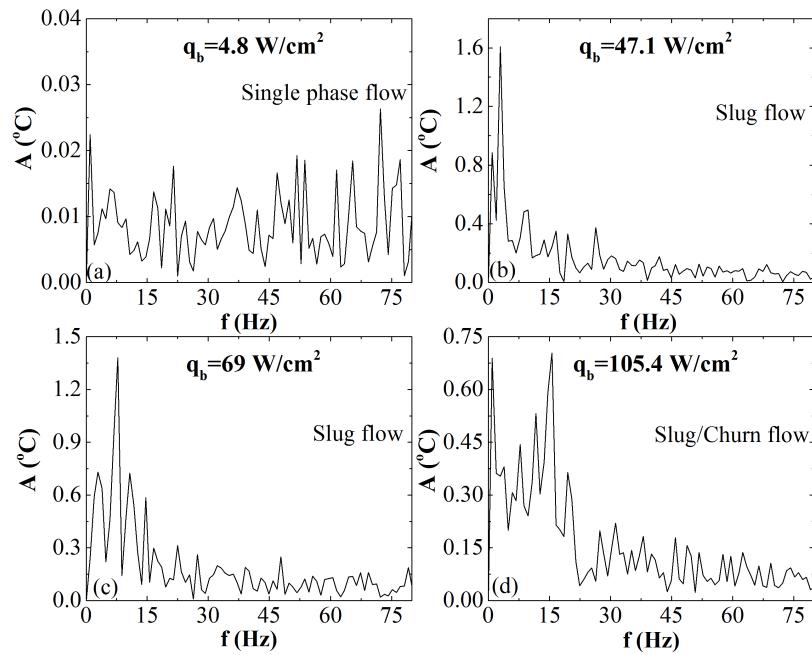


FIGURE 5.36: Corrected frequency domain of temperature (measured by sensor) versus time data for $H = 0.28 \text{ mm}$, $G = 1000 \text{ kg}/(\text{m}^2\text{s})$ for various heat fluxes

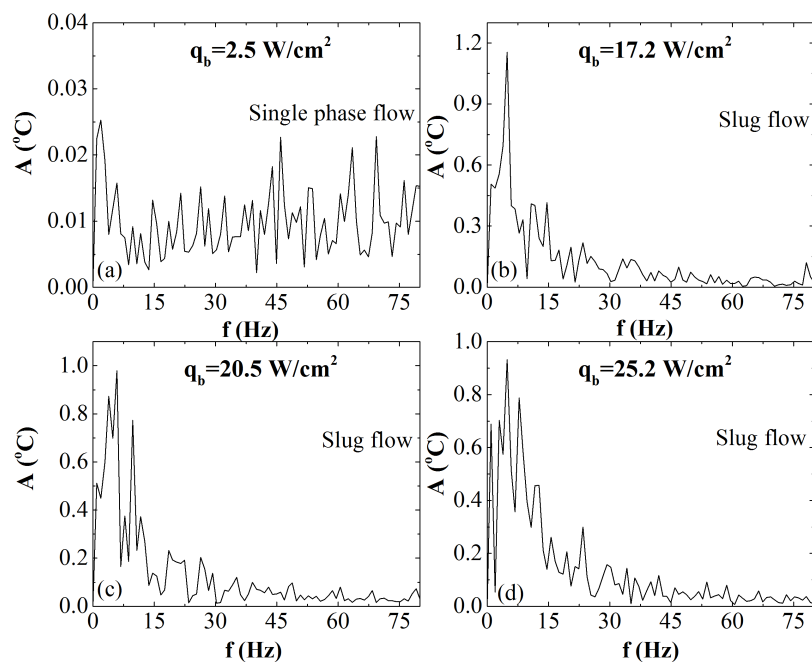


FIGURE 5.37: Corrected frequency domain of temperature (measured by sensor) versus time data for $H = 0.42 \text{ mm}$, $G = 200 \text{ kg}/(\text{m}^2\text{s})$ for various heat fluxes

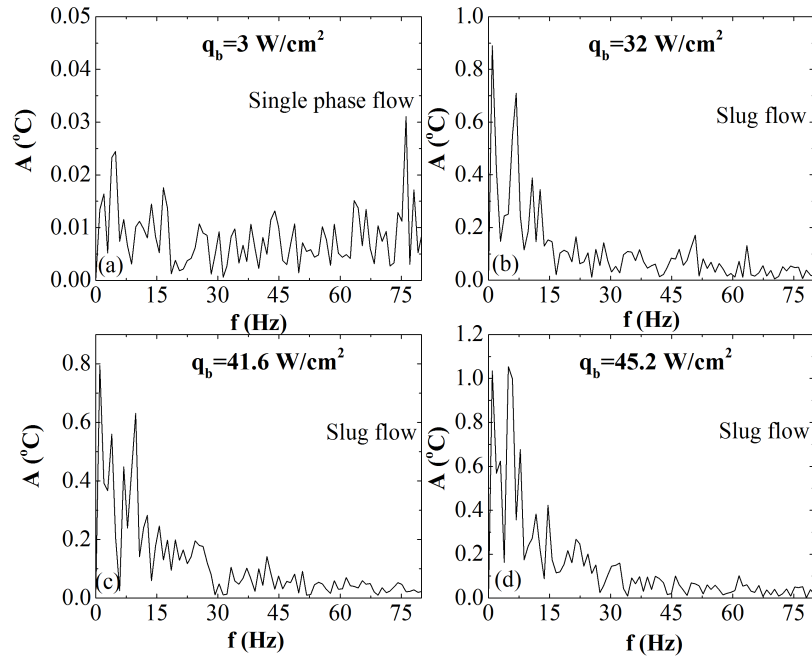


FIGURE 5.38: Corrected frequency domain of temperature (measured by sensor) versus time data for $H = 0.42 \text{ mm}$, $G = 400 \text{ kg}/(\text{m}^2\text{s})$ for various heat fluxes

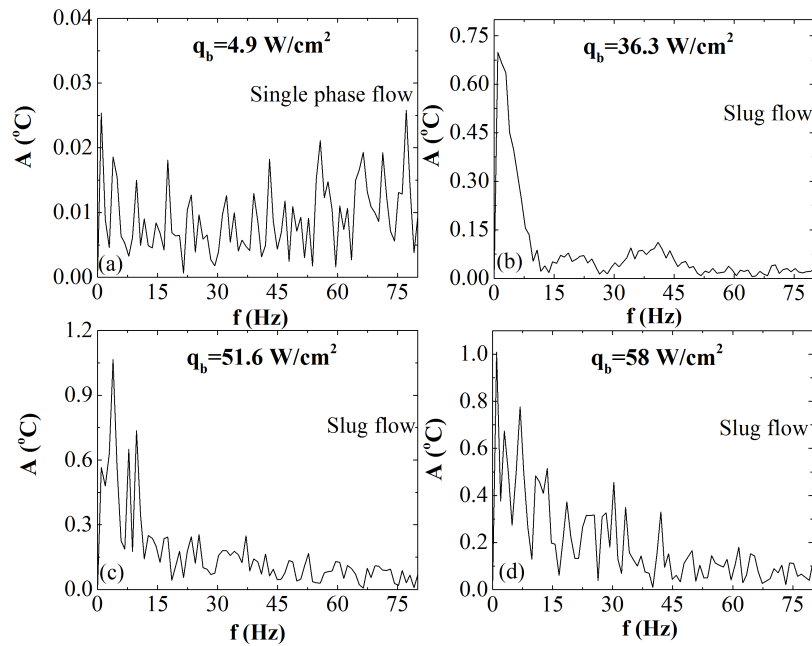


FIGURE 5.39: Corrected frequency domain of temperature (measured by sensor) versus time data for $H = 0.42 \text{ mm}$, $G = 600 \text{ kg}/(\text{m}^2\text{s})$ for various heat fluxes

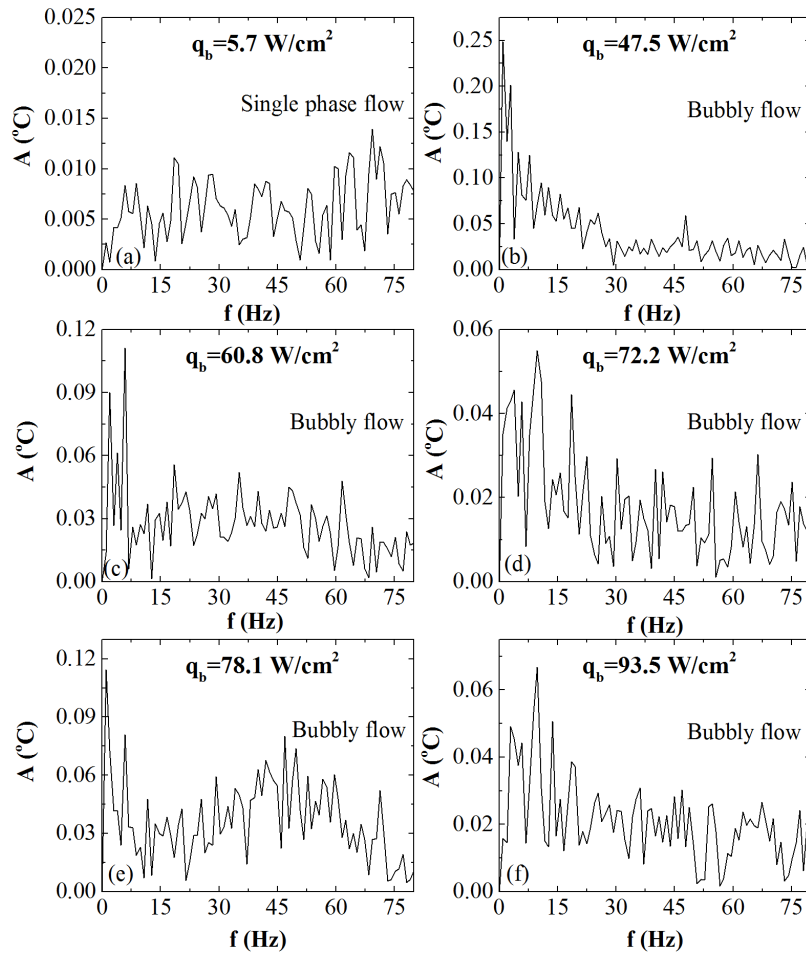


FIGURE 5.40: Corrected frequency domain of temperature (measured by sensor) versus time data for $H = 0.42 \text{ mm}$, $G = 1000 \text{ kg}/(\text{m}^2\text{s})$ for various heat fluxes

Single phase flow (for steady-state condition) in Figures 5.32 to 5.40 should ideally not have had any frequency components and the curve should have simply coincided with the x-axis. However, due to non-ideal experimental conditions, primarily the inherent noise in temperature measurement leads to some temperature fluctuations leading to non-zero amplitudes in frequency domain. During bubbly flow, the temperature fluctuations are relatively higher than that

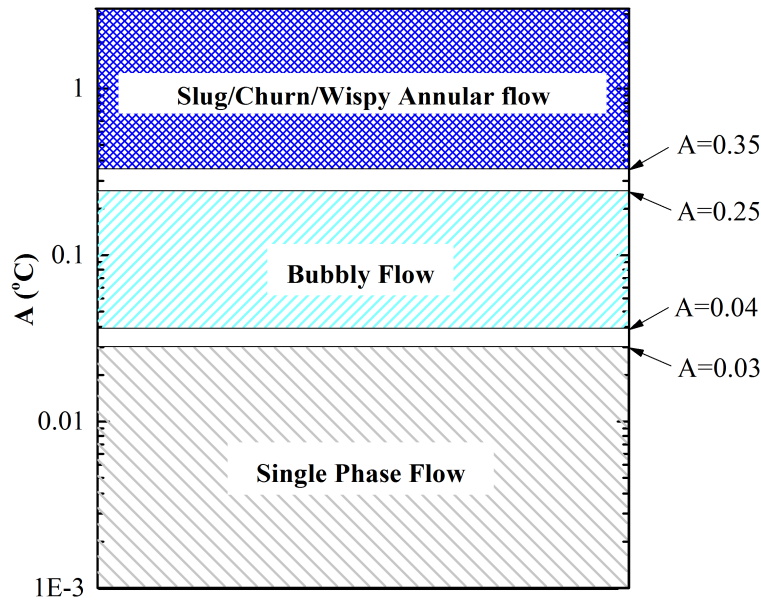


FIGURE 5.41: Regime detection chart

of single-phase flow since single-phase is steady (ideally) while boiling phenomena is unsteady. Immediately following bubble nucleation, there is a sudden increase in heat transfer coefficient due to release of accumulated superheat (utilized in evaporation, owing to the latent heat) in the surrounding liquid [88]. This increased heat transfer coefficient in turn leads to decreased wall temperature. However, during the waiting time (time period between bubble detachment and ebullition of another bubble), since there is single phase flow, the heat transfer coefficient again reduces and consequently, the wall temperature increases. Hence, amplitudes are larger for bubbly flow compared to single phase flow.

Slug flow regime generally involves three distinct features as shown in Figure 5.15; (i) elongated vapour bubble (slug) flow during which the heat transfer coefficient is very high owing to thin film evaporation (ii) local dry-out during which the heat transfer coefficient is very low (iii) liquid slug flow during the

passage of which heat transfer coefficient is intermediate [15]. Due to multiplicity of heat transfer mechanisms and large difference in heat transfer coefficient associated with each of them, the temperature fluctuations during slug flow are very large. During Churn flow and Wispy annular flow, the hydrodynamics and heat transfer are complex. These flow regimes may include thin film evaporation of liquid film (whose thickness may vary with time), nucleation of smaller bubbles and periods of partial-dry-out. This phenomenon leads to temperature fluctuations which are as high as those observed during slug flow regime.

It was anticipated that with increase in heat flux, due to increase in number of bubbles and slugs, the dominant frequency would shift to higher frequencies. But contrarily to expectations, this was not observed. The lack of increase in dominant frequencies with increasing heat flux is likely due to stochastic nature of the bubble/slug ebullition and passage leading to distributed peaks rather than a single large peak. Moreover, temperature variation during a complete slug cycle is not sinusoidal. These reasons likely explain the counter-intuitive results.

These are also the reasons, that for conditions under which slug flow regime was observed, although a relatively large peak was observed in the frequency-domain at a frequency corresponding to the frequency of passage of slug (as seen from high speed flow visualization), there were other peaks too, which could often have larger amplitudes. Hence, neither was a pattern such as increase in dominant frequencies was observed with increase in heat flux nor was it possible to detect the slug frequency from peaks in frequency domain.

Chapter 6

Conclusions and Recommendations for Future Work

Sub-cooled flow boiling phenomena in a single low aspect ratio microchannel was investigated using DI water as the coolant. Mass fluxes tested were 200, 400, 600 and 1000 $kg/(m^2s)$ for a microchannel with a width of 2.54 mm , length of 25.4 mm and heights 0.14, 0.28 and 0.42 mm . Several heat fluxes were tested, the maximum being 105 W/cm^2 . Time-averaged results for both pressure drop and heat transfer were presented. Numerical method involving solution technique for Inverse Heat Conduction Problem (IHCP) was first tested for a number of cases and then applied to transient temperature data captured synchronously with video frames during experiments. Transient results thus obtained were also presented for aforementioned conditions. This provided unique insights into the flow boiling phenomena. Transient temperature data was also shown to be useful for detection of flow boiling regimes.

The following section summarizes the important conclusions from the presented work. Lastly, based on insights gained from this thesis, recommendations for future work have been provided.

6.1 Conclusions

1. Confinement of bubble was observed for most of the cases and hence slug flow regime was the most pre-dominant. A cycle typically commences with nucleation of bubble. It grows to become a slug confined by the small microchannel dimensions. This is followed by detachment from nucleation site and expansion/acceleration longitudinally as well as entrapment of a thin film of liquid on the wetted surface. This film thins down and accumulates leading to partial dryout. Re-wetting is then observed when liquid slug passes.
2. Pressure drop was found to be sensitive to heat flux for all cases except when bubbly flow was prevalent. Pressure drop was significantly higher for smaller microchannels for a given heat flux and mass flux due to (a) larger frictional pressure drop and (b) accelerational pressure drop due to greater amount of vapour (having much larger specific volume compared to liquid) being generated. For a microchannel of given height, for a given heat flux, pressure drop was also higher for higher mass fluxes due to greater frictional component of pressure drop. For some cases, the pressure drop for high and low mass fluxes was the same. This was due to greater accelerational component of pressure drop for smaller mass flux due to greater quantity of vapour being formed.
3. ONB (Onset of Nucleate Boiling) on the boiling curve and heat transfer coefficient verses heat flux curve is identified by a sharp increase in slope.

The boiling curve is nearly vertical for two-phase region and it can be easily distinguished from single-phase region. The heat transfer coefficient also increases quite drastically with heat flux. In two-phase region, the boiling curve for a given mass flux is observed to shift towards higher wall superheat for larger microchannel height, since onset of nucleation is delayed for larger microchannels. Correspondingly heat transfer coefficient too is relatively inferior since vapour confinement effects too are relatively lesser. Larger mass flux was also observed to elevate the superheat required for onset of nucleate boiling for a given channel height. In general the boiling curve shifts towards higher wall superheat for greater mass fluxes due to lesser confinement effects which also result in relatively lower heat transfer coefficient. However, sometimes due to low bulk mean fluid temperature, the wall superheat was lower for high mass fluxes.

4. During flow boiling in microchannels, variations in heat transfer coefficient, wall heat flux and temperature are very significant with time. In fact, constant wall heat flux boundary condition is found to be invalid. While the trend in wall heat flux follows that of heat transfer coefficient, the wall temperature is observed to increase when heat transfer coefficient is low and it decreases sharply when heat transfer coefficient increases. Because of coupling of heat transfer coefficient (governed by boiling phenomena) and wall temperature, it is apparent that wall thickness/material

plays a role in determining how quickly the temperature fluctuates, thus influencing boiling phenomena and heat transfer coefficient.

5. Heat transfer coefficient increases as the slug nose arrives. This is due to evaporation of liquid at the interface causing quenching of surrounding liquid as well as due to flow structures at the slug nose that promote mixing within the liquid.
6. Peaks in heat transfer coefficient occur during passage of vapour slugs due to thin film evaporation. Thus, thin film evaporation is found to be the primary mechanism responsible for enhanced heat transfer during slug flow.
7. The peak value of heat transfer coefficient depends on initial thin film thickness trapped when the slug just arrives at a location. This in turn depends on distance of bubble incipience as well as any phenomena in the downstream region which affects the fluid flow influencing the development of hydrodynamic boundary layer. In fact, due to stagnation caused by a downstream slug, trailing slugs lead to smaller peaks in heat transfer coefficient due to thicker initial film of liquid trapped above the wetted surface.
8. Heat flux at a given mass flux and microchannel height also influences the peak heat transfer coefficient. Higher heat flux leads to higher bulk mean fluid temperature and faster thinning down of thin film before the film accumulates thus facilitating higher peaks. Since accumulation of a film

of liquid is governed by surface-wettability, it also affects the heat transfer coefficient. For high heat fluxes, even the frequency of slugs were higher since higher heat flux implies faster rise in wetted surface temperature thus leading to faster nucleation events.

9. At a given heat flux and mass flux, for smaller microchannels the peaks in heat transfer coefficient were larger due to thinner film of liquid trapped initially during passage of slug. The spatially and temporally averaged wall superheat and bulk mean temperature too affect the frequency of peaks in heat transfer coefficient.
10. At a given heat flux and microchannel height, peaks and frequency in heat transfer coefficient were respectively higher and larger for lower mass fluxes. Higher bulk mean fluid temperature and greater confinement effects for smaller mass fluxes is thought to be responsible for this observation.
11. Small peaks were observed during passage of 3-phase contact line. It covers a very small region and its residence time at a given location too is small. Hence, it does not contribute significantly to the overall high heat transfer seen during slug-flow regime.
12. During the passage of liquid slug, the heat transfer coefficient was lower than that during thin film evaporation. Passage of shorter and fast moving liquid slugs lead to higher heat transfer coefficient compared to longer and/or slow moving ones. Difference in temperature profile development

length and recirculation time within the liquid slug are the likely reasons for the differences in heat transfer coefficient due to length and velocity of liquid slug.

13. A simple methodology based on transient temperature is developed to diagnose flow regimes. Single phase flow, bubbly flow and slug/churn/wispy-annular flow could be clearly differentiated by looking at some of the highest of peaks in amplitude in the corrected frequency domain of wall temperature for frequencies below 80 Hz . For single phase flow, all peaks were below $0.03\text{ }^{\circ}\text{C}$. For bubbly flow, several of the highest of peaks ranged from $0.04 - 0.25\text{ }^{\circ}\text{C}$. While for slug flow, churn flow and wispy annular flow, the highest of peaks were greater than $0.35\text{ }^{\circ}\text{C}$. Suggestions have also been given to increase the limit of maximum frequency for which results can be relied upon.

6.2 Recommendations for Future Work

1. The range of heat flux, mass flux and the channel dimensions are limited. A similar study including time-averaged and transient variables can be carried out for a wider set of parameters. Studies on dielectric fluids should also be carried out since their properties are quite different from that of water.
2. The maximum value of heat flux was limited due to limitations of the thermal test chip used in this work hence only sub-cooled experiments

could be performed. Future endeavors could carry out similar studies for saturated boiling as well and could also include the study of CHF.

3. It is worth checking the effect of heater depth on the heat transfer performance of the microchannels. This is because a strong coupling was found between transient variations of surface temperature and heat flux with the transient flow-regime.
4. Effect of inlet/outlet compressibility on transient evolution of heat transfer can be studied.
5. Boiling is a phenomena that is very difficult to control. There were a number of different randomly active nucleation sites on the microchannel. Study on a microchannel with a very smooth surface with artificial nucleation sites (ANS) may be able to offer pre-determined well controlled boiling sites. A parametric analysis can then be conducted and effect of various parameters like distance of bubble incipience, slug length, liquid slug length, heat flux, mass flux, microchannel dimensions etc on transient heat transfer can be well quantified and a semi-analytical model can be developed.
6. Numerical simulations for flow boiling in microchannels can be carried out, not with just the fluid domain alone, but should also include the solid domain between the wetted surface and heater, to better simulate the experimental phenomena. Simulation heat transfer results should then be compared to transient experimental heat transfer results for validation.

Parametric analysis and ease of control of variables during simulations can offer invaluable information regarding local and temporal variations of hydrodynamic and thermal fields, thus enabling an understanding that could ultimately lead to mechanistic heat transfer models.

7. The methodology for regime-detection can be tested for a wider set of heat fluxes, mass fluxes, fluids etc. Use of better sensors (with lower noise) can increase the limit to which higher frequencies can be captured reliably. This method can be used and research work can be conducted to optimize a smart feed-back control of flow-rate for optimal heat transfer performance and minimum pumping power.

Bibliography

- [1] Lian Zhang, Evelyn N. Wang, Kenneth E. Goodson, and Thomas W. Kenny. Phase change phenomena in silicon microchannels. *International Journal of Heat and Mass Transfer*, 48(8):1572–1582, April 2005. ISSN 00179310. doi: 10.1016/j.ijheatmasstransfer.2004.09.048. URL <http://linkinghub.elsevier.com/retrieve/pii/S0017931004005228>.
- [2] Milnes P. David, Julie E. Steinbrenner, Josef Miler, and Kenneth E. Goodson. Adiabatic and diabatic two-phase venting flow in a microchannel. *International Journal of Multiphase Flow*, 37(9):1135–1146, November 2011. ISSN 03019322. doi: 10.1016/j.ijmultiphaseflow.2011.06.013. URL <http://linkinghub.elsevier.com/retrieve/pii/S0301932211001455>.
- [3] I. Mudawar. Assessment of high-heat-flux thermal management schemes. *IEEE Transactions on Components and Packaging Technologies*, 24(2):122–141, 2001. ISSN 15213331. doi: 10.1109/6144.926375.
- [4] Milnes P. David, Josef Miler, Julie E. Steinbrenner, Yizhang Yang, Maxat Touzelbaev, and Kenneth E. Goodson. Hydraulic and thermal characteristics of a vapor venting two-phase microchannel heat exchanger. *International Journal of Heat and Mass Transfer*, 54(25-26):5504–5516, December 2011. ISSN 00179310. doi: 10.1016/j.ijheatmasstransfer.2011.

Bibliography

- 07.040. URL <http://linkinghub.elsevier.com/retrieve/pii/S0017931011004261>.
- [5] David Fogg. *Bubble Dynamics in Microchannel Flow Boiling*. PhD thesis, Stanford University, 2007.
- [6] G M Lazarek and S H Black. Evaporative heat transfer , pressure drop and critical heat flux in a small vertical tube with R-113. *International Journal of Heat and Mass Transfer*, 25(7):945–960, 1982.
- [7] Issam Mudawar and Morris B. Bowers. Ultra-high critical heat flux (CHF) for subcooled water flow boiling-I: CHF data and parametric effects for small diameter tubes. *International Journal of Heat and Mass Transfer*, 42:1405–1428, 1999. ISSN 00179310. doi: 10.1016/S0017-9310(98)00241-5.
- [8] Tamanna Alam, Poh Seng Lee, Christopher R. Yap, and Liwen Jin. A comparative study of flow boiling heat transfer and pressure drop characteristics in microgap and microchannel heat sink and an evaluation of microgap heat sink for hotspot mitigation. *International Journal of Heat and Mass Transfer*, 58(1-2):335–347, March 2013. ISSN 00179310. doi: 10.1016/j.ijheatmasstransfer.2012.11.020. URL <http://linkinghub.elsevier.com/retrieve/pii/S0017931012008757>.
- [9] Susan N. Ritchey, Justin a. Weibel, and Suresh V. Garimella. Local measurement of flow boiling heat transfer in an array of non-uniformly heated

- microchannels. *International Journal of Heat and Mass Transfer*, 71:206–216, April 2014. ISSN 00179310. doi: 10.1016/j.ijheatmasstransfer.2013.12.012. URL <http://linkinghub.elsevier.com/retrieve/pii/S0017931013010569>.
- [10] Tannaz Harirchian and Suresh V. Garimella. Microchannel size effects on local flow boiling heat transfer to a dielectric fluid. *International Journal of Heat and Mass Transfer*, 51(15-16):3724–3735, July 2008. ISSN 00179310. doi: 10.1016/j.ijheatmasstransfer.2008.03.013. URL <http://linkinghub.elsevier.com/retrieve/pii/S001793100800183X>.
- [11] Tannaz Harirchian and Suresh V. Garimella. Effects of channel dimension, heat flux, and mass flux on flow boiling regimes in microchannels. *International Journal of Multiphase Flow*, 35(4):349–362, April 2009. ISSN 03019322. doi: 10.1016/j.ijmultiphaseflow.2009.01.003. URL <http://linkinghub.elsevier.com/retrieve/pii/S030193220900007X>.
- [12] Tamanna Alam, Poh Seng Lee, Christopher R Yap, and Liwen Jin. Experimental investigation of local flow boiling heat transfer and pressure drop characteristics in microgap channel. *International Journal of Multiphase Flow*, 42:164–174, 2012. ISSN 0301-9322. doi: 10.1016/j.ijmultiphaseflow.2012.02.007. URL <http://dx.doi.org/10.1016/j.ijmultiphaseflow.2012.02.007>.

- [13] K. Balasubramanian, M. Jagirdar, P.S. Lee, C.J. Teo, and S.K. Chou. Experimental investigation of flow boiling heat transfer and instabilities in straight microchannels. *International Journal of Heat and Mass Transfer*, 66:655–671, November 2013. ISSN 00179310. doi: 10.1016/j.ijheatmasstransfer.2013.07.050. URL <http://linkinghub.elsevier.com/retrieve/pii/S0017931013006042>.
- [14] W Qu and I Mudawar. Flow boiling heat transfer in two-phase micro-channel heat sinksII. Annular two-phase flow model. *International Journal of Heat and Mass Transfer*, 46(15):2773–2784, July 2003. ISSN 00179310. doi: 10.1016/S0017-9310(03)00042-5. URL <http://linkinghub.elsevier.com/retrieve/pii/S0017931003000425>.
- [15] J Thome, V Dupont, and Anthony M. Jacobi. Heat transfer model for evaporation in microchannels. Part I: presentation of the model. *International Journal of Heat and Mass Transfer*, 47(14-16):3375–3385, July 2004. ISSN 00179310. doi: 10.1016/j.ijheatmasstransfer.2004.01.006. URL <http://linkinghub.elsevier.com/retrieve/pii/S0017931004000316>.
- [16] Tannaz Harirchian and Suresh V Garimella. Flow regime-based modeling of heat transfer and pressure drop in microchannel flow boiling. *International Journal of Heat and Mass Transfer*, 55(4):1246–1260, 2012. ISSN 0017-9310. doi: 10.1016/j.ijheatmasstransfer.2011.09.024. URL

<http://dx.doi.org/10.1016/j.ijheatmasstransfer.2011.09.024>.

- [17] Sylwia Szczukiewicz, Navid Borhani, and John Richard Thome. Two-phase flow operational maps for multi-microchannel evaporators. *International Journal of Heat and Fluid Flow*, 42:176–189, 2013. ISSN 0142-727X. doi: 10.1016/j.ijheatfluidflow.2013.03.006. URL <http://dx.doi.org/10.1016/j.ijheatfluidflow.2013.03.006>.
- [18] Claudi Martin-Callizo, Bjorn Palm, Wahib Owhaib, and Rashid Ali. Flow Boiling Visualization of R-134a in a Vertical Channel of Small Diameter. *Journal of Heat Transfer*, 132(3):031001, 2010. ISSN 00221481. doi: 10.1115/1.4000012. URL <http://heattransfer.asmedigitalcollection.asme.org/article.aspx?articleid=1449859>.
- [19] Peter A Kew and Keith Cornwell. Correlations for the prediction of heat transfer in small-diameter channels. *Applied Thermal Engineering*, 17:705–715, 1997.
- [20] Tannaz Harirchian and Suresh V. Garimella. A comprehensive flow regime map for microchannel flow boiling with quantitative transition criteria. *International Journal of Heat and Mass Transfer*, 53(13-14):2694–2702, June 2010. ISSN 00179310. doi: 10.1016/j.ijheatmasstransfer.2010.02.039. URL <http://linkinghub.elsevier.com/retrieve/pii/S0017931010001158>.

- [21] Tamanna Alam, Poh Seng Lee, and Christopher R. Yap. Effects of surface roughness on flow boiling in silicon microgap heat sinks. *International Journal of Heat and Mass Transfer*, 64:28–41, September 2013. ISSN 00179310. doi: 10.1016/j.ijheatmasstransfer.2013.04.009. URL <http://linkinghub.elsevier.com/retrieve/pii/S0017931013003141>.
- [22] Anze Sitar, Ivan Sedmak, and Iztok Golobic. Boiling of water and FC-72 in microchannels enhanced with novel features. *International Journal of Heat and Mass Transfer*, 55(23-24):6446–6457, November 2012. ISSN 00179310. doi: 10.1016/j.ijheatmasstransfer.2012.06.040. URL <http://linkinghub.elsevier.com/retrieve/pii/S0017931012004681>.
- [23] Chun Ting Lu and Chin Pan. Convective boiling in a parallel microchannel heat sink with a diverging cross section and artificial nucleation sites. *Experimental Thermal and Fluid Science*, 35(5):810–815, July 2011. ISSN 08941777. doi: 10.1016/j.expthermflusci.2010.08.018. URL <http://linkinghub.elsevier.com/retrieve/pii/S0894177710001792>.
- [24] Jae Yong Lee, Moo-Hwan Kim, Massoud Kaviany, and Sang Young Son. Bubble nucleation in microchannel flow boiling using single artificial cavity. *International Journal of Heat and Mass Transfer*, 54(25-26):5139–5148, December 2011. ISSN 00179310. doi: 10.

Bibliography

- 1016/j.ijheatmasstransfer.2011.08.042. URL <http://linkinghub.elsevier.com/retrieve/pii/S001793101100487X>.
- [25] Satish G. Kandlikar, Wai Keat Kuan, Daniel a. Willistein, and John Borrelli. Stabilization of Flow Boiling in Microchannels Using Pressure Drop Elements and Fabricated Nucleation Sites. *Journal of Heat Transfer*, 128(4):389, 2006. ISSN 00221481. doi: 10.1115/1.2165208. URL <http://link.aip.org/link/JHTRAO/v128/i4/p389/s1&Agg=doi>.
- [26] C.-J. Kuo and Y. Peles. Local measurement of flow boiling in structured surface microchannels. *International Journal of Heat and Mass Transfer*, 50(23-24):4513–4526, November 2007. ISSN 00179310. doi: 10.1016/j.ijheatmasstransfer.2007.03.047. URL <http://linkinghub.elsevier.com/retrieve/pii/S0017931007002979>.
- [27] A.K.M.M. Morshed, Fanghao Yang, M. Yakut Ali, Jamil a. Khan, and Chen Li. Enhanced flow boiling in a microchannel with integration of nanowires. *Applied Thermal Engineering*, 32:68–75, January 2012. ISSN 13594311. doi: 10.1016/j.applthermaleng.2011.08.031. URL <http://linkinghub.elsevier.com/retrieve/pii/S1359431111004613>.
- [28] Fanghao Yang, Xianming Dai, Yoav Peles, Ping Cheng, Jamil Khan, and Chen Li. Flow boiling phenomena in a single annular flow regime in microchannels (I): Characterization of flow boiling heat transfer. *International Journal of Heat and Mass Transfer*, 68:703–715, January

Bibliography

2014. ISSN 00179310. doi: 10.1016/j.ijheatmasstransfer.2013.09.058. URL <http://linkinghub.elsevier.com/retrieve/pii/S0017931013008326>.
- [29] Satish G. Kandlikar, Theodore Widger, Ankit Kalani, and Valentina Mejia. Enhanced Flow Boiling Over Open Microchannels With Uniform and Tapered Gap Manifolds. *Journal of Heat Transfer*, 135(6):061401, 2013. ISSN 0022-1481. doi: 10.1115/1.4023574. URL <http://heattransfer.asmedigitalcollection.asme.org/article.aspx?doi=10.1115/1.4023574>.
- [30] Matthew Law, Poh-Seng Lee, and Karthik Balasubramanian. Experimental investigation of flow boiling heat transfer in novel oblique-finned microchannels. *International Journal of Heat and Mass Transfer*, 76:419–431, September 2014. ISSN 00179310. doi: 10.1016/j.ijheatmasstransfer.2014.04.045. URL <http://linkinghub.elsevier.com/retrieve/pii/S0017931014003500>.
- [31] Alam Tamanna and Poh Seng Lee. Investigation of flow boiling characteristics in expanding silicon microgap heat sink. *Fourteenth Intersociety Conference on Thermal and Thermomechanical Phenomena in Electronic Systems (ITherm)*, pages 458–465, May 2014. doi: 10.1109/ITHERM.2014.6892317. URL <http://ieeexplore.ieee.org/lpdocs/epic03/wrapper.htm?arnumber=6892317>.

- [32] K. Balasubramanian, P. S. Lee, L. W. Jin, S. K. Chou, C. J. Teo, and S. Gao. Enhanced heat transfer and reduced pressure drop using stepped fin microchannels. *2011 IEEE 13th Electronics Packaging Technology Conference*, pages 653–659, December 2011. doi: 10.1109/EPTC.2011.6184500. URL <http://ieeexplore.ieee.org/lpdocs/epic03/wrapper.htm?arnumber=6184500>.
- [33] Jinliang Xu, Guohua Liu, Wei Zhang, Qian Li, and Bin Wang. Seed bubbles stabilize flow and heat transfer in parallel microchannels. *International Journal of Multiphase Flow*, 35(8):773–790, August 2009. ISSN 03019322. doi: 10.1016/j.ijmultiphaseflow.2009.03.008. URL <http://linkinghub.elsevier.com/retrieve/pii/S0301932209000597>.
- [34] Abhijit Mukherjee and Satish G. Kandlikar. Numerical simulation of growth of a vapor bubble during flow boiling of water in a microchannel. *Microfluidics and Nanofluidics*, 1(2):137–145, March 2005. ISSN 1613-4982. doi: 10.1007/s10404-004-0021-8. URL <http://www.springerlink.com/index/10.1007/s10404-004-0021-8>.
- [35] Rui Zhuan and Wen Wang. Simulation on nucleate boiling in micro-channel. *International Journal of Heat and Mass Transfer*, 53(1-3):502–512, January 2010. ISSN 00179310. doi: 10.1016/j.ijheatmasstransfer.2009.08.019. URL <http://linkinghub.elsevier.com/retrieve/pii/S0017931009004748>.

- [36] A. Mukherjee, S.G. Kandlikar, and Z.J. Edel. Numerical study of bubble growth and wall heat transfer during flow boiling in a microchannel. *International Journal of Heat and Mass Transfer*, 54(15-16):3702–3718, July 2011. ISSN 00179310. doi: 10.1016/j.ijheatmasstransfer.2011.01.030. URL <http://linkinghub.elsevier.com/retrieve/pii/S0017931011001426>.
- [37] Rui Zhuang and Wen Wang. Simulation of subcooled flow boiling in a micro-channel. *International Journal of Refrigeration*, 34(3):781–795, May 2011. ISSN 01407007. doi: 10.1016/j.ijrefrig.2010.12.004. URL <http://linkinghub.elsevier.com/retrieve/pii/S0140700710002781>.
- [38] M Magnini, B Pulvirenti, and J R Thome. Numerical investigation of the influence of leading and sequential bubbles on slug flow boiling within a microchannel. *International Journal of Thermal Sciences*, pages 1–17, 2013. ISSN 1290-0729. doi: 10.1016/j.ijthermalsci.2013.04.018. URL <http://dx.doi.org/10.1016/j.ijthermalsci.2013.04.018>.
- [39] M Magnini, B Pulvirenti, and J R Thome. Numerical investigation of hydrodynamics and heat transfer of elongated bubbles during flow boiling in a microchannel. *International Journal of Heat and Mass Transfer*, 59:451–471, 2013. ISSN 0017-9310. doi: 10.1016/

Bibliography

- j.ijheatmasstransfer.2012.12.010. URL <http://dx.doi.org/10.1016/j.ijheatmasstransfer.2012.12.010>.
- [40] S. S. Mehendale, a. M. Jacobi, and R. K. Shah. Fluid Flow and Heat Transfer at Micro- and Meso-Scales With Application to Heat Exchanger Design. *Applied Mechanics Reviews*, 53(7):175, 2000. ISSN 00036900. doi: 10.1115/1.3097347.
- [41] Satish G. Kandlikar. Fundamental issues related to flow boiling in minichannels and microchannels. *Experimental Thermal and Fluid Science*, 26(2-4):389–407, 2002. ISSN 08941777. doi: 10.1016/S0894-1777(02)00150-4.
- [42] C L Ong and J R Thome. Macro-to-microchannel transition in two-phase flow : Part 1 Two-phase flow patterns and film thickness measurements. *Experimental Thermal and Fluid Science*, 35(1):37–47, 2011. ISSN 0894-1777. doi: 10.1016/j.expthermflusci.2010.08.004. URL <http://dx.doi.org/10.1016/j.expthermflusci.2010.08.004>.
- [43] Jaeseon Lee and Issam Mudawar. Critical heat flux for subcooled flow boiling in micro-channel heat sinks. *International Journal of Heat and Mass Transfer*, 52(13-14):3341–3352, 2009. ISSN 00179310. doi: 10.1016/j.ijheatmasstransfer.2008.12.019. URL <http://dx.doi.org/10.1016/j.ijheatmasstransfer.2008.12.019>.

- [44] M. W. Wambsganss, D. M. France, J. a. Jendrzeczyk, and T. N. Tran. Boiling Heat Transfer in a Horizontal Small-Diameter Tube. *Journal of Heat Transfer*, 115(4):963, 1993. ISSN 00221481. doi: 10.1115/1.2911393.
- [45] W. Yu, D. M. France, M. W. Wambsganss, and J. R. Hull. Two-phase pressure drop, boiling heat transfer, and critical heat flux to water in a small-diameter horizontal tube. *International Journal of Multiphase Flow*, 28(6):927–941, 2002. ISSN 03019322. doi: 10.1016/S0301-9322(02)00019-8.
- [46] Bruno Agostini, John Richard Thome, Matteo Fabbri, Bruno Michel, Daniele Calmi, and Urs Kloter. High heat flux flow boiling in silicon microchannels Part I: Heat transfer characteristics of refrigerant R236fa. *International Journal of Heat and Mass Transfer*, 51(21-22):5400–5414, October 2008. ISSN 00179310. doi: 10.1016/j.ijheatmasstransfer.2008.03.006. URL <http://linkinghub.elsevier.com/retrieve/pii/S0017931008001592>.
- [47] Bruno Agostini, John Richard Thome, Matteo Fabbri, Bruno Michel, Daniele Calmi, and Urs Kloter. High heat flux flow boiling in silicon microchannels - Part II: Heat transfer characteristics of refrigerant R245fa. *International Journal of Heat and Mass Transfer*, 51(21-22):5415–5425, 2008. ISSN 00179310. doi: 10.1016/j.ijheatmasstransfer.2008.03.007.
- [48] Tailian Chen and Suresh V. Garimella. Local heat transfer distribution and effect of instabilities during flow boiling in a silicon microchannel heat

Bibliography

- sink. *International Journal of Heat and Mass Transfer*, 54(15-16):3179–3190, July 2011. ISSN 00179310. doi: 10.1016/j.ijheatmasstransfer.2011.04.012. URL <http://linkinghub.elsevier.com/retrieve/pii/S0017931011002286>.
- [49] Tannaz Harirchian and Suresh V. Garimella. Boiling Heat Transfer and Flow Regimes in Microchannels A Comprehensive Understanding. *Journal of Electronic Packaging*, 133(1):011001, 2011. ISSN 10437398. doi: 10.1115/1.4002721. URL <http://link.aip.org/link/JEPAE4/v133/i1/p011001/s1&Agg=doi>.
- [50] W Qu. Flow boiling heat transfer in two-phase micro-channel heat sinks I. Experimental investigation and assessment of correlation methods. *International Journal of Heat and Mass Transfer*, 46(15):2755–2771, July 2003. ISSN 00179310. doi: 10.1016/S0017-9310(03)00041-3. URL <http://linkinghub.elsevier.com/retrieve/pii/S0017931003000413>.
- [51] Weilin Qu and Issam Mudawar. Transport Phenomena in Two-Phase Micro-Channel Heat Sinks. *Journal of Electronic Packaging*, 126(2):213–224, 2004. ISSN 10437398. doi: 10.1115/1.1756145. URL <http://link.aip.org/link/JEPAE4/v126/i2/p213/s1&Agg=doi>.
- [52] Han J. Lee and Sang Yong Lee. Heat transfer correlation for boiling flows in small rectangular horizontal channels with low aspect ratios. *International Journal of Multiphase Flow*, 27(12):2043–2062, 2001. ISSN

03019322. doi: 10.1016/S0301-9322(01)00054-4.

[53] Satish G. Kandlikar and Prabhu Balasubramanian. An experimental study on the effect of gravitational orientation on flow boiling of water in 1054197 μm parallel minichannels. *Journal of Heat Transfer*, 127(8):820–829, 2005. doi: 10.1115/1.1928911.

[54] Avram Bar-Cohen and Emil Rahim. Modeling and Prediction of Two-Phase Microgap Channel Heat Transfer Characteristics. *Heat Transfer Engineering*, 30(8):601–625, 2009. ISSN 0145-7632. doi: 10.1080/01457630802656678.

[55] Yoshio Utaka, Shuhei Okuda, and Yutaka Tasaki. Configuration of the micro-layer and characteristics of heat transfer in a narrow gap mini/micro-channel boiling system. *International Journal of Heat and Mass Transfer*, 52(9-10):2205–2214, 2009. ISSN 00179310. doi: 10.1016/j.ijheatmasstransfer.2008.11.020. URL <http://dx.doi.org/10.1016/j.ijheatmasstransfer.2008.11.020>.

[56] Dae Whan Kim, Emil Rahim, Avram Bar-Cohen, and Bongtae Han. Direct submount cooling of high-power LEDs. *IEEE Transactions on Components and Packaging Technologies*, 33(4):698–712, 2010. ISSN 15213331. doi: 10.1109/TCAPT.2010.2040618.

[57] John R. Thome and Lorenzo Consolini. Mechanisms of Boiling in Micro-Channels: Critical Assessment. *Heat Transfer Engineering*, 31(4):288–297, April 2010. ISSN 0145-7632. doi: 10.1080/

Bibliography

01457630903312049. URL <http://www.tandfonline.com/doi/abs/10.1080/01457630903312049>.
- [58] Stefan S. Bertsch, Eckhard a. Groll, and Suresh V. Garimella. Review and Comparative Analysis of Studies on Saturated Flow Boiling in Small Channels. *Nanoscale and Microscale Thermophysical Engineering*, 12(3):187–227, September 2008. ISSN 1556-7265. doi: 10.1080/15567260802317357. URL <http://www.tandfonline.com/doi/abs/10.1080/15567260802317357>.
- [59] Jungho Kim. Review of nucleate pool boiling bubble heat transfer mechanisms. *International Journal of Multiphase Flow*, 35(12):1067–1076, December 2009. ISSN 03019322. doi: 10.1016/j.ijmultiphaseflow.2009.07.008. URL <http://linkinghub.elsevier.com/retrieve/pii/S0301932209001311>.
- [60] Satish G. Kandlikar. Scale effects on flow boiling heat transfer in microchannels: A fundamental perspective. *International Journal of Thermal Sciences*, 49(7):1073–1085, July 2010. ISSN 12900729. doi: 10.1016/j.ijthermalsci.2009.12.016. URL <http://linkinghub.elsevier.com/retrieve/pii/S1290072910000098>.
- [61] Anthony M. Jacobi and John R. Thome. Heat Transfer Model for Evaporation of Elongated Bubble Flows in Microchannels. *Journal of Heat Transfer*, 124(6):1131, 2002. ISSN 00221481. doi: 10.1115/

- 1.1517274. URL <http://link.aip.org/link/JHTRAO/v124/i6/p1131/s1&Agg=doi>.
- [62] V Dupont. Heat transfer model for evaporation in microchannels. Part II: comparison with the database. *International Journal of Heat and Mass Transfer*, 47(14-16):3387–3401, July 2004. ISSN 00179310. doi: 10.1016/j.ijheatmasstransfer.2004.01.007. URL <http://linkinghub.elsevier.com/retrieve/pii/S0017931004000328>.
- [63] Martin Freystein, Christoph Kirse, and Peter Stephan. Bubble coalescence and moving contact line evaporation during flow boiling in a single microchannel. In *ICNMM*, pages 1–6, 2014.
- [64] Sameer Raghavendra Rao, Farzad Houshmand, and Yoav Peles. Transient flow boiling heat-transfer measurements in microdomains. *International Journal of Heat and Mass Transfer*, 76:317–329, September 2014. ISSN 00179310. doi: 10.1016/j.ijheatmasstransfer.2014.03.029. URL <http://linkinghub.elsevier.com/retrieve/pii/S001793101400235X>.
- [65] Sajjad Bigham and Saeed Moghaddam. Microscale study of mechanisms of heat transfer during flow boiling in a microchannel. *International Journal of Heat and Mass Transfer*, 88:111–121, 2015. ISSN 0017-9310. doi: 10.1016/j.ijheatmasstransfer.2015.04.034. URL <http://dx.doi.org/10.1016/j.ijheatmasstransfer.2015.04.034>.

- [66] R Revellin and J R Thome. A new type of diabatic flow pattern map for boiling heat transfer in microchannels. *Journal of Micromechanics and Microengineering*, 17(4):788–796, April 2007. ISSN 0960-1317. doi: 10.1088/0960-1317/17/4/016. URL <http://stacks.iop.org/0960-1317/17/i=4/a=016?key=crossref.b63adf70f43d6f7d77cf7a6c154a6663>.
- [67] Yoon Jo Kim, Yogendra K Joshi, Andrei G Fedorov, Young-joon Lee, and Sung-kyu Lim. Thermal Characterization of Interlayer Microfluidic Cooling of Three-Dimensional Integrated Circuits With Nonuniform Heat. *Journal of Heat Transfer*, 132(April 2010):1–9, 2014. doi: 10.1115/1.4000885.
- [68] Jae-Mo Koo, Sungjun Im, Linan Jiang, and Kenneth E. Goodson. Integrated Microchannel Cooling for Three-Dimensional Electronic Circuit Architectures. *Journal of Heat Transfer*, 127(January 2005):49, 2005. ISSN 00221481. doi: 10.1115/1.1839582.
- [69] Rémi Revellin, Vincent Dupont, Thierry Ursenbacher, John R. Thome, and Iztok Zun. Characterization of diabatic two-phase flows in microchannels: Flow parameter results for R-134a in a 0.5 mm channel. *International Journal of Multiphase Flow*, 32:755–774, 2006. doi: 10.1016/j.ijmultiphaseflow.2006.02.016.

- [70] R Hohl, J Blum, M Buchholz, T Lüttich, H Auracher, and W Marquardt. Model-based experimental analysis of pool boiling heat transfer with controlled wall temperature transients. *International Journal of Heat and Mass Transfer*, 44(12):2225–2238, June 2001. ISSN 00179310. doi: 10.1016/S0017-9310(00)00272-6. URL <http://linkinghub.elsevier.com/retrieve/pii/S0017931000002726>.
- [71] James V. Beck, Ben Blackwell, and Charles R. St. Clair Jr. *Inverse Heat Conduction: Ill-Posed Problems*. Wiley Interscience Publication, 1985.
- [72] OM Alifanov. *Inverse heat transfer problems*. Springer-Verlag, Berlin, 1994. URL <http://adsabs.harvard.edu/abs/1988MIZMa.....A>.
- [73] Joachim Blum and Wolfgang Marquardt. An optimal solution to inverse heat conduction problems based on frequency domain interpretation and observers. *Numerical Heat Transfer, Part B: Fundamentals*, 32(4):453–478, December 1997. ISSN 1040-7790. doi: 10.1080/10407799708915019. URL <http://dx.doi.org/10.1080/10407799708915019>.
- [74] E. Bayo, H. Moulin, O. Crisalle, and G. Gimenez. Well-Conditioned Numerical Approach for the Solution of the Inverse Heat Conduction Problem. *Numerical Heat Transfer, Part B: Fundamentals*, 21(1):79–98, January 1992. ISSN 1040-7790. doi: 10.1080/

Bibliography

10407799208944923. URL <http://www.tandfonline.com/doi/abs/10.1080/10407799208944923>.
- [75] Miroslav Raudenský, Keith A. Woodbury, J. Kral, and T. Brezina. Genetic Algorithm in Solution of Inverse Heat Conduction Problems. *Numerical Heat Transfer, Part B: Fundamentals*, 28(3):293–306, October 1995. ISSN 1040-7790. doi: 10.1080/10407799508928835. URL <http://www.tandfonline.com/doi/abs/10.1080/10407799508928835>.
- [76] Jian Su and Geoffrey F. Hewitt. Inverse Heat Conduction Problem of Estimating Time-Varying Heat Transfer Coefficient. *Numerical Heat Transfer: Part A: Applications*, 45(8):777–789, May 2004. ISSN 1040-7782. doi: 10.1080/10407780490424299. URL <http://www.tandfonline.com/doi/abs/10.1080/10407780490424299>.
- [77] Wolfgang Marquardt and Hein Auracher. An observer-based solution of inverse heat conduction problems. *International Journal of Heat and Mass Transfer*, 33:1545–1562, 1990.
- [78] A.N. Tikhonov and V.Y. Arsenin. *Solution of Ill-Posed Problems*. V.H. Wniston, Washington DC, 1977.
- [79] J.V. Beck, B. Blackwell, and a. Haji-Sheikh. Comparison of some inverse heat conduction methods using experimental data. *International Journal of Heat and Mass Transfer*, 39(17):3649–3657, November 1996. ISSN 00179310. doi: 10.1016/0017-9310(96)00034-8.

Bibliography

- URL <http://linkinghub.elsevier.com/retrieve/pii/0017931096000348>.
- [80] J.R. Taylor. *An Introduction to Error Analysis*. University Science Books, 1997.
- [81] Peter a. Kew and Keith Cornwell. Correlations for the prediction of boiling heat transfer in small-diameter channels. *Applied Thermal Engineering*, 17(8-10):705–715, 1997. ISSN 13594311. doi: 10.1016/S1359-4311(96)00071-3.
- [82] Dae Whan Kim, Emil Rahim, Avram Bar-Cohen, and Bongtae Han. Thermofluid characteristics of two-phase flow in micro-gap channels. *2008 11th IEEE Intersociety Conference on Thermal and Thermomechanical Phenomena in Electronic Systems, I-THERM*, pages 979–992, 2008. ISSN 1087-9870. doi: 10.1109/ITHERM.2008.4544373.
- [83] Tailian Chen and Suresh V. Garimella. Measurements and high-speed visualizations of flow boiling of a dielectric fluid in a silicon microchannel heat sink. *International Journal of Multiphase Flow*, 32(8):957–971, August 2006. ISSN 03019322. doi: 10.1016/j.ijmultiphaseflow.2006.03.002. URL <http://linkinghub.elsevier.com/retrieve/pii/S0301932206000577>.
- [84] Sameer Raghavendra Rao and Yoav Peles. Spatiotemporally resolved heat transfer measurements for flow boiling in microchannels. *International Journal of Heat and Mass Transfer*, 89:482–493,

Bibliography

2015. ISSN 00179310. doi: 10.1016/j.ijheatmasstransfer.2015.05.062. URL <http://linkinghub.elsevier.com/retrieve/pii/S0017931015005566>.
- [85] Yaohua Zhang, Yoshio Utaka, and Yuki Kashiwabara. Formation Mechanism and Characteristics of a Liquid Microlayer in Microchannel Boiling System. *Journal of Heat Transfer*, 132(12):122403–1–7, 2010. ISSN 00221481. doi: 10.1115/1.4002365. URL <http://link.aip.org/link/JHTRAO/v132/i12/p122403/s1&Agg=doi>.
- [86] Satish G. Kandlikar, Wai Keat Kuan, and Abhijit Mukherjee. Experimental Study of Heat Transfer in an Evaporating Meniscus on a Moving Heated Surface. *Journal of Heat Transfer*, 127(March 2005):244–251, 2005. ISSN 00221481. doi: 10.1115/1.2397093.
- [87] T. C. Thulasidas, M. a. Abraham, and R. L. Cerro. Flow patterns in liquid slugs during bubble-train flow inside capillaries. *Chemical Engineering Science*, 52(17):2947–2962, 1997. ISSN 00092509. doi: 10.1016/S0009-2509(97)00114-0.
- [88] Satish G. Kandlikar. Heat Transfer Mechanisms During Flow Boiling in Microchannels. *Journal of Heat Transfer*, 126(1):8, 2004. ISSN 00221481. doi: 10.1115/1.1643090. URL <http://link.aip.org/link/JHTRAO/v126/i1/p8/s1&Agg=doi>.

Appendix A: Uncertainty Analysis

Uncertainties in results of experiments have been estimated based on principles explained by J.R. Taylor [80].

Uncertainty in Summation

Suppose $F = f(x, y, \dots, v, w)$ such that

$$F = x + y + \dots - v - w$$

and uncertainties in measuring x, y, \dots, v and w are $\delta x, \delta y, \dots, \delta v$ and δw respectively and if they are known to be independent and random, then the uncertainty in F is given as

$$\delta F = \sqrt{(\delta x)^2 + (\delta y)^2 + \dots + (\delta v)^2 + (\delta w)^2}$$

In any case, δF is never larger than their ordinary sum.

$$\delta F \leq \delta x + \delta y + \dots + \delta v + \delta w$$

Uncertainty in Products and Quotients

Suppose $F = f(x, y, \dots, v, w)$ such that

$$F = \frac{x \times y \dots}{\dots v \times w}$$

the fractional uncertainty in F is sum in quadrature of the fractional uncertainties in x, y, v and w and is given as

$$\frac{\delta F}{|F|} = \sqrt{\left(\frac{\delta x}{|x|}\right)^2 + \left(\frac{\delta y}{|y|}\right)^2 + \dots + \left(\frac{\delta v}{|v|}\right)^2 + \left(\frac{\delta w}{|w|}\right)^2}$$

if errors are known to be random and independent of each other. In any case, it is never large than their ordinary sum.

$$\frac{\delta F}{|F|} \leq \frac{\delta x}{|x|} + \frac{\delta y}{|y|} + \dots + \frac{\delta v}{|v|} + \frac{\delta w}{|w|}$$

List of Publications

International Conferences

1. M. Jagirdar, P.S. Lee, Transient evolution of heat transfer performance during flow boiling in a microchannel, in: Proc. ASME 2015 International Conference on Nanochannels, Microchannels, Minichannels InterPACK-ICNMM2015, 2015.
2. M. Jagirdar, P.S. Lee, Temperature transients for detection of flow-regimes in a mini/microchannel, in: 7th International Conference on Applied Energy ICAE2015, 2015.
3. M. Jagirdar, P.S. Lee, Methodology for More Accurate Assessment of Heat Loss in Microchannel Flow Boiling, in: 16th Electronics Packaging Technology Conference, EPTC2014 ,2014: pp. 630634.
4. Y. Fan, P.S. Lee, L. Jin, W. Chua, N. Mou, M. Jagirdar, A parametric numerical study in cylindrical oblique fin minichannel, in: Proc. ASME 2013 International Technical Conference and Exhibition on Packaging and Integration of Electronic and Photonic Microsystems, InterPACK2013, 2013.

International Journals

1. M. Jagirdar, P.S. Lee, A diagnostic tool for detection of flow-regimes in a microchannel using transient wall temperature signal. Status: Submitted to Applied Energy.
2. M. Jagirdar, P.S. Lee, Qualitative and quantitative performance of IHCP solution methodology for fast transients. Status: Submitted to Numerical Heat Transfer, Part A: Applications.
3. M. Jagirdar, P.S. Lee, Study of transient heat transfer during sub-cooled flow boiling in a low aspect ratio microchannel: Heat transfer mechanisms during slug flow. Status: To be submitted to International Journal of Multiphase Flow.
4. M. Jagirdar, P.S. Lee, Quasi-steady and transient study of heat transfer during sub-cooled flow boiling in a low aspect ratio microchannel. Status: To be submitted to International Journal of Heat and Mass Transfer.
5. K. Balasubramanian, M. Jagirdar, P.S. Lee, C.J. Teo, S.K. Chou, Experimental investigation of flow boiling heat transfer and instabilities in straight microchannels, International Journal of Heat and Mass Transfer 66 (2013) 655671.

Attachment

A CD has been attached with the thesis. It consists of a sample video file corresponding to figure [5.21](#).